Dynamics of Eutectic Growth in a Three-Phase System

By

Samira Mohagheghi

A Thesis Submitted to the
Graduate School of Engineering
in Partial Fulfillment of the Requirements for
the Degree of
Doctor of Philosophy
in
Materials Science and Engineering
Koc University

January 2018

Koc University

Graduate School of Sciences and Engineering

This is to certify that I have examined this copy of a Ph.D. thesis by

Samira Mohagheghi

and have found that it is complete and satisfactory in all respects,

and that any and all revisions required by the final

examining committee have been made.

Committee Members:

Melis Şerefoğlu Kaya, Ph.D.

_____

Mehmet Somer, Ph.D. (Co-Advisor)

_____

Sabine Bottin-Rousseau, Ph.D.

_____

Derya Dışpınar, Ph.D.

_____

Ehsan Layegh Khavidaki, Ph.D.

_____

Murat Sözer, Ph.D.

_____

Ersan Üstündağ, Ph.D.

_____

Date: 30 January 2018

To my beloved family

ABSTRACT

Solidification is involved in a variety of manufacturing processes such as casting, welding, soldering, and additive manufacturing. Solidification microstructures, which are the traces left in the solid by the propagating solid/liquid interface, evolve depending on the inherent characteristics of the materials as well as the process parameters. The properties of materials are significantly dependent on the microstructure and therefore, understanding the pattern formation phenomena is necessary to control and optimize the material properties. Because many industrially used materials are multi-phase, in recent years, an extensive research effort is dedicated to understanding how different microstructures form during solidification. However, this is a challenging task due to the fact that the multiplicity of phases and interphase boundaries lead to formation of highly complex microstructures. One of the examples of multi-phase materials is three-phase eutectic systems in which three crystalline phases are spontaneously growing from a homogenous liquid at the non-variant eutectic composition. Due to not having a mushy-zone and having well-ordered patterns, low melting temperatures, and excellent fluidity during casting, eutectic systems are used extensively in the industry. The research effort explained in this thesis aims to understand the fundamental and crucial, but currently unknown, aspects of three-phase eutectic growth by performing systematic experiments on In-Bi-Sn ternary system. The employed methodology is based on real-time investigation of solidification front dynamics from both sides of the quasi-2D samples using a novel optical microscopy system along with directional solidification techniques, namely directional solidification and rotating directional solidification setups.

In the first part of the thesis, the effect of sample thicknesses on the stability of the ABAC-type growth pattern, which is the basic state of the three-phase eutectic system in absence of interphase energy anisotropy, is investigated. It is found that by increasing sample thickness, the stability region of the ABAC pattern shrinks and this effect is correlated with

the mechanisms of the instabilities, namely lamellae elimination and branching. The dynamics and features of these instabilities are characterized thanks to the double-sided microscope by observing the phenomena simultaneously from top and bottom of the samples. Two key pattern recovery mechanisms are identified, namely phase invasion and phase exchange, which assist the system to spontaneously recover the isotropic ABAC pattern if the stacking faults are formed in the arrangement. In the second part, different three-phase eutectic grains are identified as a function of interphase anisotropy. Depending on the 2D-Wulff plots of the interphase boundaries, four distinct eutectic grain types are established in three-phase systems, namely isotropic, nearly-locked, fully-locked, and separated eutectic grains. While the isotropic eutectic grains have orientation-independent interphase boundary energies, non-singular and singular minima in certain angular ranges of the interphases' energies lead to formation of the nearly-locked and fully-locked eutectic grains, respectively. In these grains, the lamellar structures are inclined into the low-energy direction of the interphase boundary energies. In the last type of the three-phase eutectic grains called separated eutectic grain, not only the microstructure is deviated from regular ABAC pattern, but also the morphologies of the phases are totally altered due to the interphase anisotropy. Two distinguishable separated microstructures are identified and possible origins of each are proposed. Finally, other types of microstructures that are observed within this study are classified in terms of sample thickness dependent and anisotropy-driven microstructures.

ÖZET

Katılaşma, döküm, kaynak, lehim ve katmanlı imalat gibi çeşitli üretim metotlarında yer alır. Katılaşma mikroyapıları, ilerleyen katı/sıvı arayüzeyinin geride bıraktığı izlerdir. Bu yapılar, malzemenin içsel özellikleri ve proses parametrelerine bağlı olarak evrilir. Malzeme özellikleri önemli ölçüde mikroyapıya bağlıdır ve bu nedenle malzeme özelliklerinin kontrol ve optimize edilmesi için fazların dizilim oluşum prensiplerinin anlaşılması gerekir. Endüstride kullanılan malzemelerin çoğu çok fazlı olduğundan, son yıllarda, çok fazlı mikroyapının katılaşma esnasında nasıl oluştuğunu anlamaya yönelik birçok kapsamlı bilimsel araştırmalar yapılmıştır. Fakat fazların ve fazlar arası yüzeylerin çeşitliliğinden dolayı oldukça karmaşık mikroyapılar oluştuğundan, mikroyapının oluşum dinamikleri hayli karmaşık bir problemdir. Terner ötektik bir sistemde, ötektik kompozisyondaki homojen bir sıvıdan aynı anda üç kristal fazın büyüdüğü üç fazlı ötektik sistemler çok fazlı malzemelere bir örnektir. Ötektik sistemler, düzenli dizilime, düşük erime sıcaklığına, döküm sırasında mükemmel akışkanlığa sahip oldukları ve ayrıca katı ve sıvının beraber bulunduğu bir sıcaklık aralığı bulunmadığı için endüstride yaygın olarak kullanılırlar. Bu tezin amacı, In-Bi-Sn üçlü sistemi ile sistematik deneyler yaparak, üç fazlı ötektik büyümenin temel ve kritik ama henüz bilinmeyen özelliklerini anlamaktır. Katılaşma sırasında kısmı olarak 2B olan numunelerin katı/sıvı arayüzeyleri her iki taraftan gerçek zamanlı olarak incelenebilmesi için en gelişkin teknolojiler kullanılarak bu araştırmalar için üretilmiş tek yönlü katılaştırma ve dönen tek yönlü katılaştırma üniteleri kullanılmıştır.

Tezin ilk bölümünde, ara yüzey enerjisinin izotropik olduğu durumlarda numune kalınlığının, 2B ve üç fazlı ötektik sistemlerde temel yapı olan ABAC diziliminin kararlılığı üzerindeki etkileri araştırılmıştır. Numune kalınlığı arttıkça ABAC diziliminin kararlılık bölgesinin daraldığı ve bunun nedeninin kararsızlık mekanizmaları olan lamel eliminasyonu ve dallanması ile ilgili olduğu anlaşılmıştır. Bu kararsızlıkların dinamikleri ve özellikleri, mikroyapının alttan ve üstten aynı anda gözlemlenmesini sağlayan çift taraflı mikroskop sayesinde karakterize edilmiştir. Faz değişimi ve faz akını şeklinde adlandırdığımız ve dizilimde bir hata olduğunda ABAC yapısının tekrar elde edilmesini sağlayan iki kilit mekanizma olduğu belirlenmiştir.

İkinci bölümde, üç fazlı ötektik tanecikler, fazlar arası yüzey enerjisinin anizotropi fonksiyonundaki farklılıklara göre sınıflandırılmıştır. Ötektik tanecikler, fazlar arasındaki sınırların Wulff grafiklerine göre izotropik, kısmen kilitli, tamamen kilitli ve ayrıymış tanecikler olarak dört gruba ayrılmışlardır. İzotropik ötektik taneciklerde, fazlar arası yüzey enerjisi yönden bağımsızken, bu enerjinin belirli açı aralıklarında tekil ve tekil olmayan minimumlar olması, sırasıyla tamamen kilitli ve kısmen kilitli ötektik taneciklerinin oluşmasına sebep olmuştur. Bu taneciklerde lamel yapı, fazlar arası yüzey enerjisinin az olduğu yöne doğru eğilmiştir. Son grup olan ayrışmış taneciklerde ise mikroyapı düzenli ABAC dizilimini oluşturmadığı gibi fazların morfolojisi de fazlar arası anizotropiden dolayı tamamen değişmiştir. İki farklı ayrışmış mikroyapı tanımlanmış ve her birinin muhtemel kaynağı belirlenmiştir. Son olarak, bu çalışma kapsamında gözlemlenen diğer mikroyapı

tipleri numune kalınlığına bağlı ve anizotropi kaynaklı mikroyapılar olarak sınıflandırılmıştır.

ACKNOWLEDGEMENTS

I would like to express my deepest gratitude to my advisor Melis Şerefoğlu Kaya, for her encouragement, enthusiasm, and immense knowledge. Without her guidance and motivation, this thesis would not have materialized. I owe my gratitude to my co-advisor, Mehmet Somer whose knowledge and experience were all the time open to me.

My sincere appreciation to the members of my committee, Sabine Bottin-Rousseau, Derya Dışpınar, Murat Sözer, Ehsan Layegh Khavidaki, and Ersan Üstündağ for their contribution to my thesis. Discussions and valuable comments given by my group mates, Sinan Yücetürk and Mehmet Emre Çetinkaya have been a great help in this journey.

I have greatly benefited from KÜTEM (Koç University TÜPRAŞ Energy Center), KUYTAM (Koç University Surface Science and Technology), and I received generous support from Barış Yağçı.

I wish to thank the gorgeous country, Turkey, who welcomed me with open wings. Also, I would like to thank Koç University to provide me a scholarship and offer me good time of living on its beautiful campus.

I am most thankful to my family for all support and encouragement, especially my father, who has selflessly given me more than I ever could have asked for.

I also would like to acknowledge TÜBİTAK and European Commission Marie Curie Career Integration Grants for financially supporting this research study.

TABLE OF CONTENT

LIST OF TABLES

LIST OF FIGURES

NOMENCLATURE

A phase	In_2Bi phase
B phase	β-In phase
C phase	γ-Sn phase
ABAC	In_2Bi/β-In/In_2Bi/γ-Sn phase alternation
Ω	Center of rotation in rotating directional solidification experiments
CW	Clockwise rotation
CCW	Counterclockwise rotation
C_α	Composition of α phase
C_β	Composition of β phase
r*	Critical nucleus radius
N_F	Degree of freedom
D	Diffusion coefficient in liquid
DS	Directional solidification
EG	Eutectic grains
C_E	Eutectic composition
λ	Eutectic spacing
λ-plot	Eutectic spacing versus position of phases within the width of the sample plot
T_E	Eutectic temperature
Γ	Gibbs-Thomson coefficient
V	Growth velocity

K_r and K_c	Jackson and Hunt constants
L phase	Liquid phase
m	Liquidus slope
N_c	Number of chemical species
N_φ	Number of phases
λ_{JH}	The eutectic spacing corresponds to minimum undercooling
Λ_b	Reduced eutectic spacing corresponds to upper limit
Λ_c	Reduced eutectic spacing corresponds to lower limit
RDS	Rotating directional solidification
ω	Rotation speed
rms	Root mean square
STD	Standard deviation
δ	Sample thickness
S/L	Solid/liquid
S/S	Solid/solid
ε	Strenght of anisotropy in surface free energy
γ_{ij}	Surface energy vector between i and j phases
σ_{ij}	Surface tension vector of the ij interphase boundaries
G	Thermal gradient
3D	Three dimensional
2D	Two dimensional
ΔT	Undercooling
f	Volume fraction of phases

Chapter 1 : Introduction to eutectics

Introduction

1.1 Eutectic solidification principles

Solidification is involved in many manufacturing techniques such as casting [1, 2], soldering [3], welding [4-6], and additive manufacturing [7]. Comprehensive understanding of phenomena occurred during solidification requires intensive interdisciplinary knowledge in mathematics, physics, and materials science. Many materials properties are determined by the microstructural features; therefore, it is vital to realize how different parameters lead to the formation of various microstructures during solidification. In long run, this will result in controlling and optimizing the desired properties of the materials for particular applications.

Form thermodynamics point of view, solidification is a first-order phase transformation characterized by discontinuous change in the state variables. Two main terms involved in solidification are nucleation and growth. Based on the classical theory of nucleation, nuclei form in the liquid by statistical fluctuation. Competition between the surface energy associated with the formation of the surface of a nucleus and volume free energy associated with phase transformation yields a critical nucleus radius (r*). The nucleus size below r* is unstable and will melt. On the other hand, the nucleus size above r* is stable. Once the stable nuclei forms, the solid/liquid (S/L) interface will propagate. The growth of the solid is a non-equilibrium process. Latent heat produced by the growth will be transferred by conduction, convection and radiation [8, 9].

Eutectic solidification is characterized by the spontaneous growth of two or more solid phases form a homogenous liquid. Eutectic alloys have lower melting points compared to the melting temperature of the phases forming the eutectic system. These give rise to their superior flow properties and makes them excellent candidate materials for casting, welding, and soldering processes [10, 11]. The simple system in which two solids with different compositions form during eutectic reaction is a binary system. The eutectic phase transformation reads the following reaction:

$$L(C_E) \rightarrow \alpha\ (C_\alpha) + \beta\ (C_\beta)$$

The liquid at eutectic composition (C_E) and temperature (T_E), two solids, α and β with compositions of C_α and C_β are at equilibrium at constant pressure. Figure 1-1 shows schematic of a hypothetical binary phase diagram, in which the eutectic reaction occurs at T_E and C_E.

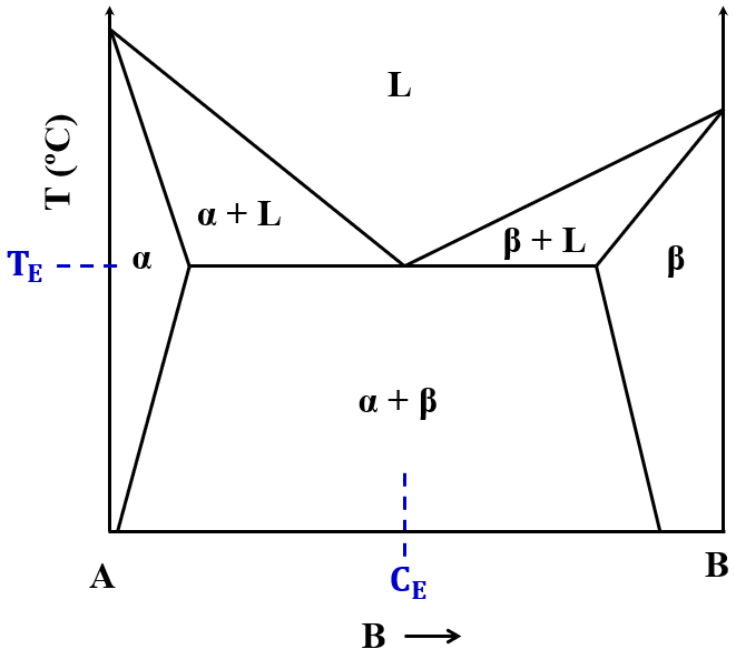

Figure 1-1. Schematic of a binary phase diagram with eutectic point.

According to Gibbs's phase rule, at the non-variant eutectic point, the degree of freedom (N_F) essentially is zero.

$$N_F = N_c - N_\varphi + 1 \qquad \text{(at constant pressure)}$$

Where N_c is the number of chemical species and N_φ is the number of phases at the equilibrium [12].

1.2 Coupled-growth concept in eutectic growth

The coupled-growth concept in eutectic growth was first developed by A. Kofler [8]. The concept states that there is a temperature-composition zone in which two eutectic phases in a binary alloy solidify in a coupled manner at the same velocity. The coupled-growth necessarily does not occur at either eutectic composition or temperature.

In eutectic growth, α or A-rich phase rejects the B atoms whereas β or B-rich phase rejects the A atoms into the liquid ahead of the front. The exchange of the solute occurs by the lateral diffusion of the rejected atoms in the liquid ahead of the solidification front. The lateral diffusion of A and B atoms towards α and β phases, respectively, illustrated in Figure 1-2, decreases the maximum and minimum composition variation ahead of the both solid phases. This mechanism of the growth is called “coupled growth” and it provides more efficient growth mechanism rather than the individual growth of each solid phase from the liquid.

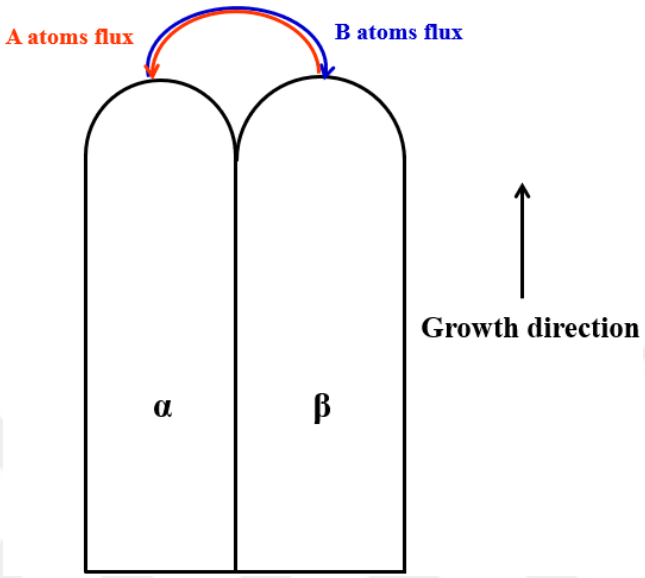

Figure 1-2. Schematic representation of the coupled growth during eutectic growth. While the A atoms diffuse laterally to reach α phase front, the B atoms diffuse in opposite direction to reach to β phase front.

1.3 Mechanical equilibrium in the triple point junction

At triple point junction, where the liquid meets the solid phases at local equilibrium conditions, the surface energies of the species are in equilibrium. Therefore, the surface energies of the solids with liquid, *i.e.* $\gamma_{\alpha L}$ and $\gamma_{\beta L}$, and the energy associated with the surface between α and β solids, *i.e.* $\gamma_{\alpha\beta}$, schematically shown in Figure 1-3, should follow the following equality.

$$\gamma_{\alpha\beta} = \gamma_{\alpha L}\cos\theta_1 + \gamma_{\beta L}\cos\theta_2$$

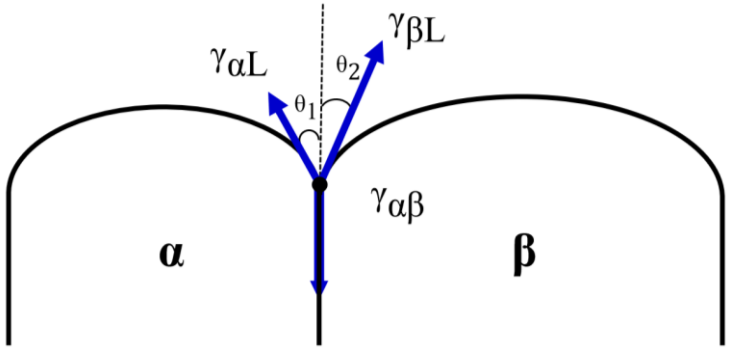

Figure 1-3. Mechanical equilibrium between surface energies in a triple-point junction. θ is the angle between surface energy of each indicated solid phases and the growth direction.

1.4 Phase morphology in eutectics

Solidification microstructures are greatly affected by the S/L energy, both in terms of magnitude and anisotropy function. Based on the properties of the S/L surface energy of the phases, eutectics are categorized into two major groups: regular or non-faceted/non-faceted and irregular or faceted/non-faceted eutectics.

When a solid phase has non-faceted interface with the liquid or in other words, it has *atomically-rough* interface, there will be many energetically favorable sites for the atoms attach. Therefore, the growing solid will appear in the form of smooth crystals at microscopic scale. Such solid is called non-faceted crystal, which is the characteristic of most of the metals. Many non-faceted/non-faceted eutectic system were investigated in the literature; metallic systems such as Sn-Pb [13-15], Al-Cu [16], Pb-Cd [17], Zn-Sn [18], In-In_2Bi [19]

and organic systems such as CBr_4-C_2Cl_6 and SCN-DC [20-24]. On the other hand, when a solid phase has faceted interface with the liquid or has *atomically flat* interface, attachment of the atoms to the interface is difficult. When such a barrier forms, the growth proceeds along particular crystallographic planes [25, 26]. This will lead to the formation of faceted crystals such as most of non-metals. Eutectics which have one faceted phases are called irregular eutectics and the most famous examples of the these eutectics are Al-Si [27, 28], Fe-C [29, 30], Cu-B [31, 32] systems and organic systems such as BOR-SCN [33], AMPD-SCN [34], and DC-NAP [35, 36]. Irregular eutectics have non-isothermal S/L interface and faceted phase grows simultaneously with the non-faceted matrix forming a wide range of spacings and orientations with respect to the overall growth direction [33].

In addition to the energetic features of the S/L interfaces, the volume fraction of the existing solid phases affects the eutectic microstructure. For isotropic systems, a usual rule of thumb is that if one of the phases has a small volume fraction, fibrous (rod) morphology of minority phase provides less interface area and therefore, the total interfacial energy is minimized. On the other hand, if the volume fractions of the phases are approximately the same, plate-like (lamellar) structure is preferred [1]. Figure 1-4 schematically illustrates the fibrous (rod) and plate-like (lamellae) morphologies in regular eutectics and their counterparts in irregular eutectics.

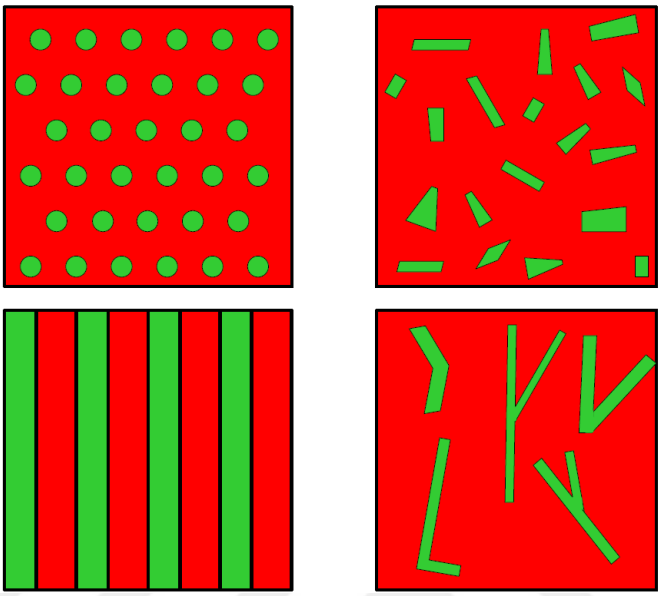

Figure 1-4. Phase morphology in regular and irregular eutectics. The first column represents the rod and lamellar structure in regular eutectic. The second column shows faceted structure in irregular eutectics.

While phase fraction is a preliminary factor to determine the phase morphology, it was proven that influence of sample geometry on development of solidification morphology is also determinant [20, 37]. The rod and lamellar eutectics are observed to coexist over a finite composition range and the transition from rod to lamellar morphology is not a sharp transition as it was previously believed [38].

1.5 Jackson and Hunt (JH) theory

The fundamental theory on steady-state growth of regular eutectics was proposed by Jackson and Hunt in 1966 [39]. Since then, the theory was the groundwork of the studies in the field of eutectic growth. The theory described that eutectics can form a uniform lamellar or rod patterns during directional solidification. Since this study deals with only lamellar structure, the focus will be on the former and the details of the theory will be discussed in this section. The theory considered the directional growth of the lamellar structure in a fixed thermal gradient in two-dimensional, where the effect of the convection in the liquid can be safely neglected.

The assumptions of JH theory are as follows:

1. The solidification front is planar and isothermal.
2. The diffusion occurs in the liquid and the diffusion in the solid is neglected.
3. Solid/solid interphase energy anisotropy is negligible and the α/β interphase boundary is essentially perpendicular to the solidification front. In other words, the two solid phases are growing in the direction of the imposed thermal gradient.
4. The triple-point junctions move only in the direction of the imposed thermal gradient.

Considering the symmetric phase diagram and linearized liquidus and solidus lines, they solved the diffusion equation for the moving S/L interface at a constant velocity (V) in the direction of the fixed thermal gradient (G). The outcome of the theory presents the

relation between undercooling necessary for the coupled growth of two phases (ΔT), the eutectic spacing (λ) and the growth velocity (V):

$$\Delta T = \frac{|m_\alpha||m_\beta|}{|m_\alpha| + |m_\beta|} V\lambda \frac{(C_s^\beta - C_s^\alpha)}{2\pi D} + \frac{2(1-f)|m_\beta|\Gamma_\alpha \sin(\theta_\alpha) + 2f|m_\alpha|\Gamma_\beta \sin(\theta_\beta)}{f(1-f)(|m_\alpha| + |m_\beta|)\lambda}$$

Where m stands for the slops of the liquidus lines, Γ is the Gibbs-Thomson coefficient, f is the volume fraction, D is the diffusion coefficient. θ is the angle of each surface energy vector of solid phases at the triple-point junction, as discussed in Figure 1-3. Considering all material constants as K_c and K_r (Jackson and Hunt constants), the undercooling equation can be simplified as follows:

$$\Delta T = K_c V\lambda + \frac{K_r}{\lambda}$$

Where K_c and K_r are:

$$K_c = \frac{(C_s^\beta - C_s^\alpha)|m_\alpha||m_\beta|}{2\pi D|m_\alpha| + |m_\beta|}$$

$$K_r = \frac{2(1-f)|m_\beta|\Gamma_\alpha \sin(\theta_\alpha) + 2f|m_\alpha|\Gamma_\beta \sin(\theta_\beta)}{f(1-f)(|m_\alpha| + |m_\beta|)}$$

The first term of the equation represents the undercooling necessary for diffusion and it decreases by decreasing the eutectic spacing value. This will provide short path for the lateral diffusion of the atoms. On the other hand, the second term is the capillary undercooling associated with the curvature of the S/L interface, hence decreases with increase in eutectic spacing values. The capillary undercooling can decrease the total undercooling by reducing the S/L interface curvature. Nature finds the optimum in eutectic spacing value between these opposing features. The undercooling versus the eutectic spacing plot for a hypothetical alloy is shown in Figure 1-5.

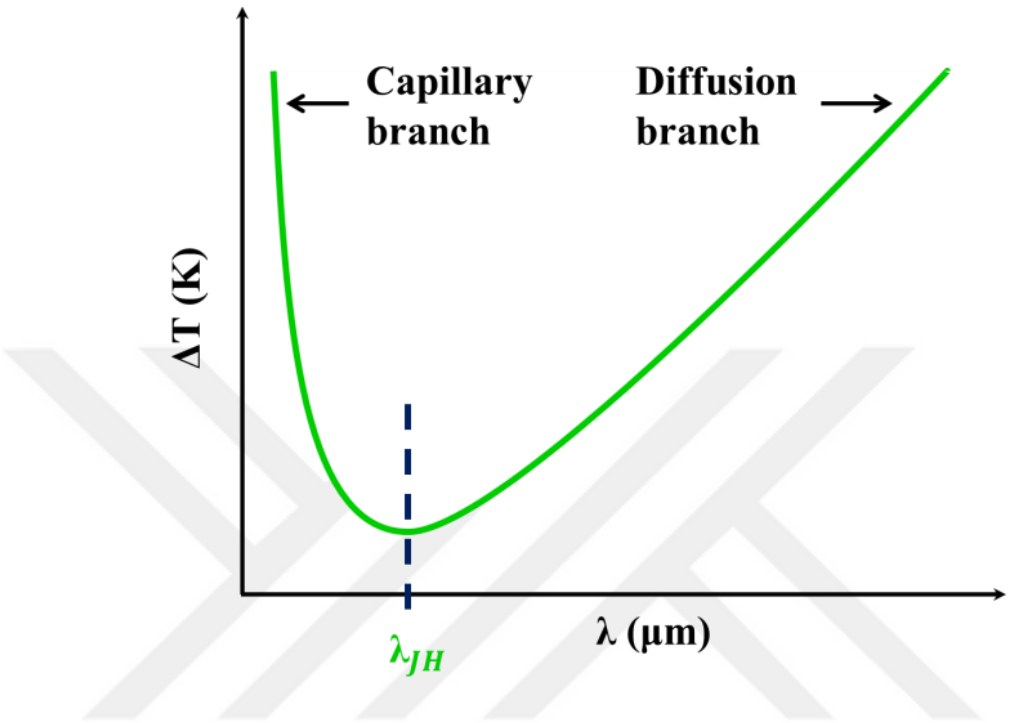

Figure 1-5. Undercooling at the S/L interface as a function of the eutectic spacing plot for a hypothetical eutectic system.

Jackson and Hunt proposed that the eutectic growth occurs at the minimum undercooling. The eutectic spacing corresponding to the minimum undercooling value is designated by λ_{JH} on Figure 1-5. One can take the derivative of the equation and find the minimum value of the eutectic spacing, known as Jackson and Hunt spacing (λ_{JH}):

$$K_c\, V - \frac{K_r}{\lambda_{JH}^2} = 0$$

$$\lambda_{JH}^2 V = K_r / K_c$$

This relationship is called JH law and it described that $\lambda_{JH}^2 V$ parameter is a constant and depends on the system properties.

1.6 Instabilities at the limits of stability region

JH theory proposed that the periodic lamellar structure cannot grow below the minimum undercooling spacing. Beyond the stability regime, system undergoes catastrophic changes, namely, lamellae elimination and branching. The formation of these instabilities in fact is a process of the adaptation of the eutectic spacing to the new situation [12, 40, 41]. Consider a regular lamellar structure which is growing at a constant velocity (V_2), shown in Figure 1-6. If the velocity is increased from V_2 to V_3, the lamellar spacing is corresponding to the minimum undercooling larger than the new λ_{JH}. In this case, λ_{JH} of V_2 is located in the diffusion side of the plot of λ_{JH} of V_3 and to adopt to the new condition, lamellae branching occurs. On the other hand, if the velocity is decreased from V_2 to V_1, the system is located in the capillary branch of the plot. Consequently, the new eutectic spacing now is larger than the spacing at V_2. In order to adjust to the new condition, the system terminates one phase.

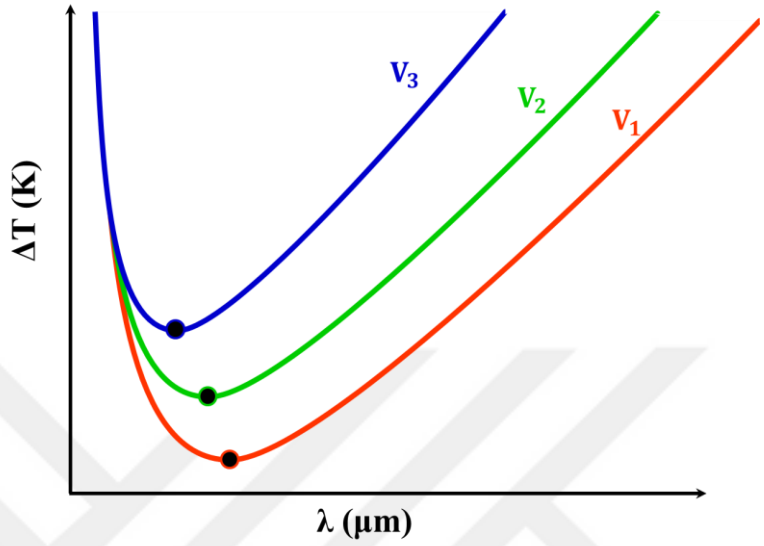

Figure 1-6. Schematic undercooling as a function of the eutectic spacing graph at three different velocities. $V_3>V_2>V_1$.

Figure 1-7 shows the branching and elimination events observed in a transparent organic system, namely CBr_4-C_2Cl_6, adopted from the movie of Jackson and Hunt [12].

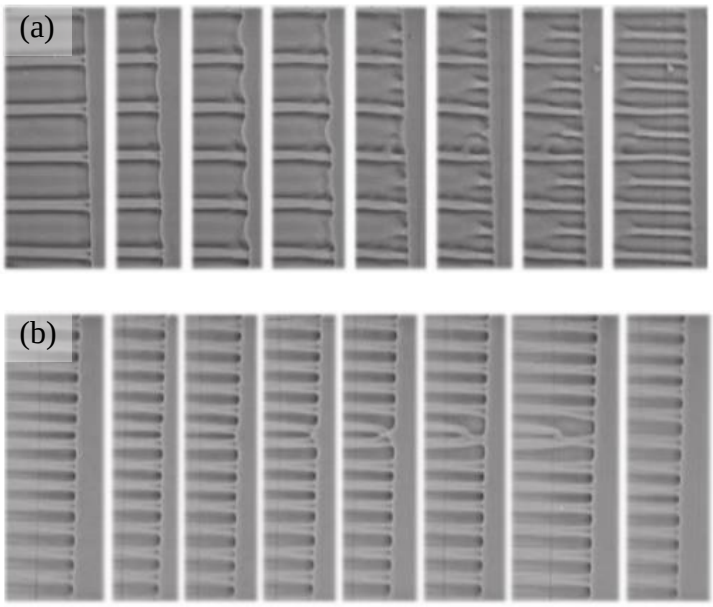

Figure 1-7. The instabilities occurred beyond the stability limits in a periodic lamellar structure of a binary system. (a) Branching event resulted from an increase in growth velocity. (b) Elimination event occurred as a result of a decrease in growth velocity [12].

One of the main directions in understanding pattern selection in eutectic solidification is to recognize and characterize the instabilities, which bound the stability region of the pattern. In 2D samples, while in lower limit, the only identified instability is the elimination, upper limit is accompanied with various instabilities [42]:

- Oscillations: 1λ-oscillatorry mode is characterized by the oscillation of the thicknesses of the two phases. In this type of instability, the mirror planes are in the middle of each phase. On the other hand, in 2λ-oscillatorry, one of the phases oscillates and the

mirror planes in the other phase only stays intact. In a study by M. Zimmermann *et al.* on Al-Cu eutectic system, it was shown that breakdown of steady-state lamellar in the hypoeutectic compositions was not necessarily associated with formation of dendrites of the primary phase. Destabilization of the front was accompanied by formation of oscillations in wide range of composition and growth rates. Consistency between these results and similar findings in organic systems lead to the conclusion that such microstructures are the features of the eutectic solidification, irrespective of the system [43].

- Tilted structure: In tilted state, the eutectic spacing can be reduced by a factor of $\sin(\theta)$, where θ is tilted angle. In this type of structure, both mirror symmetry planes disappear.

The results of the experimental work by M. Ginibre *et al.* [44], S. Akamatsu *et al.* [45, 46] along with Karma *et al.* [24] are summarized in Figure 1-8, where the undercooling is given as a function of the reduced eutectic spacing, $\Lambda = \lambda/\lambda_{JH.}$. Plot shows the basic-state region and the stability region bounded by different instabilities.

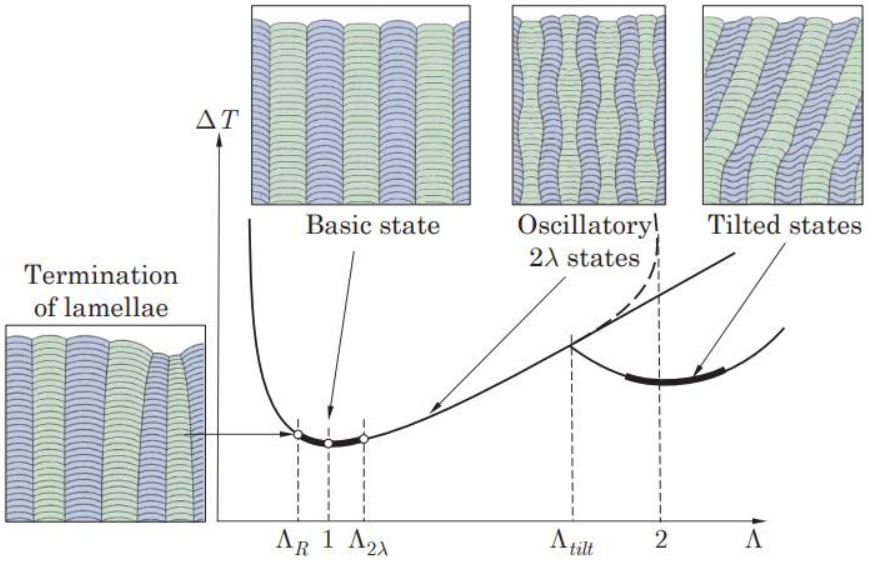

Figure 1-8. The stability diagram for regular two-phase eutectic systems. The undercooling as a function of reduced eutectic spacing plot shows different sections with various states of the system [12].

The features of Figure 1-8 can be summarized as follows:

- The basic-state is at $\Lambda = 1$ corresponds to the steady-state microstructure (minimum undercooling criteria).
- Λ_R shows the threshold of termination (elimination) instability at the lower limit of the stability regime of basic state.
- $\Lambda_{2\lambda}$ corresponds to 2λ oscillation instability.
- Λ_{tilt} represents tilt bifurcation. Periodic tilted lamellar structure appears at $\Lambda > \Lambda_{tilt}$.

The example microstructures of the discussed instabilities are shown in Figure 1-9.

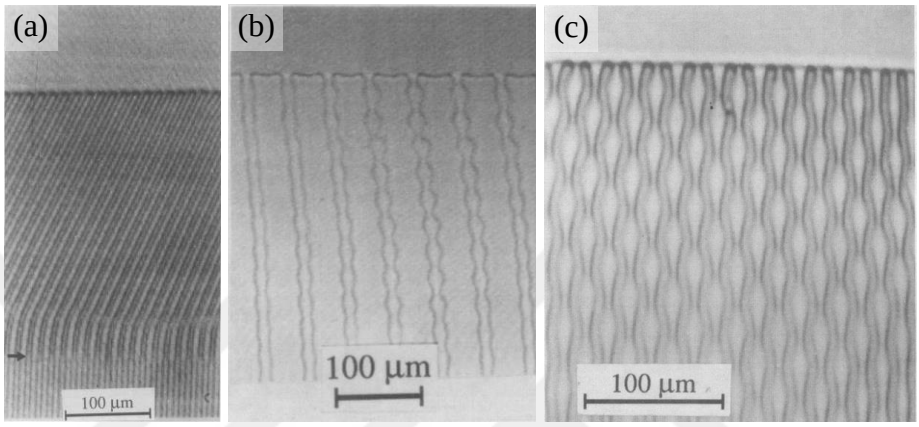

Figure 1-9. Various instabilities observed. (a) Tilted structure. (b) 1λ-oscillation. (c) 2λ-oscillation [24].

Later studies on eutectic systems showed that the eutectic spacing disperses even in the most careful experiments. This contrasts with the generally believed fact that lamellar eutectics should obey the "selection principle". This means that in sufficiently long experiments at a fixed V and G, the growth front should eventually reach to a unique and selected pattern. According to JH theory, the selected spacing should be the one that corresponds to the minimum undercooling. However, it is experimentally and numerically proved that no selection in eutectic spacing occurs and interplay between different instabilities of the system keeps the eutectic spacing between a stable range of spacings [47].

According to JH theory, the spacing below the minimum undercooling spacing is not stable and the system undergoes elimination process. Later S. Akamatsu *et al.* showed that eutectics can grow below the minimum undercooling spacing due to phase diffusion phenomenon, which is the homogenization process of the eutectic spacing distribution over time. The experimental results on the thin samples of CBr_4-C_2Cl_6 and two-dimensional phase-field simulation disclosed that the triple-point junctions move laterally with respect to the growth direction as well, in contrast to the assumption of the JH theory. The lateral movement of the triple-point junctions overstablizes the pattern and reduces the formation of strong gradient in the eutectic spacing [48, 49]. This consequently leads to stable pattern below λ_{JH} [46]. Later study on the same system showed the stability of the lamellar structure even in the reduced eutectic spacing values around $0.65\lambda_{JH}$. Not only in transparent organic alloys, but also in metallic systems the stability of the pattern below λ_{JH} was shown. S. Akamatsu *et al.* performed in-situ experiments with In–In_2Bi two-phase eutectic alloy and determined that the periodic lamellar structure is stable between $\Lambda_c = 0.8$ and $\Lambda_b = 2.2$, where Λ_c and Λ_b are respectively the reduced eutectic spacing corresponding to the lower and upper bounds of the stability regime [19].

1.7 Solidification Modeling

The solidification microstructures are numerically studied with phase-field modeling. This modeling technique offers a systematic tool to predict microstructure evolution by taking into account both diffusional field and evolution of the interface [12, 50]. The main advantage of this method is the replacement of the sharp interfaces by diffuse interfaces with a finite thickness. An order parameter is introduced, which generally takes the value of 1 for solid phase and -1 for liquid phase. This order parameter is homogenously and continuously changing in S/L interface [51, 52]. Many solidification microstructures ranging from dendrites [53], lamellar and rod eutectics [54, 55], bulk sample and multiphase systems [56, 57], and even complicated phenomena such as spiraling eutectic dendrites [58, 59] were successfully simulated by phase-field modeling. Undoubtedly, the phase-field modeling technique is a powerful tool and together with experimental observations will increase the understanding of fundamental aspects of solidification microstructures.

1.8 Pattern formation phenomena in physics

Pattern formation is common phenomena in nature. No matter in which system it occurs, the organized patterns arise spontaneously from the interactions between many determinant factors involved in the system. Pattern formation can be in chemical reagents that react and diffuse or wind-blown sand grains. These patterns are called self-organized.

Understanding how these self-organized patterns are formed is therefore addressed in various scientific fields, ranging from zoology and chemical kinetics to sociology and economic systems.

Even though thermodynamics determines the final, stable state of a reacting system, it is silent about the pattern formation phenomena. Despite the fact that a universal theory of pattern formation in nature does not exist, the study of the pattern formation will provide many aspects of the common principles, such as the universality of basic lamellar, hexagonal, branched, and spiral patterns [60].

The pattern formation during solidification is categorized under non-equilibrium pattern forming systems and it got the attention of physicists in the recent decades. This mostly arises from the mutual interest in phase transitions phenomena between physicists and materials scientists. The complexity of the pattern-selection phenomena comes from the underlying instabilities of the systems in which these phenomena occur. This is due to the fact that pattern-forming behavior is highly sensitive to slight variation in system parameters [61]. The fruitful interaction between the concepts and methods of nonlinear physics and materials science techniques cast further light on understanding the fundamental aspects of pattern formation phenomena in solidification.

Chapter 2 : Three-phase eutectic growth in quasi-2D samples during directional solidification

2.1 Introduction

Numerous experimental, theoretical, and numerical studies have been performed on solidification of single phase and two-phase systems. However, a wide range of practically used materials are multi-phase. Therefore, a great attention of research studies is shifted towards multiphase solidification in recent years. The main questions are that the how the microstructure form during solidification of multi-phase systems and how different physical parameters interact to form a particular pattern. Once the pattern formation dynamics are understood, in long run, it will lead to design materials with desired and optimized properties. Achieving such comprehensive understanding, however, needs interdisciplinary effort between physics, mathematics, and materials science. Pattern formation phenomena during solidification of multi-component alloys are less understood compared to single and two-phase systems. The difficulties arise from the different morphological stabilities and the complex nature of dynamical behavior of the patterns in multiphase systems [62].

In this study, the focus will be on a three-phase eutectic system with a composition of the non-variant point of a ternary alloy. In a ternary alloy, near to the non-variant eutectic composition, the liquid turns to three solid phases, without any primary phase formation. Such three-phase structure has a planar solidification front, similar to formation of a pure element [63]. In ternary eutectic systems, different microstructural configurations naturally exist due to the presence of three phases, *i.e.* A, B, and C. This adds complexity to the microstructure selection as well as the analysis of growth dynamics of three-phase systems.

While in two-phase systems, AB stacking sequence is the only possible configuration, in three-phase systems, various stacking sequence can exist such as ABC, ABAC, ABABAC, etc.

The microstructure formation during solidification of three-phase systems became the subject of numerical as well as experimental studies. Choudhury *et al.* [57] numerically studied the stability of different phase arrangements in three-phase eutectic systems using phase-field method. They assumed a symmetric phase diagram for the system, and measured the average undercooling for different phase arrangements. They focused on two major arrangements, ABC and ABAC. While the ABC phase arrangement shows no mirror plane, the ABAC stacking sequence contains two mirror planes in the middle of B and C phases, which are designated by blue and green colors in Figure 2-1. Their results showed good agreement with theoretical values of the minimum undercooling and corresponding eutectic spacing.

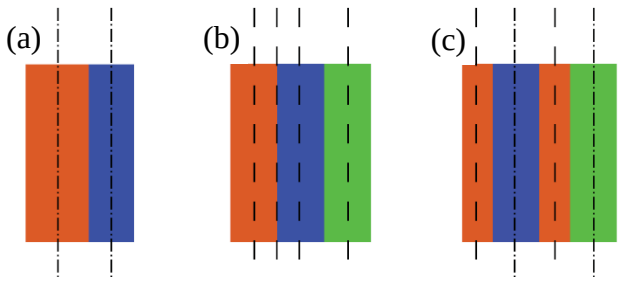

Figure 2-1. Different phase arrangements possible in three-phase systems compared with two-phase systems. (a) AB stacking sequence of a two-phase system. There exit two mirror

planes in the middle of each phase shown by dashed-dotted lines. (b) ABC stacking sequence in three-phase systems. The configuration does not have a real mirror plane. Only quasi-mirror lines exist for this configuration shown by dashed lines. (c) ABAC stacking sequence in three-phase systems. This configuration has two mirror planes shown by dashed-dotted lines in the middle of B and C phases which are colored blue and green [57].

They compared the calculated undercooling values of these two types of configuration in three-phase systems at two different growth velocities. For both configurations, they have found good agreement between theoretical prediction and simulation results.

Experimentally, no steady-state ABC pattern is observed; most likely due to symmetry-broken arrangement of ABC phase alternation. In experimental studies, on the other hand, ABAC stacking was observed in different systems, from metals to organic materials [64]. In Pb-Sn-Cd system, W. J. Boettinger [65] and J.D. Holder [66] showed the formation of the ABAC arrangement in ternary eutectic alloys. L. Sturz *et al.* [21] and V.T. Witusiewicz *et al.* [67] showed the formation of the ABAC stacking sequence in the three-phase AMPD–DC–NPG–SCN quaternary organic alloys along ternary path. The earlier study on In-Bi-Sn system in thick samples by M. A. Ruggiero and J.W. Rutter [68], revealed the lamellar microstructure formation with the ABAC sequence at higher growth rate. Later, V.T. Witusiewicz *et al.* [69] performed in-situ directional solidification experiment on In-Bi-Sn ternary alloy using thin samples. They showed that the lamellar microstructure takes the symmetric ABAC stacking sequence instead of simple ABC arrangement. The steadiness of

ABAC pattern originates from the presence of mirror symmetry axes in the middle of B and C phases, which ease the solute redistribution in the solidification front during coupled growth. In a recent experimental study by S. Bottin-Rousseau *et al.* [70], stability of ABAC pattern was examined using In-Bi-Sn three-phase eutectic system wherein sample thickness was equal to 13 μm. Similar to two-phase systems, in three-phase eutectics, the lower and upper limits of the stability coincided with lamellae elimination and branching, respectively. It is reported that ABAC pattern could be obtained after elimination and afterwards eutectic spacing profile was homogenized by phase-diffusion process [46, 49]. After branching, however, the symmetry was broken by formation of ABABAC-type stacking faults and thus phase-diffusion phenomenon could not be verified after branching for three-phase eutectics. The details of these spacing adjustment mechanisms in three-phase systems are more complicated than the two-phase counterparts since, at the simplest case, a series of elimination or branching event should take place to preserve the ABAC pattern.

In this chapter, the following unknown aspects of three-phase eutectic systems are addressed: (***i***) The formation of ABAC pattern in quasi-2D samples will be investigated. (***ii***) The possible variations in the stability thresholds by increasing the sample thickness will be explored. (***iii***) Thanks to the novel microscopy system called double-sided microscope, dynamics and mechanisms of the instabilities formed at the threshold of stability region were characterized and will be explained in detail. (***iv***) The recovery mechanisms of the ABAC

pattern after these instabilities were identified and their detailed features are presented in this chapter.

2.2 Experimental procedure

The In-Bi-Sn eutectic system is selected due to its two major advantages. First, it has a non-variant eutectic point in which three solid phases grow with non-faceted S/L interfaces. Secondly, the low eutectic temperature of the alloy allows monitoring of the solidification front in real time. This alloy is one of the potential candidates for lead-free solders [3, 71] and therefore, the understanding of the solidification characteristics of these types of alloys will open a new way to their use in the electronics industry.

The non-variant eutectic point in this system is at 59.2°C at In–20.7Bi–19.1Sn (at.%) composition [69]. The ternary phase diagram of the In-Bi-Sn system is illustrated in Figure 2-2. During eutectic reaction three solid phases form: In_2Bi, β-In, and γ-Sn, all of which have non-faceted S/L interfaces. The composition of each phase is given in Table 2-1.

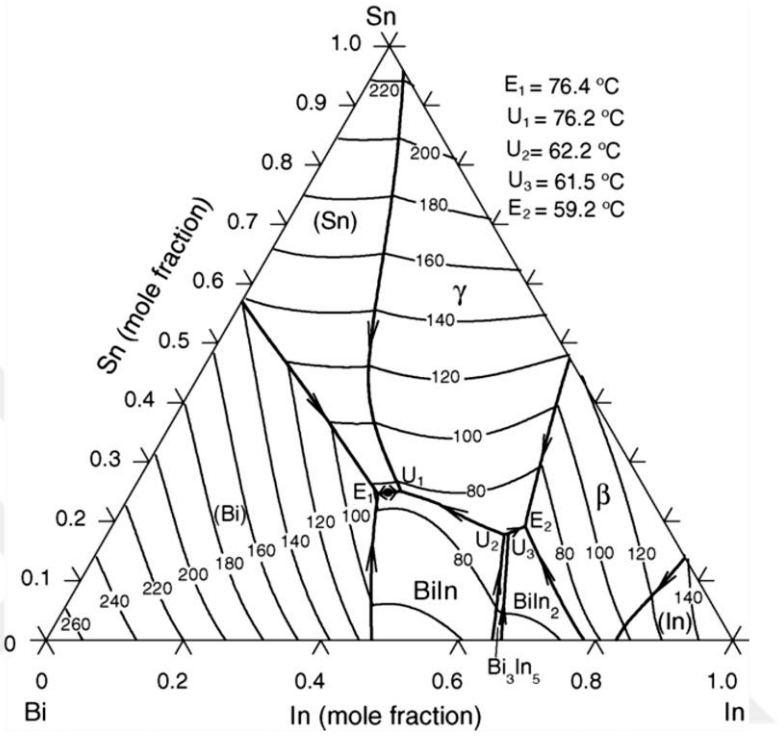

Figure 2-2. In-Bi-Sn ternary phase diagram. E_2 is the non-variant eutectic composition used in this study [69].

Table 2-1. Chemical compositions of three eutectic phases of In-Bi-Sn system [69].

Phase	**In (at.%)**	**Bi (at.%)**	**Sn (at.%)**
A: In_2Bi	66.48 ± 0.14	30.52 ± 0.23	3.00 ± 0.24
B: β-In	64.14 ± 0.42	11.38 ± 0.33	24.48 ± 0.27
C: γ-Sn	40.14 ± 0.21	16.11 ± 0.21	43.75 ± 0.35

In-Bi-Sn alloy close to the ternary eutectic point was prepared from 99.999% pure elements (Alfa Aesar). The elemental Bismuth, Indium, and Tin were precisely weighed and

then the mixture was melted and stirred under Argon atmosphere for sufficient amount of time to achieve a homogenous composition.

The sample container consists of two glass plates separated with a Mylar spacer. The glasses were washed employing multi-step cleaning operations. The thicknesses of the glasses are approximately 0.3 mm. The main region of the sample is rectangular with 4 mm width, 40 mm length in DS experiments. Figure 2-3 illustrates the schematic of the sample and the actual one.

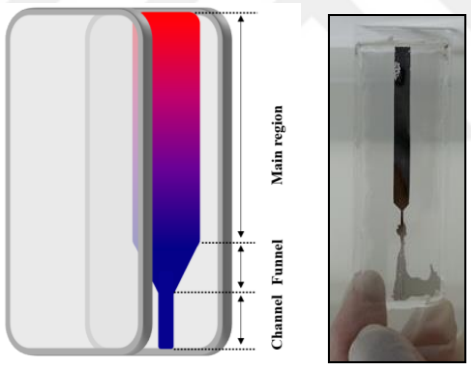

Figure 2-3. Schematic of the sample container and the actual sample.

Three different Mylar thicknesses, which are 23, 50, and 100 μm were used. The samples were filled with the molten alloy by Argon pressure using a setup illustrated in Figure 2-4 and sealed right away to avoid contamination.

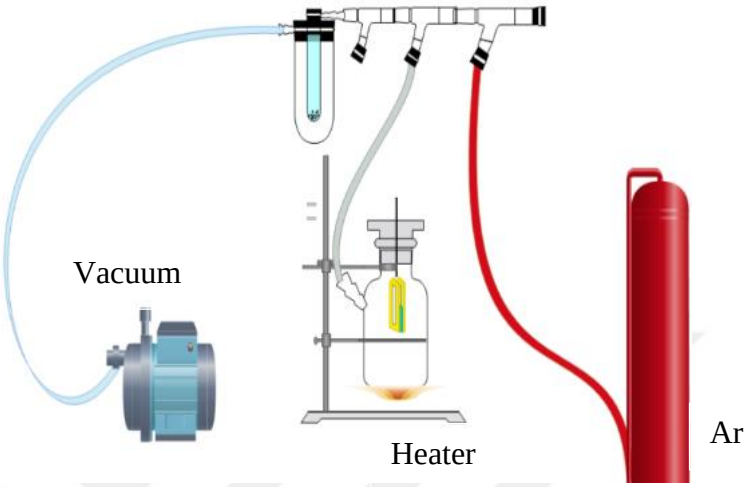

Figure 2-4. Schematic of the sample filling setup. The setup consists of a vacuum pump, an Argon tank, a heater/stirrer, and the connection line.

2.2.1 Directional solidification setup and the experiment protocol

The Bridgman solidification technique was introduced by Bridgman in 1923. The sample container is pulled down in a furnace between hot and cold zones [72]. Generally speaking, in Bridgman facility one zone is heated above the melting temperature of the material and the other zone is cooled down to temperature sufficiently below the melting temperature of the material. Therefore, a thermal gradient is established between zones [73].

A home-made horizontal Bridgman-type setup was used in the directional solidification (DS) studies. The samples were directionally solidified at a fixed thermal gradient of 3.3 K/mm. Horizontal Bridgman setup consists of a hot and a cold zone made out of copper

blocks, and a motor to push the sample from hot to cold side in order to solidify it. While hot zone is heated by resistance heaters, water is circulated through the copper blocks of the cold zone. In order to avoid thermal fluctuations, which would destroy local equilibrium conditions, the sample is sandwiched between cold and hot blocks as shown in Figure 2-5. This maximizes the contact surface of the blocks with the sample and minimizes the airflow. The temperatures of hot and cold blocks are adjusted to place the solidification front in between the zones. The investigated growth velocity range is 0.02 – 0.5 μm/s. During steady-state growth, the position of the S/L interface is stationary with respect to the laboratory frame. In other words, sample pushing velocity is equal to the growth velocity.

The blocks are fixed on an isolative plate with a gap in between them and situated on top of the double-sided microscope stage, which enables real-time observation of solidification front from both top and bottom of the sample. Double-sided microscope consists of an inverted and an upright microscope, lenses of which can be aligned such that both microscopes are focused on the same region of interest with a micrometer resolution, from both top and bottom of the sample. Throughout this study, top and bottom microstructures are referred to the images taken by these two microscopes. The microscopes are equipped with CMOS cameras, which are connected to computers for automated real-time acquisition of solidification front images.

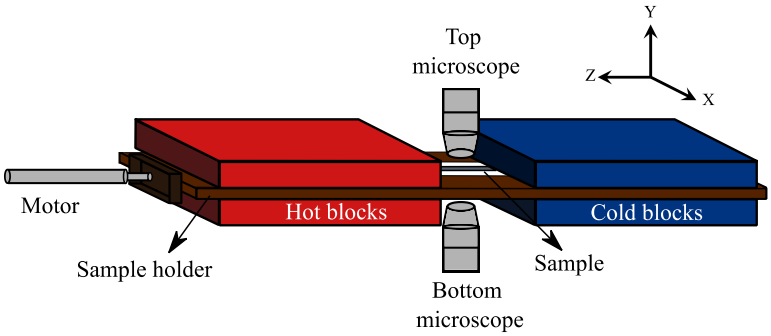

Figure 2-5. Schematic representation of the DS Bridgman setup. Z is the direction of imposed thermal gradient, X and Y are the directions of sample width and thickness, respectively.

After contrast enhancement, each phase of the eutectic microstructure has a different color due to their particular refractive index. For simplicity, the phases are designated A, B, and C such that black (A), white (B), and gray (C) phases are In_2Bi, β-In, and γ-Sn phases, respectively. We use the typical eutectic spacing (λ) definition for three-phase eutectics in 2D, *i.e.* the width of one ABAC unit, as well as the Cartesian coordinates where Z, X, and Y are the axes representing the direction of imposed thermal gradient (G), sample width, and sample thickness (δ), respectively. Schematic representation of ABAC pattern is shown in Figure 2-6.

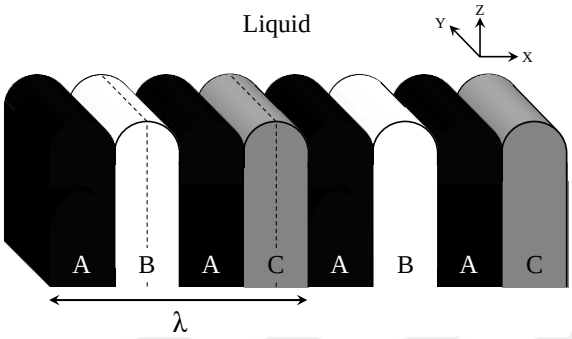

Figure 2-6. Schematic representation of the ABAC pattern during DS experiment. Mirror-symmetry planes at the center of B and C phases are shown with the dashed lines. λ is the eutectic spacing. Temperature is increasing in Z direction. Sample width and thickness are in X and Y directions, respectively.

In order to acquire the most accurate λ data, it is measured from four different interphase boundaries of one ABAC unit ($A_1B_1A_1C_1$) to the next one ($A_2B_2A_2C_2$). In other words, λ is measured from A_1B_1, B_1A_1, A_1C_1, C_1A_2 boundaries to A_2B_2, B_2A_2, A_2C_2, C_2A_3 boundaries, respectively. The locations of these boundaries are determined using an image processing software. Hence, for each ABAC pattern, a total of 4 λ measurements are made as shown in the spatial distribution plots of eutectic spacing along X direction, namely the λ-plots, given in *Results and Discussion* sections. All the measurements performed in this study are taken from large isotropic ABAC grains. In isotropic ABAC grains, the surface energy of the interphase boundaries, *i.e.* AB and AC, of the system are parallel to the imposed gradient direction. In other words, the tipple point junctions follow the gradient direction.

The width of the area from which λ is measured is dependent on the size of these isotropic ABAC grains. In our quasi-2D samples, along the width of the sample, generally there exist multiple grains.

2.2.2 ABAC pattern growing protocol

Formation of an extended isotropic eutectic grain with ABAC arrangement requires great care. The procedure is started by melting of the sample down to a place in a channel position. The channel is the narrower part of the sample, ~ 700 µm-thick, which assists formation of less eutectic grains in the main region of the sample. In this step, the solidification front is kept at zero velocity for sufficient time in order to form of a polycrystalline layer of a phase [45], shown in Figure 2-7 (a). In all experiments, this phase is γ-Sn. This means that the actual composition is deviated from the eutectic composition and there is small excess of γ-Sn. By the start of the directional movement, the second phase which is In_2Bi grows from the layer underneath and reaches to the front through existing channels between γ-Sn crystals, illustrated in Figure 2-7 (b). In_2Bi phase rapidly invades through the front. Subsequently, two phases grow (γ-Sn and In_2Bi), Figure 2-7 (c), for a certain growth length. The length of two-phase growth depends on the experimental conditions. Generally, a slow velocity gives rise to longer two-phase growth length. The next step is the initiation of the third phase, β-In, as shown in Figure 2-7 (d). The initiation of the

third phase is a 3D mechanism accompanied by the emission of the β-In branches [44] between growing γ-Sn/In_2Bi alternation. Eventually, the three phases grow together, and the pattern gradually reaches to the periodic ABAC pattern by elimination of the faults in stacking sequence and the eutectic spacing is homogenized by phase-diffusion process. In fact, this procedure was sometimes repeated several times to achieve the desired grain.

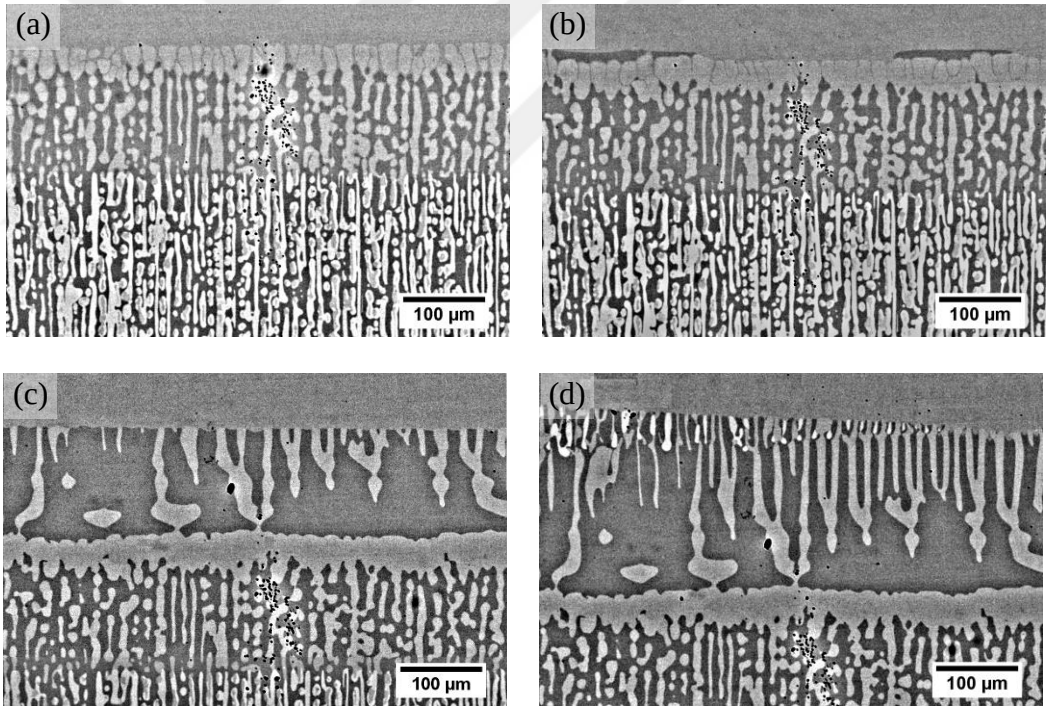

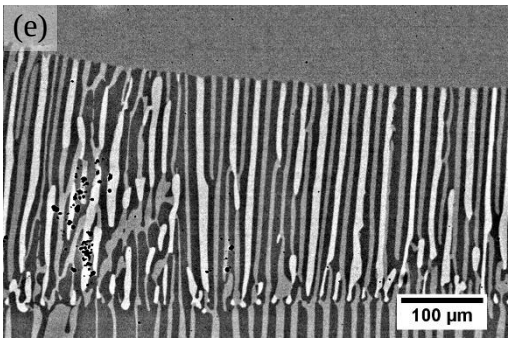

Figure 2-7. The initial stages of the ABAC pattern formation. (a) The front is occupied with polycrystalline γ-Sn (C) at V = 0 µm/s. (b) Lateral invasion of In_2Bi (A) phase. In_2Bi sweeps the front as soon as the directional movement started at V = 0.100 µm/s. (c) Two-phase growth of In_2Bi and γ-Sn at V = 0.100 µm/s. (d) Initiation of the growth of β-In (B) phase at the same velocity. (e) Initial stages of three-phase growth. The nonplanarity of the S/L interface on left-side of the image is due irregularity in the shape of Mylar spacer. G = 3.3 K/mm and δ = 50 µm.

2.3 Results and discussion

An example ABAC pattern observed from top and bottom of the sample is given in Figure 2-8. In an isotropic ABAC pattern, each phase is a lamella, and this can be confirmed by having the identical microstructure in top and bottom views of the sample.

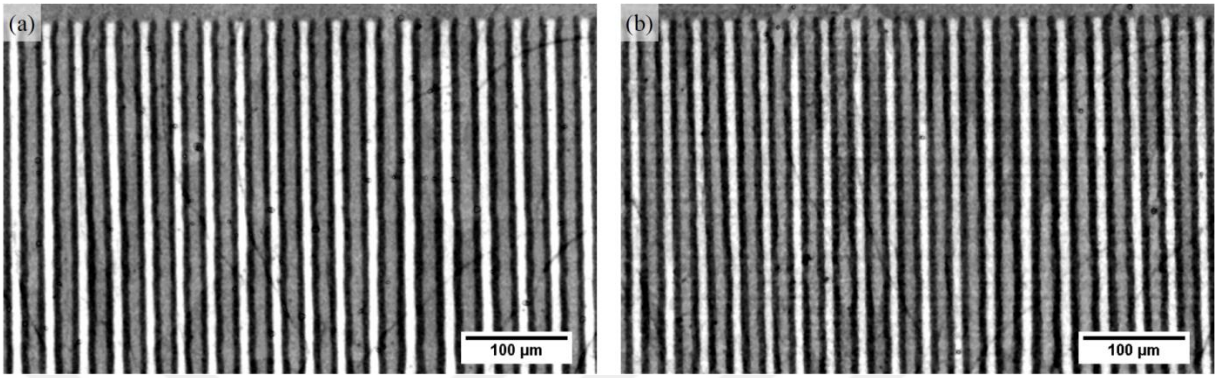

Figure 2-8. ABAC-type growth pattern in In-Bi-Sn system formed during a DS experiment. (a) Top microstructure. (b) Bottom microstructure. Identical microstructures existed in top and bottom views of the sample. V = 0.150 µm/s, G = 3.3 K/mm, and δ = 23 µm.

2.3.1 Lower and upper limits

In quasi-2D samples, similar to 13 µm-thick samples [70], the lower and upper stability limits of the ABAC pattern correspond to lamellae elimination and branching, respectively. In ABAC arrangement, if only one phase branches or eliminates as in the case of two-phase eutectic structures, the symmetry of the ABAC pattern will be locally broken. In order to preserve the ABAC stacking, a series of branching or elimination should take place at the right locations. Detailed explanation of the dynamics of these two spacing adjustment mechanisms as well as the recovery dynamics of the ABAC pattern are given in the following subsections.

The samples used in this study are called quasi-2D due to having both 2D and 3D features. 2D features include lamellae extending from top side of the sample to the bottom side, without an interruption, which is confirmed by the images showing exactly the same microstructure on top and bottom of the sample, during steady-state growth, as shown in Figure 2-8. Whereas, the spacing adjustment and recovery mechanisms have 3D features proven by the difference in phase sequence at the top and bottom of the sample. Figure 2-9 shows examples of elimination and branching in three-phase system. In Figure 2-9 (a), as a result of velocity increase from 0.045 to 0.050 μm/s, branchings of only one type of phase are occurred and this breaks the symmetry of the ABAC pattern. In Figure 2-9 (b), by decreasing velocity from 0.180 to 0.140 μm/s, eliminations of A, B, and C phases in series take place, which results in preservation of ABAC pattern.

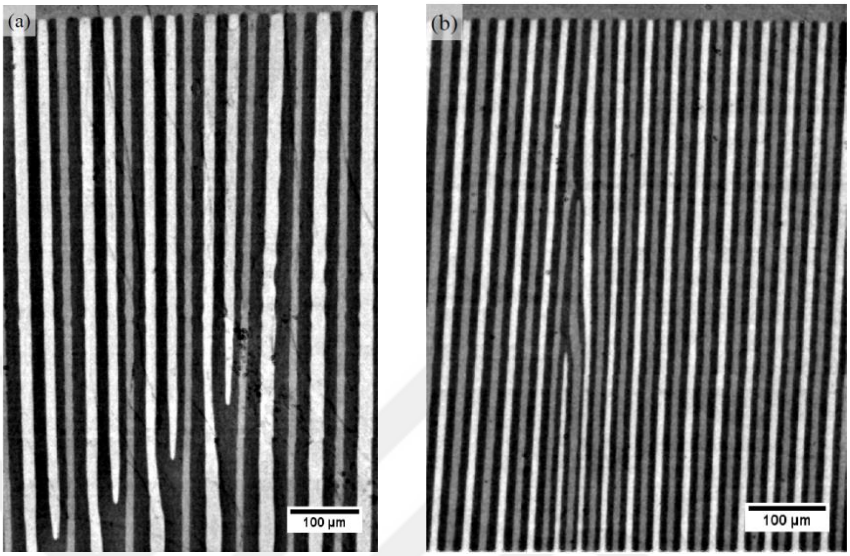

Figure 2-9. Spacing adjustment mechanisms observed in ABAC pattern. (a) Series of branching events took place as result of an upward velocity jump. (b) Elimination event occurred due to a downward velocity jump. δ = 23 µm and G = 3.3 K/mm.

2.3.2 Lower limit: lamellae elimination

Elimination happens when the spacing is less than the minimum threshold value of the stability range (λ_{el}), which is generally observed after a downward velocity jump, *i.e.* when the initial velocity (V_i) is higher than the final velocity (V_f). Lower limit of eutectic spacing corresponds to a global minimum at the λ-plot. Beyond this limit, ABAC eutectic pattern is no longer stable and it tries to go back to the stable regime using spacing adjustment mechanisms.

Figure 2-10 (a) shows the microstructure where two ABAC pattern elimination events took place, shown by white and black dashed circles corresponding to first and second eliminations, respectively. The λ-plot was measured from the location shown by the dotted line, where the recovery of the ABAC pattern occurred after the first elimination and before the onset of the second one. It can be seen from the λ-plot that spacing distribution has a local maximum at the position of 426 μm due to the first elimination event and a global minimum at the position of 205 μm right before the onset of the second elimination event. Local minima or maxima in λ-plots are homogenized with time by the phase diffusion mechanism.

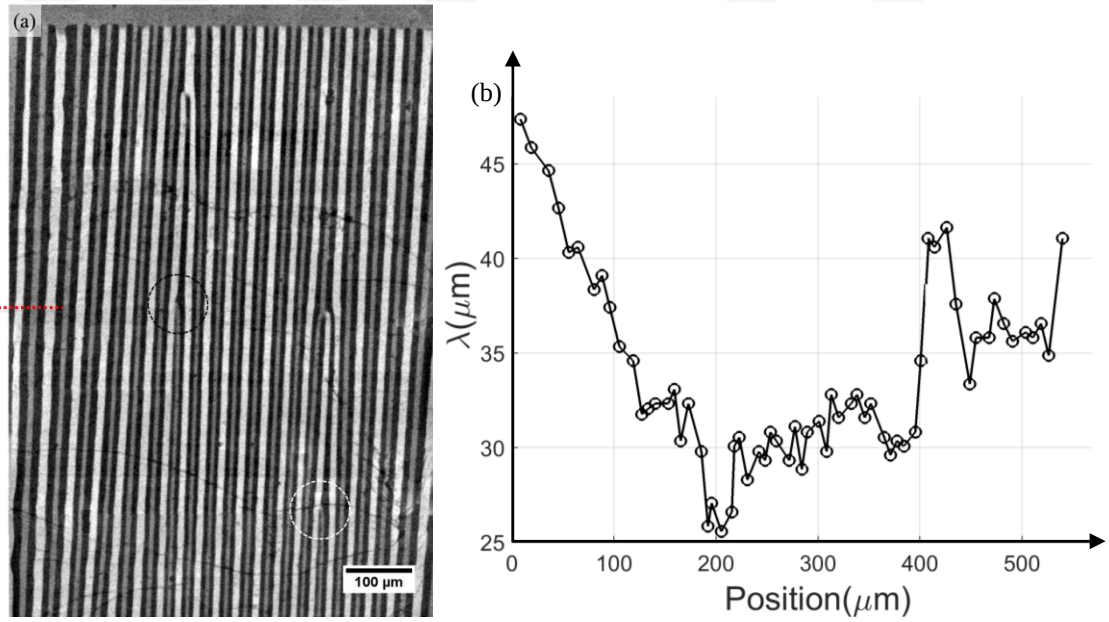

Figure 2-10. Elimination instability and corresponding eutectic spacing plot. (a) Elimination of two ABAC patterns shown by dashed circles after a velocity change from V_i = 0.180 μm/s

to V_f = 0.140 µm/s. (b) λ-plot corresponding to the dotted line in (a) shows a global minimum right before the onset of the second elimination and a local maximum after the first elimination events. δ = 23 µm and G = 3.3 K/mm. λ_{el} = 25.56 µm.

3D features of the elimination process are summarized in Figure 2-11, where top and bottom views of the microstructure are given along with the λ-plots corresponding to the onset of the elimination. While instability started at the bottom at time t_1 by elimination of a black and gray phases, ABAC pattern is still preserved on top. Only after 750 seconds, *i.e.* at t_2, elimination starts with white phase on top. This time difference corresponds to 60 µm growth length at V = 0.080 µm/s between t_1 and t_2. The corresponding λ-plots for top and bottom at t_1 show that the λ values are not significantly different at the region of elimination, *i.e.* around the minimum value of λ at the position of 330 µm. This shows that the start of elimination on one side with a different time and phase than the other side is mainly due to of dynamical reasons. Slight relaxation in the spacing distribution of the top microstructure was observed around the minimum value between t_1 and t_2, probably due to onset of elimination at the bottom at t_1. As a result, during the elimination process, the lamellar configuration around the spacing-adjusting region is not the same at both sides of the sample. Additionally, on top view, after elimination of a phase, neighboring phases merge resulting in decrease of phases from two to one, while at the bottom, each phase of ABAC is eliminated one at a time. Although the time, sequence, and mechanism of elimination are different at the sides of the sample, at the end, ABAC pattern is recovered at both sides of the sample

after elimination. There is a local maximum in λ-plot at the position of 189 µm originated from an elimination of a fault in ABAC pattern and due to slowness of the phase diffusion process, the spacing distribution is non-homogenous around this position. It is worth to note here that in all of the experiments performed in this study, the final outcome of an elimination process is the termination of one ABAC motif, without a single exception. It other words, ABAC pattern is always recovered after elimination.

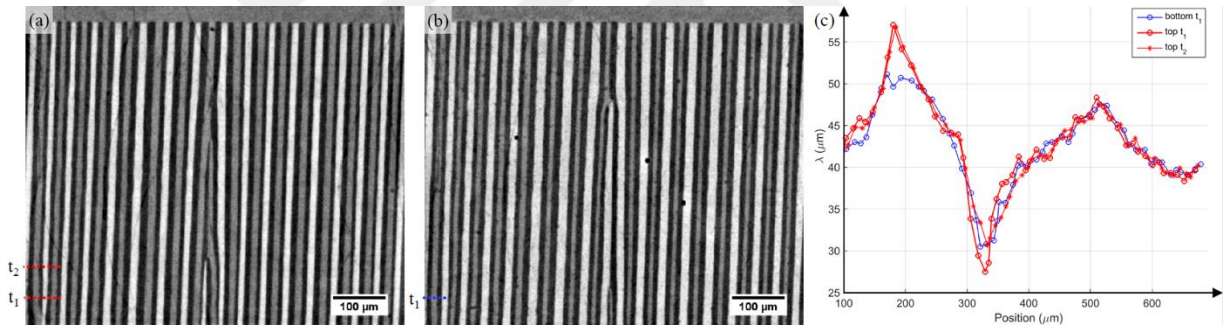

Figure 2-11. Elimination instability occurred when the velocity was decreasedfrom V_i = 0.100 µm/s to V_f = 0.080 µm/s. Microstructure is viewed from two sides of the sample (a) Top microstructure. (b) Bottom microstructure at the same time with (a). (c) λ-plots corresponding to times t_1 and t_2, which are marked on the microstructures. The spacing distribution of the bottom view at t_2 is not given since ABAC motif is not preserved at that time. λ^{Bottom}_{el} = 30.49 µm and λ^{Top}_{el} = 30.69 µm. δ = 23 µm and G = 3.3 K/mm.

After elimination, recovery of ABAC pattern can take place with more complex mechanisms such as phase exchange [70], which is the replacement of a phase with another. Details of phase-exchange mechanism are explained here by using the top and bottom views of the solidification front as shown in Figure 2-12. It is worth to note here that lamellae can be tilted with respect to Y direction which may result in a slight shift in X direction between top and bottom microstructures. Additionally, the difference in thicknesses of each phase in top and bottom views in Figure 2-12 shows that the geometry of lamellar is actually a trapezoidal prism instead of rectangular prism morphology. Schematic representation of the phase-exchange mechanism through the thickness of the sample, assuming all the phase boundaries are straight and perpendicular to glass walls, is given step-by-step in Figure 2-13, wherein to follow the process easily, each phase in the region is specified as follows:

a) Numbers at the subscripts designates the number of ABAC unit to which the phase belongs. In total two ABAC units ($\sum_1^2$ ABAC) were involved in the phase-exchange mechanism,
b) "f" and "s" subscripts specify the first and second A phase, respectively, within one ABAC motif,
c) "T" and "B" superscripts are used for top and bottom views, respectively.

When the eutectic spacing reaches elimination threshold, $A^T_{1f}, B^T_1, A^T_{2f,} B^T_2$ phases are eliminated on top within $\sum_1^2$ ABAC, while A^B_{1s}, C^B_1, A^B_{2s}, C^B_2 phases are eliminated in the bottom of the sample. That gives rise to a sequence of $A^T_{1s}C^T_1A^T_{2s}C^T_2$ on top and

$A^{B}_{1f}B^{B}_{1}A^{B}_{2f}B^{B}_{2}$ at the bottom of the sample right at the growth front. This shows another 3D feature of the elimination event on the grounds that the lamellae are only eliminated halfway through the thickness (Y direction). After these eliminations, probably, while A^{T}_{1s} is merged with A^{B}_{1f}, A^{T}_{2s} merged with A^{B}_{2f}. Thus, the new arrangement of the phases not only breaks the symmetry of the pattern in XZ plane but also in YZ plane. Since repetition of two-phase array in a three-phase system is not favored due to diffusional reasons at the solidification front, this arrangement is expected to exist only as a transient state. After 285 seconds (62.7 μm growth length), C^{T}_{1} invades from top to bottom (Y direction) and eliminates B^{B}_{2} from the bottom view. From the top view, though, it is observed that B^{B}_{2} is actually not eliminated all the way, but invades from the bottom and reaches to the opposite side and eliminates C^{T}_{1} from the top view. This phenomenon, *i.e.* the exchange of two phases through the thickness of the sample, is called phase exchange, and it enables recovery of the ABAC pattern. In this scenario, phase A plays a role as the enabling media for phase exchange by providing the path for B and C phase invasions, most probably, by having a negative curvature in Y direction at the growth front. As a result of this phase-exchange mechanism, ABAC pattern is recovered at both top and bottom of the sample (Figure 2-12 (c, d) and Figure 2-13 (c)).

The velocity of through-thickness invasion, that is the movement of a phase from one side of the sample to the other one, can be measured by dividing the sample thickness with the time difference between disappearances of invading phase from one side to appearance of it on the other side of the sample. For the phase-exchange example shown in Figure 2-12,

the invasion velocity measured with this method is ≈ 0.19 μm/s, which is close to the growth velocity, 0.220 μm/s. The uncertainty in determination of the invasion velocity comes from the facts that the image acquisition frequency was 0.2 Hz, a phase is only visible by the optical system when it reaches several microns in size, and it is assumed that a phase is invading from one wall to the other wall of the sample.

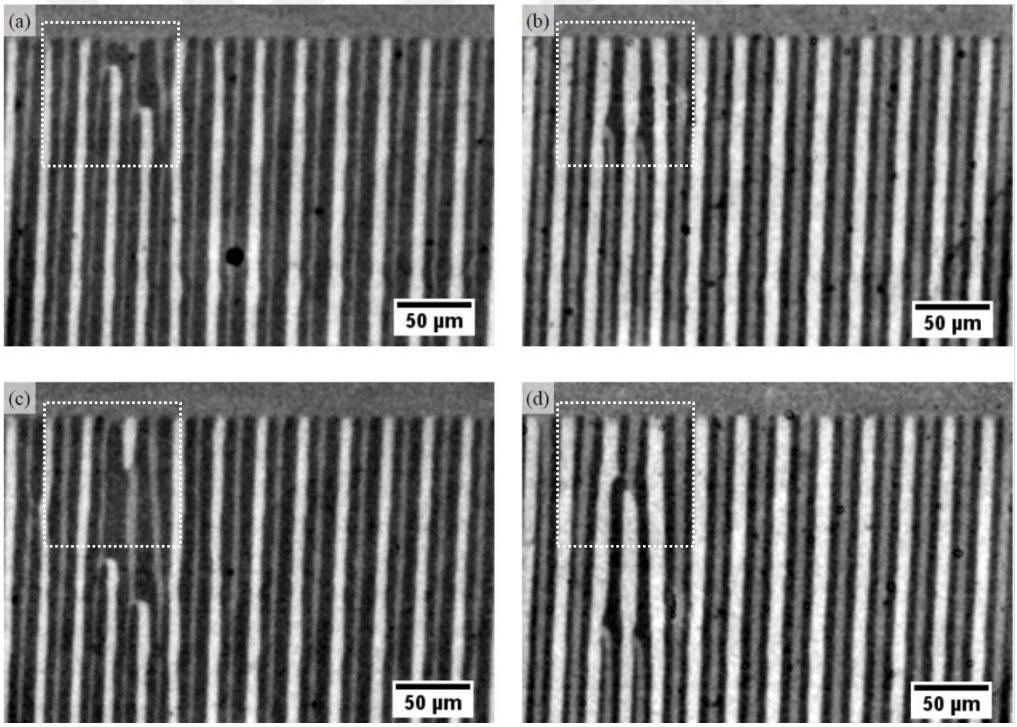

Figure 2-12. Phase-exchange mechanism observed after an elimination process. (a) Top view of the microstructure showing the elimination of AB phases belonging to 2 different ABAC motifs and formation of ACAC pattern. (b) Bottom view at the same time with (a) showing the elimination of AC phases belonging to 2 different ABAC motifs and formation of ABAB pattern. (c) Top view showing the phase exchange of B with the existing C phase. (d) Bottom

view at the same time with (c) showing the phase exchange of C with the existing B phase. The time difference between (a), (b) and (c), (d) is 345 seconds. V_i = 0.26 µm/s, V_f = 0.220 µm/s, G = 3.3K/mm, and δ = 23 µm. The positions of the events are marked on the microstructures with the white dashed rectangles.

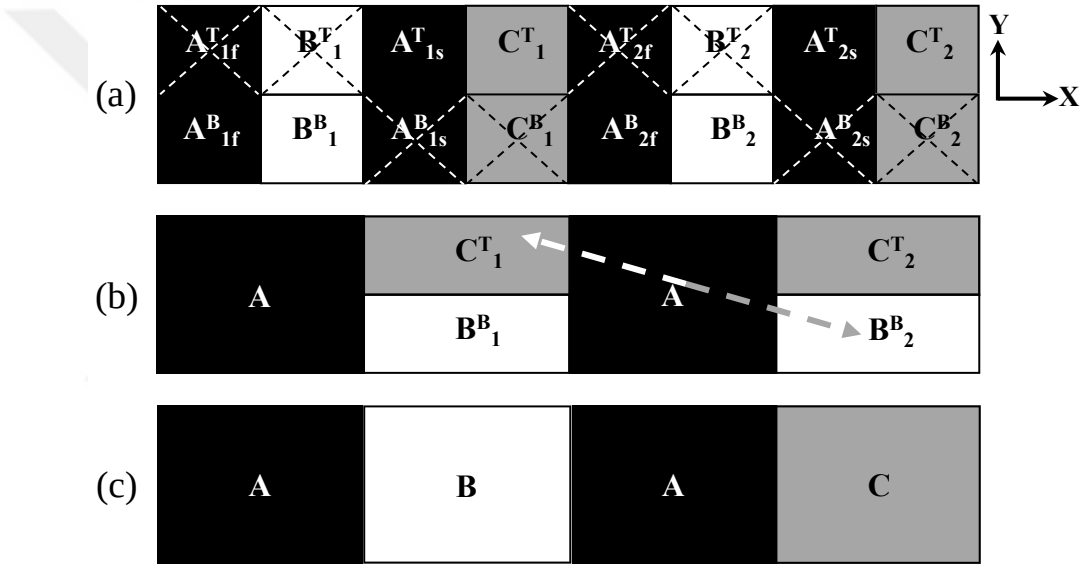

Figure 2-13. Schematic representation of phase-exchange mechanism through the thickness of the sample, *i.e.* in XY plane. (a) Configuration of two ABAC motifs right after the elimination processes. Eliminated phases are crossed for clarity. (b) Microstructure after A^T_{1s} is merged with A^B_{1f} and A^T_{2s} is merged with A^B_{2f}. Arrow points the phases that will be exchanged. (c) Final ABAC motif is obtained after the phase exchange of C^T_1 with B^B_2.

Figure 2-14 shows another example of the recovery after elimination in a slightly tilted ABAC pattern. In this example first B phase is eliminated and the recovery did not take place

at once. C phase oscillated through the thickness and after exchanging with B four times, it grows stably. Meanwhile, A and C phases in neighboring ABAC units are eliminated.

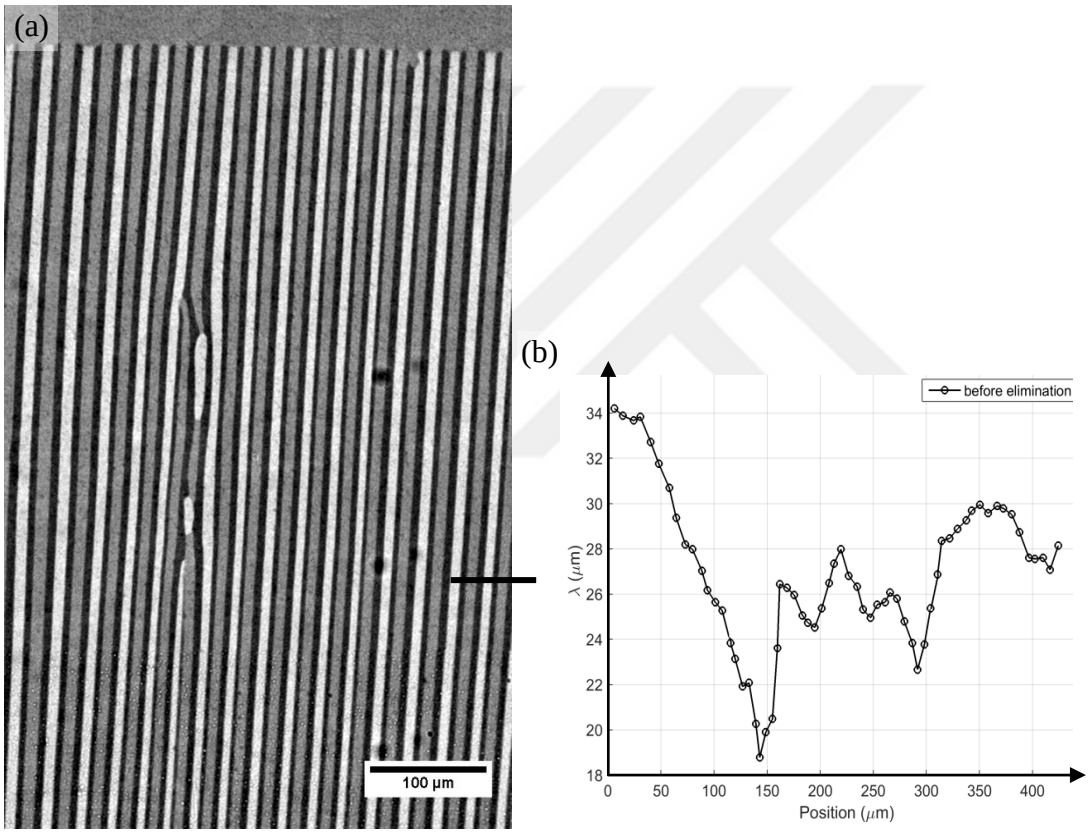

Figure 2-14. Oscillating lamellae within the thickness during an elimination event. (a) The ABAC pattern is recovered after an elimination is accompanied by continuous exchange between B and C phases, and elimination of an ABAC motif at last. (b) λ-plot taken before elimination shows a global minimum. The position where λ-plot was taken is marked on the microstructure in (a). the V_i = 0.230 μm/s, V_f = 0.200 μm/s, G = 3.3 K/mm, and δ = 50 μm.

2.3.3 Upper limit: lamellae branching

Branching happens when the spacing is more than the maximum value of the stability range (λ_{br}), which is generally observed after an upward velocity jump, *i.e.* when the initial velocity (V_i) is lower than the final velocity (V_f). However, it can also happen without any change in the growth velocity as in the case of Figure 2-15. Figure 2-15 shows the microstructure of a branching event along with the λ-plots at which branching location corresponds to a global maximum. All the λ values measured after the recovery of ABAC pattern, are within the stability limits of ABAC for the given velocity.

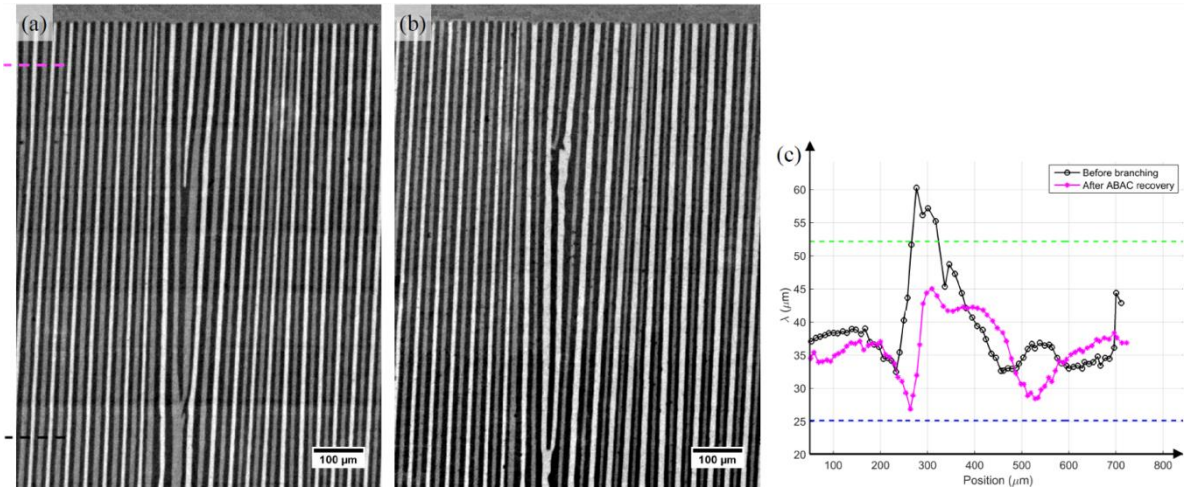

Figure 2-15. Branching instability occurred during a DS experiment. (a) Top view showing series of branching events resulting in ABAC pattern recovery. The dash lines show the locations from which the λ-plot measurements are done. (b) Bottom view of the same region with (a). (c) λ-plots corresponding to the regions before the onset of the branching and after

the recovery of ABAC pattern observed on top view of the sample. On the λ-plot, horizontal dashed lines on top (green) and bottom (blue) show the upper and lower stability limits, respectively, for V = 0.140 μm/s. λ^{T}_{br} = 60.3 μm, λ^{B}_{br} = 56.2 μm. δ = 23 μm and G = 3.3 K/mm.

The mechanism of branching instability in quasi-2D samples is found to be intrinsically a 3D process due to being accompanied by a particular phase-invasion mechanism in Y direction at the growth front. The mechanism of branching is explained here using the images given in Figure 2-16 as well as schematic representation shown in Figure 2-17 . In this case, 4 white phases are branched at the bottom view, while 4 black phases are branched at the top view of the microstructure. When we look at the time sequence of these events, it is clear that in each case of branching first black phase (A) is branched on top without any disturbance of the ABAC pattern at bottom. Afterwards, the branched arm in contact with the glass invades through the thickness of the sample (in Y direction) and finally reaches to the opposite side and divides the white phase (B) into two as schematically shown in Figure 2-7. As a result, both on top and bottom of the sample, regions with ABABAC order are formed and the lamellae configuration is the same. Hence, it is proven that nucleation is not happening during branching, but only growth is taking place.

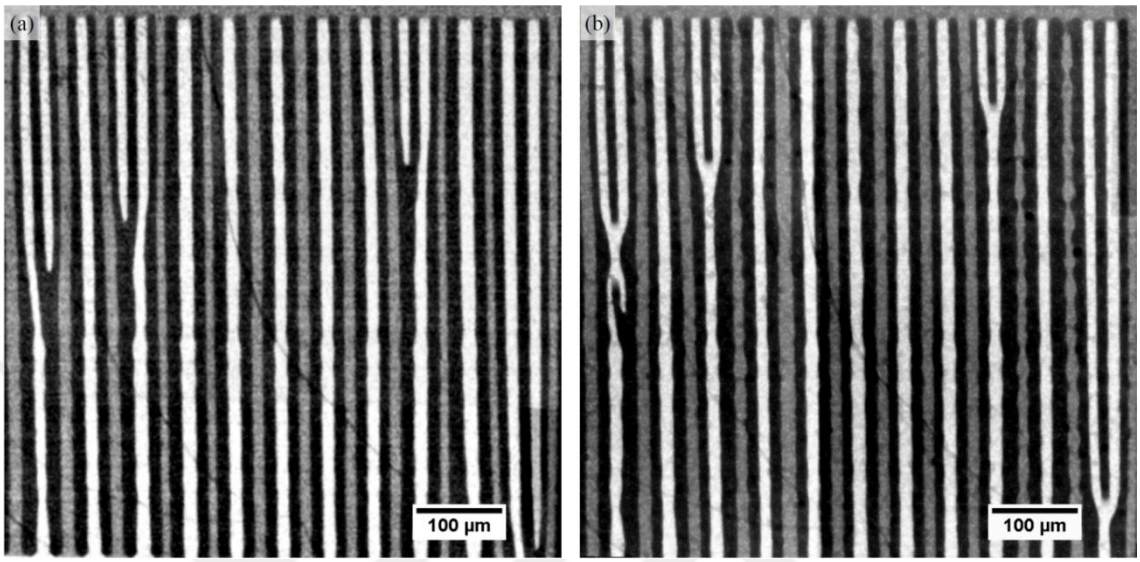

Figure 2-16. Branching instability observed in several lamellae. V_i = 0.080 µm/s, V_f = 0.110 µm/s. (a) Top view of the microstructure. (b) Bottom view of the microstructure at the same time with (a). δ = 23 µm and G = 3.3 K/mm.

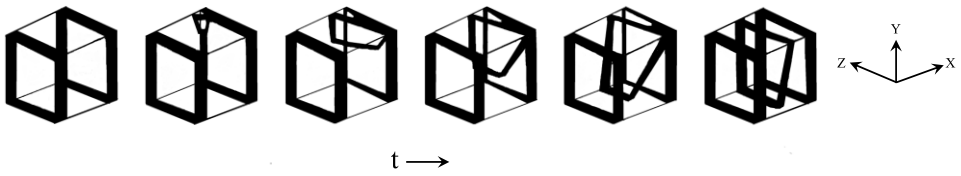

Figure 2-17. Schematic representation of branching instability with time (t). The microstructure evolves from left to right. The process is started with branching of black phase on top. Then the branched arm invades to the bottom of the sample, at which point, it makes the white phase branch by dividing it into two.

The time delay between top and bottom branching events verifies that through-thickness lamella invasion has a certain velocity. It is found that this velocity is dependent on experimental parameters and it is on the same order of magnitude with the growth velocity as shown in Figure 2-18. Through-thickness invasion velocity is much slower than the reported velocity of phase invasion process in lateral (X) direction [44]. In the latter case, phase invasion sweeps the solidification front very fast because the solid/liquid interface is highly undercooled due to the excessive solute accumulation. However, during branching, the solute built-up is localized, and hence, the through-thickness invasion velocity is on the same order of magnitude with the growth velocity.

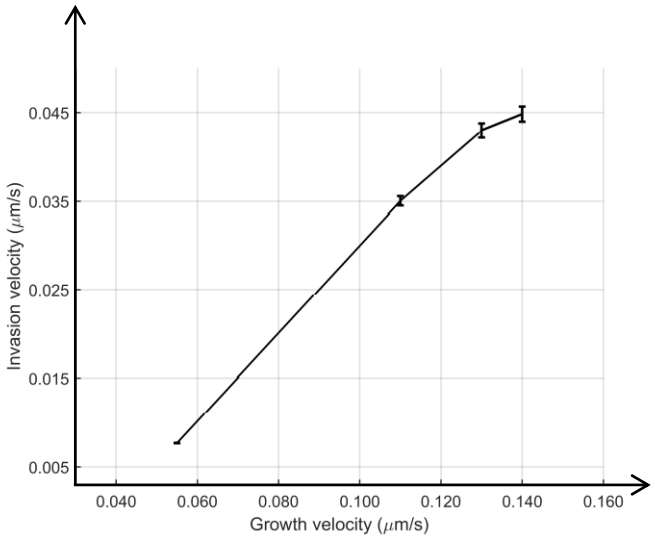

Figure 2-18. Invasion velocity as a function of growth velocity.

It was reported in 13 µm-thick samples that recovery of ABAC pattern after branching is unlikely due to difficulty in the required subsequent branching [70]. However, in this study, employing thicker samples, recovery of ABAC pattern after branching was observed as shown in Figure 2-15 (a, b) and by subsequent through-thickness invasion of phases. Figure 2-19 shows phase invasion cases observed in a 50 µm-thick sample. In these examples, branching of white phase resulted in ABABAC pattern, as usual. However, after the branching event, gray phase invaded in between branched arms of white phase, and divided the central black phase into two. As a result, in both of the cases, ABACABAC sequence is formed and hence ABAC pattern is recovered at the same velocity where branching occurred. This shows that increasing sample thickness activated some particular 3D mechanisms as a result of which even after branching, ABAC pattern is preserved. It should be noted that independent of sample thickness, eutectic spacing, velocity, and even type of branched phase, phase invasion can recover the ABAC pattern at the same velocity at which the spacing adjustment mechanism was occurred.

In addition to aforementioned mechanism, phase-exchange mechanism can also take place after branching to recover the ABAC pattern. In Figure 2-20, after branching, by means of two succeeding phase-exchange and one phase-invasion mechanisms, the ABAC pattern was recovered. Similar to the recovery after elimination by phase-exchange mechanism, replacement event occurs between B and C phases at the growth front, such that B (C) phase invades perpendicular to sample plane and then it exchanges with C (B) phase. There exists

another branching which results in a stacking defect, namely ABABAC, in the microstructure which disturbs the overall ABAC pattern. This defect continued to grow for about 1200 µm, where the end of the experimental run is reached.

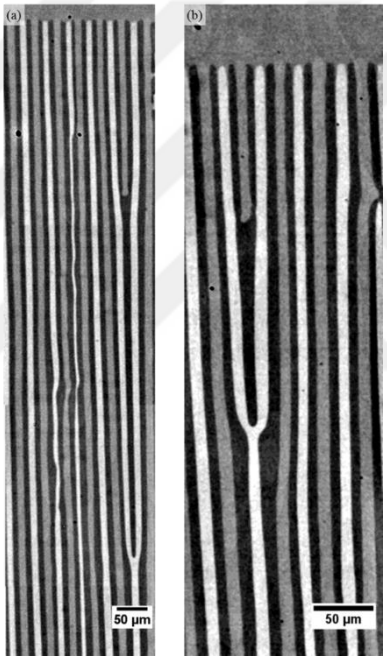

Figure 2-19. Recovery of ABAC pattern after branching instability by the phase-invasion mechanism. As a result of velocity change from 0.110 µm/s to 0.150 µm/s, branching of white phase took place. Later, gray phase invaded in between branched arms of white phase, and divided the central black phase into two. In (b), ABAC pattern is recovered much faster than the case in (a). δ = 50 µm and G = 3.3 K/mm.

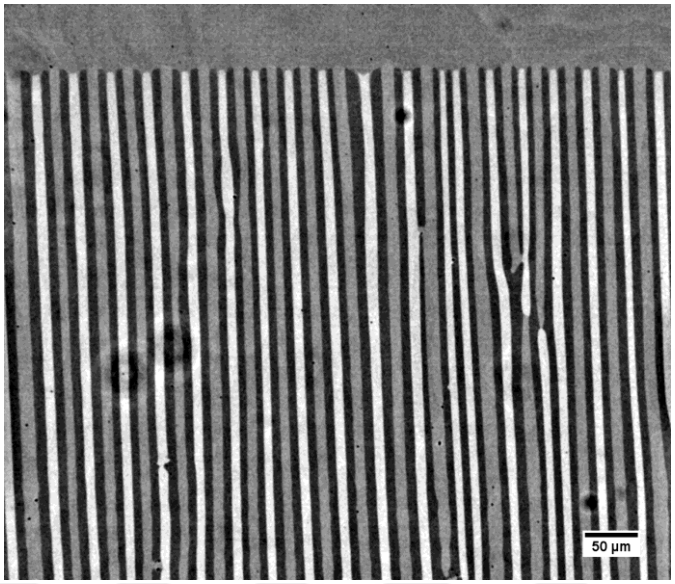

Figure 2-20. A complex example of phase-exchange mechanisms occurring right next to each other to recover ABAC pattern after branching. Following the phase-exchange events, invasion of C phase makes the A phase branch by dividing it into two. V = 0.180 µm/s, G = 3.3 K/mm, and δ = 50 µm.

In all phase-exchange events observed within this study, the replacement occurred between B (β-In) and C (γ-Sn) phases. When the composition of each phase is examined Table 2-1, compared to the invariant eutectic composition, it can be seen that during "tripled" growth, the main solute exchange is in between A and C for In and Sn, while Bi is mainly exchanged between A and B. More specifically, ABAC is probably stable because this kind of phase arrangement minimizing the diffusion length when A phase is In_2Bi for this three-phase system. Furthermore, recovery mechanisms after branching were only observed when

the phase arrangement on top and bottom of the sample was different. In other words, invasion and exchange of β-In and γ-Sn phases may occur only when there is excess In and Sn locally at the solidification front.

As it is argued, the requirement to activate the recovery mechanisms is that the phase arrangement in the sides of the sample should not be the same. This means that a 3D fault exists in the phase arrangement, *i.e.* different phases exist at the same X location at the sides of the sample. For example, in the case shown in Figure 2-20, the stacking fault next to the recovery region was not recovered until the growth front reached to the end of the sample. Interestingly, it was observed that when the lamellar arrangement is the same at the top and bottom views, *i.e.* there is no 3D fault in the arrangement, sometimes the system spontaneously generates a 3D fault in the arrangement in order to enable the recovery. Figure 2-21 (a and b) shows the microstructure resulting from successive branching events where numerous ABABAC faults formed in the ABAC arrangement. One can realize that identical phase arrangement exists at the top and bottom views of the sample and in such circumstances, the recovery does not occur. Figure 2-21 (c and d) shows the microstructures from top and bottom views after 2290 μm growth length. In one occasion of ABABAC structures, the C phase on the bottom view develops double branching and as a result of that, the phase arrangement on top and bottom is not the same anymore. It should be noted this event occurred spontaneously without change in the velocity. In the next step, through one

exchange and one invasion mechanisms on the bottom side and one invasion on the top side, the ABAC is locally recovered in both sides of the sample in the region of interest.

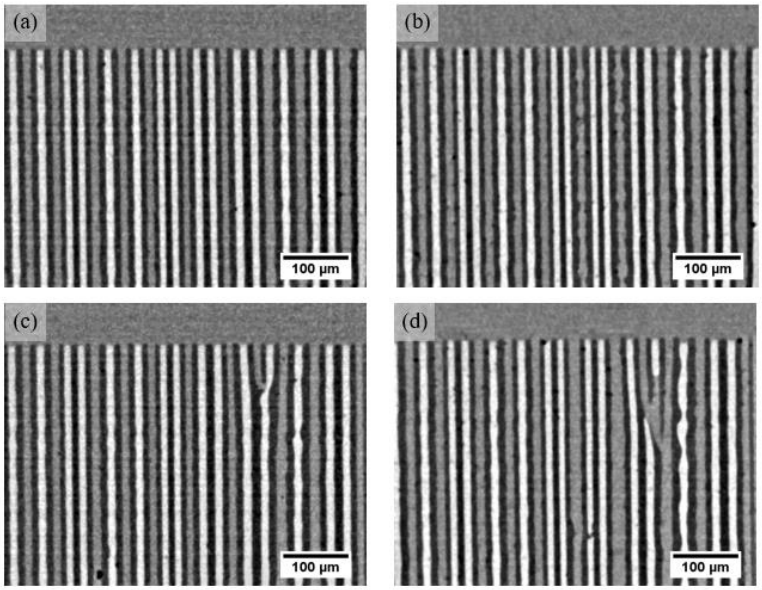

Figure 2-21. Recovery mechanism in the absence of initial dissimilarity in the phase arrangement. (a) Top view of the microstructure having ABABAC stacking faults. (b) Bottom view of the microstructure with the identical arrangement as the top microstructure. (c) Top microstructure after 2290 µm growth length. (d) Bottom microstructure showing double branching of C phase at the right side of the image. One of the branched C arms is exchanged with one of the B phases at the fault and the second branched arm invades to the other side of the sample. V = 0.150 µm/s, G = 3.3 K/mm, and δ = 23 µm.

Even though the phase-exchange and invasion phenomena cannot be theoretically explained yet, it is obvious that the system stimulates these complicated mechanisms to achieve the ABAC pattern, which is the stable and basic stacking in three-phase eutectic systems. It is believed that employing quasi-2D samples activated these mechanisms, which are inherently 3D and absent in a real 2D geometry. In other words, the samples used in this study are thick enough to accommodate two different phases through the thickness of the sample for a short amount of time.

2.3.4 Oscillation instability

In the examined sample thicknesses, oscillation instability is rarely observed, and the upper limit of the stability is always bounded by branching instability. This can be due to fact that by increasing sample thickness, the intrinsically 3D mechanisms such as branching can take place easily. While the oscillations of any mode are the efficient mechanism in purely 2D samples, by decreasing confinement effect, 3D mechanisms are more active. Figure 2-22 shows a low amplitude 1λ-oscillation which eventually branched.

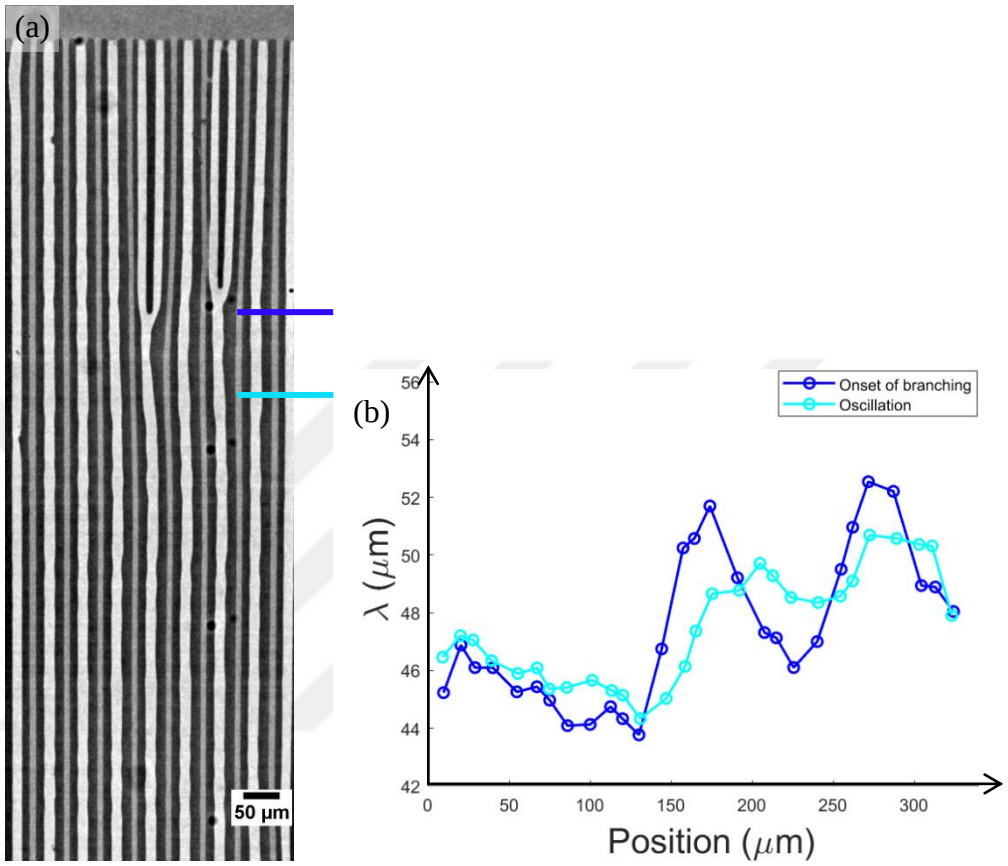

Figure 2-22. Low amplitude 1λ-oscillatory mode followed by branching instability. (a) Marked positions on the microstructure are the positions where the spacing measurements were taken. The blue and cyan lines resemble the onset of branching and during oscillation, respectively. (b) The eutectic spacing plot corresponds to the marked regions in (a). V = 0.130 µm/s, G = 3.3 K/mm, and δ = 50 µm.

In Figure 2-22 (b) two maxima in the eutectic spacing values at 51.7 and 52.5 µm occurred at positions of 174.0 and 271.8 µm respectively, corresponding to the onset of the branchings. These maxima also exist in the oscillation position, with lower spacing values. It can be concluded that even though the oscillation mechanism is still active in the quasi-2D

geometry, it is first not stable, *i.e.* it is ended either by branching instability or damped over time. Secondly, the amplitude of the oscillation is considerably low compared to the oscillations occurred in 2D samples.

2.3.5 Stability diagram of ABAC pattern for quasi-2D samples

The stability diagram of the ABAC pattern can be defined by the eutectic spacing (λ) as a function of growth velocity (V). The maximum and minimum in the eutectic spacing values corresponding to the onset of branching and elimination events resemble the upper and lower limits of the stability region for the given sample thickness and velocity. It should be mentioned that since the thickness of the Mylar spacers are used increased by a factor of two, the sample thicknesses are categorized based on the Mylar spacer thicknesses and not by the exact sample alloy thicknesses. The thresholds are compared with the previous study on 13 µm-thick sample [70, 74], to examine the effect of increasing sample thickness on the stability region. Figure 2-23 illustrates the stability diagram.

It is found that the elimination threshold (λ_c) in thicker samples are still in good agreement with those of 13 µm-thick samples. This can be related to the mechanism behind the elimination process. It was discussed in *section 2.3.2* that the elimination process has some 3D features, however, the overall mechanism is the termination of four phases and recovery of the ABAC pattern all the time. It should not be surprising that by decreasing

confinement effect elimination mechanism is not significantly affected. This contrasts with the threshold of branching instability (λ_{br}). It was shown in *section 2.3.3* that branching event is complete a 3D mechanism which is accompanied by generation of a newly branched arms from the parent phases. It is known that such a 3D mechanism is absent in real 2D samples wherein the stability regime was bounded by oscillation and tilted structures [24]. Therefore, it was expected that by the decreasing confinement impact on the growth, the 3D mechanisms such as branching readily takes place. That leads to the occurrence of branching at lower eutectic spacings in thicker samples compared to the thinner ones at a given velocity. The final outcome of this event, indeed, will be the shrinkage of the lamellar ABAC pattern stability regime by increasing sample thickness.

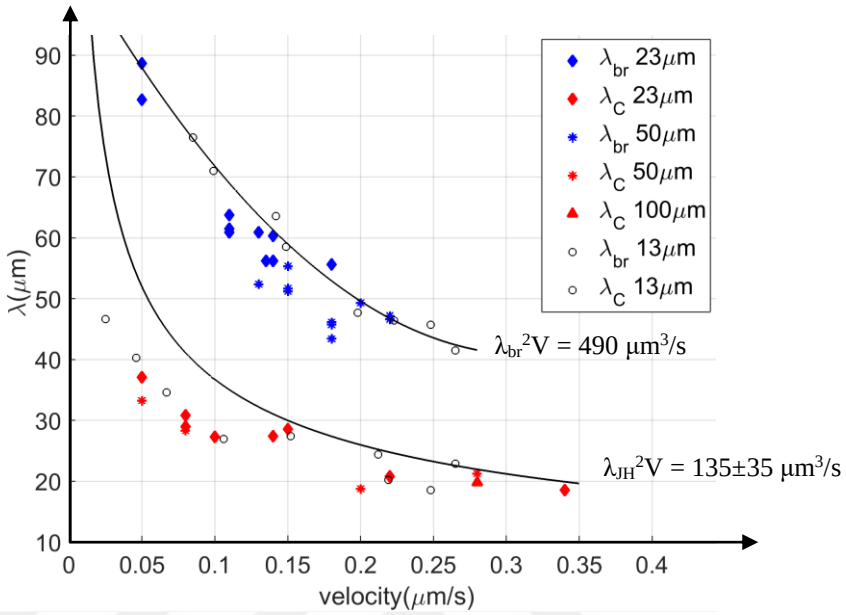

Figure 2-23. Stability diagram of the ABAC-type growth pattern. The upper and lower limits of the stability regime are shown by blue and red colors, respectively. The fitted curves correspond to λ_{JH} and the threshold of the branching (λ_{br}) in 13 µm-thick sample [70].

2.4 Conclusion

In this chapter, using quasi-2D samples of In-Bi-Sn system at eutectic composition, it was experimentally shown that for the ABAC basic pattern, the spacing adjustment mechanisms observed beyond the lower and upper stability limits are elimination and branching, respectively, as reported in much thinner samples [70]. For the employed experimental conditions, while the microstructure is necessarily 2D during steady-state growth, *i.e.* top and bottom microstructures are the same, 3D features were observed during spacing adjustment mechanisms. 3D features of these instabilities, including the start of the

elimination and branching on one side of the sample while ABAC continues to grow on the other side of it and the different sequence of eliminating or branching phases on the sides of sample, are characterized using, for the first time in the literature, the double-sided microscopy system. These 3D features result in observation of totally different microstructure at the sides of the sample while spacing adjustment mechanisms are taking place. Both elimination and branching start with one phase, which can be any of the three phases present in the microstructure. After these instabilities, two key ABAC pattern recovery mechanisms, namely, phase-invasion and phase-exchange mechanisms were identified and analyzed. Phase-exchange mechanism is the exchange of β-In (B) and γ-Sn (C) phases along the solidification front where In_2Bi (A) phase provides a path for these phases to invade through the thickness of the sample. Phase invasion is the mechanism where a phase is propagating in Y direction, *i.e.* perpendicular to the growth direction (Z). ABAC pattern is always recovered after elimination at both sides of the sample, even though the phase, time, sequence, and mechanism of eliminations are different on the sides of the sample. Elimination can take place by cease of a phase from the solidification front or by merging of 2 phases of the same kind. After elimination, ABAC pattern is recovered by either continuous eliminations of all phases or by phase-exchange mechanism. Particularly, when the phase sequence is different at the sides of the sample, phase-exchange mechanism is observed to be used to recover the ABAC pattern at both sides of the sample. In the case of branching, it was shown that branching does not include nucleation process as already predicted in two-phase systems. With innovative double-sided microscopy system, it was

observed that the branched arm grows through the thickness of the sample by dividing the neighboring phase into two. Hence, only growth takes place in branching and it can only occur in quasi-2D and 3D samples. The recovery mechanisms after branching are established to be phase invasion, phase exchange or their combinations. Despite the recovery of ABAC pattern all the time after elimination, the system could not always get rid of the stacking defects such as ABABAC patterns after branching. It is worth to note here that the pattern recovery employing aforementioned mechanisms, *i.e.* phase exchange and phase invasion, were only observed when the phase arrangement at a given X position at the solidification front are different on the sides of the sample. If the arrangement is identical, it was observed in several occasions that the system spontaneously forms a fault in the stacking sequence to enable recovery. That can be related to the fact that the examined samples are thick enough to accumulate different phases within the thickness of the sample, but only temporarily.

In the examined thickness range, rare occasions of 1λ-oscillatrory mode were detected, which all either followed by branching event or damped over time. With decreasing the confinement effect, it is shown that 3D mechanisms such as branching occur easily and that suppress the instabilities such as oscillations, which are mostly mechanisms in truly 2D geometry.

The thresholds of the instabilities in thicker samples were compared to the ones in the thinner one (~13 μm). It is found that the elimination threshold is not changed; however, the branching limit is shifted towards lower spacing values at a given velocity. This effect results

from the underling mechanisms of these instabilities. It is believed that 3D mechanisms such as branching easily takes place in the thicker samples, where the lamellar structure gains the degree of freedom within the thickness of the sample. Such a trend ultimately leads to shrinkage of the stability regime of lamellar ABAC pattern by decreasing confinement effect.

Chapter 3 : Three-phase eutectic growth in thin samples during rotating directional solidification

3.1 Introduction

As it is discussed in *Chapter 1* and *2*, the fundamental theory of eutectic growth was proposed by Jackson and Hunt in 1966 has the simplification assumption that the solid/solid (S/S) interphase is isotropic in two-phase eutectic systems. In this circumstance, the steady-state periodic lamellar structure is expected to grow parallel to the imposed thermal gradient upon directional solidification (DS) of thin samples. This means that the surface energy of S/S boundary is essentially orientation-independent. In directional solidification experiments, one can only observe the growth dynamics in one direction, which is the direction of the growth or the imposed thermal gradient. In other words, considering 2D-section of Wulff plot of the S/S interphase boundary energy, the behavior of it in other crystallographic orientations cannot be examined during DS experiments. Generally speaking, one can call eutectic grains (EG) isotropic, only if the magnitude of the interphase energy is constant over all crystallographic orientations. In other words, the surface energy does not contain any kind of minima in any direction. Therefore, the expected 2D-section of Wulff plot of the interphase boundary is a circle. The equilibrium shape, which is the shape that minimizes the surface free energy integrated over the entire surface, has a circular shape, shown schematically in Figure 3-1.

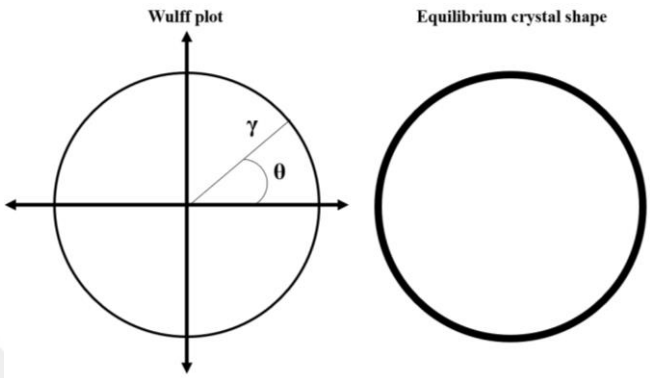

Figure 3-1. 2D-section of Wulff plot for an isotropic surface energy and the corresponding equilibrium crystal shape.

3.1.1. RDS experiment principles

Rotating directional solidification (RDS) is an experimental method, which provides the quantitative information about 2D-Wulff form of the S/S energy. The main concept of the method is to keep all the parameters fixed in directional solidification technique and vary only orientation of the S/S interphase with respect to imposed thermal gradient direction. During RDS experiment, a EG is rotated continuously at a fixed thermal gradient field to examine the behavior of the S/S boundary in all crystallographic orientations, *i.e.* over 360° rotation of the sample. Combining RDS experimental method with in-situ observation was a breakthrough in identifying the S/S anisotropy effect on the solidification pattern formation. S. Akamatsu *et al.* developed a semiempirical theory on the effect of S/S interphase

anisotropy on the lamellar growth [75, 76] in two-phase systems. Using the RDS method, they showed the formation of an isotropic eutectic grain in CBr_4–C_2Cl_6 and In–In_2Bi binary systems (Figure 3-2). In this type of eutectic grain, lamellar trajectories stay normal to the solidification front during an RDS run. In other words, since the S/S energy is orientation-independent, the lamellae trajectories follow the direction of the thermal gradient. Therefore, their trace left in the solid by the propagating S/L interface in one turn of RDS experiment is a circle.

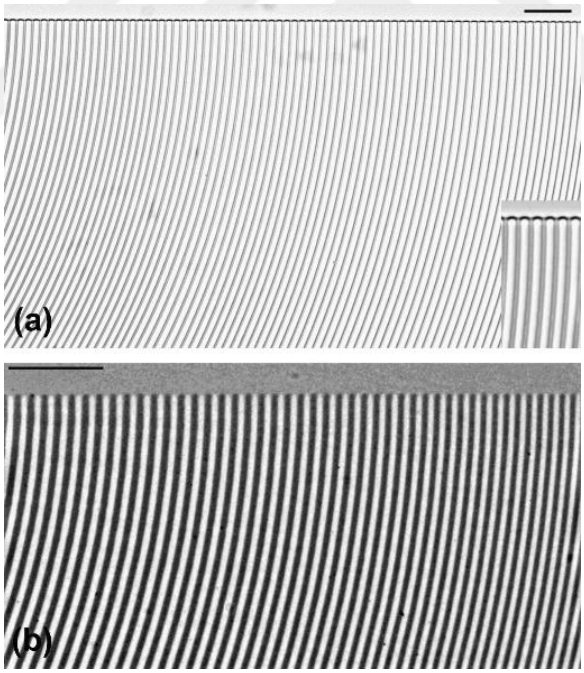

Figure 3-2. Lamellar trajectories in RDS experiments of isotropic eutectic grains in two-phase systems. (a) CBr_4-C_2Cl_6 organic system. (b) In-In_2Bi metallic system [77].

In this chapter, the existence of a so-called isotropic eutectic grains in In-Bi-Sn three-phase system over the entire crystallographic orientation will be discussed. In other words, does the isotropic EG in the three-phase systems evolve floatingly over 360º rotation of the sample during RDS experiments. If yes, it would mean that both interphase boundaries of the system, *i.e.* AB and AC, must essentially be orientation-independent. Furthermore, it will be investigated if the ABAC basic state will be preserved during the evolution of the initially isotropic grain during an RDS experiment.

3.2 Experimental procedure

RDS setup configuration

RDS setup consists of a hot and a cold zone made of copper blocks with an adjustable gap in between these zones. The sample is fixed inside the sample holder and sandwiched between the blocks. The setup has one motor to enable directional movement and another one to rotate the sample in XZ plane. The blocks, sample holder, and motors are assembled and situated on the double-sided microscope stage to acquire real-time images of the solidification front from top and bottom sides of the sample. Schematic of the setup is shown in Figure 3-3.

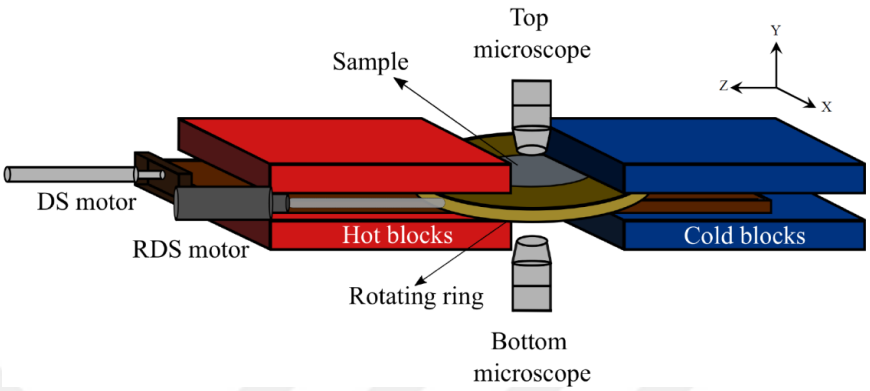

Figure 3-3. Schematic representation of the RDS setup.

RDS experiments are started in the channel region of the sample to be able to select the desired EG. Large EG is formed by growing the pattern directionally at a constant velocity. When the solidification front reaches the equipment's center of rotation, Ω, the directional movement is stopped while the rotational movement at a constant angular speed, ω, is started. The time (t) and S/L interface position (P) at this moment will be taken as the reference starting points in an RDS run, *i.e.* t_0 and P_0 are the time and interface position at the beginning of the rotation, schematically shown in Figure 3-4 (a). While the sample is rotating on XZ plane around Ω, half of the sample width is solidifying whereas the other half is melting as it is represented in Figure 3-4 (b). The rotating motion induces a growth velocity gradient at the solidification front. The growth velocity is zero at the center, which results in a single-phase formation [78, 79]. As the velocity increases from the center to the edge of the sample (proportional to xω, where x is the distance from the center of rotation, Ω) first two-phase

and then three-phase structures are formed. As growth velocity increases towards the edge of the sample, the three-phase eutectic spacing consistently decreases. Therefore, while coarser scaling is observed close to the center, fine eutectic patterns form at the perimeter of the circular sample. One can obtain full evolution of the pattern by taking regular mosaic images of the whole front and reconstruct them in the form of a panoramic image. It should be noted here that while the sample is rotated clockwise, the pattern grows counterclockwise and vice versa.

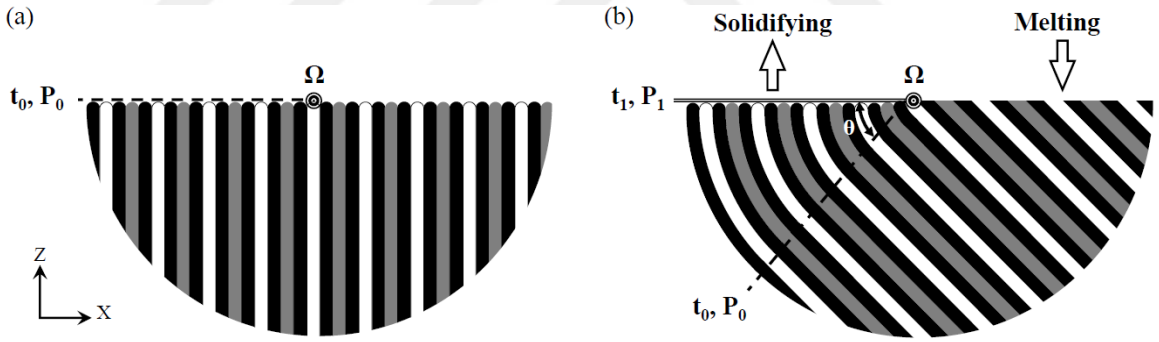

Figure 3-4. (a) Schematic microstructure obtained in a standard DS experiment when the solidification front reaches to the center of rotation, Ω. The time and position at which rotation is started are defined as t_0 and P_0. (b) Microstructure obtained after θ degrees of rotation in counterclockwise direction. The microstructure grows in clockwise direction. Right side of the sample is melting while the left side is solidifying. S/S interphase boundaries follow the trajectory of the rotational motion.

The position at which the S/L interface reaches the center of rotation is determined by the setup. Ideally, if the S/L interface is right at the center of rotation, *i.e.* Ω, the trajectory of the motion will be circle with an origin at Ω. However, experimentally, it is very hard to be perfectly at the center of rotation and the front is always slightly below or above Ω along the Z axis. This leads to a centripetal and centrifugal motion of the trajectories for $P_0 < \Omega$ and $P_0 > \Omega$, respectively. As a result, in a floating grain, the trajectory of an S/S interphase boundary forms a spiral instead of a circle.

3.3 Results and discussion

3.3.1 Floating (Isotropic) eutectic grains

In the isotropic EG, all surface energies (γ) of interphase boundaries are crystallographic orientation independent. For the ABAC pattern, it means that the surface energies of both AB and AC interphase boundaries, *i.e.* γ_{AB} and γ_{AC}, are isotropic. For an isotropic EG, the γ-plots, *i.e.* surface energy plots as a function of orientation, of both γ_{AB} and γ_{AC} are forming a circle. The equilibrium at the triple-point junctions, thus, follows the Young's law:

$$\gamma_{AL} + \gamma_{BL} + \gamma_{AB} = 0 \text{ and } \gamma_{AL} + \gamma_{CL} + \gamma_{AC} = 0$$

Where γ_{AL}, γ_{BL}, and γ_{CL} are the surface energies between the indicated solid phases with the liquid.

Figure 3-5 illustrates the schematic representation of an ABAC motif in an isotropic three-phase eutectic system along with the associated surface energies.

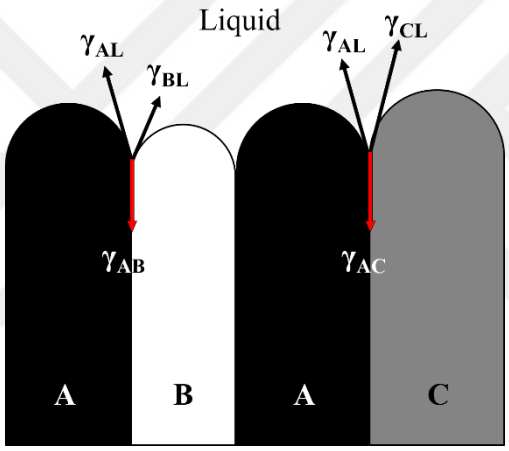

Figure 3-5. Schematic microstructure showing the two different triple-point junctions existing in an ABAC pattern. In an isotropic EG, surface energy of two boundaries, *i.e.* γ_{AB} and γ_{AC} are parallel to the growth direction.

In an isotropic EG, interphase boundaries are continuous from top to the bottom of the sample. In other words, each phase in an ABAC pattern is a lamella. This can be confirmed by having the identical microstructures on top and bottom views of the sample during an RDS experiment, as shown in Figure 3-6.

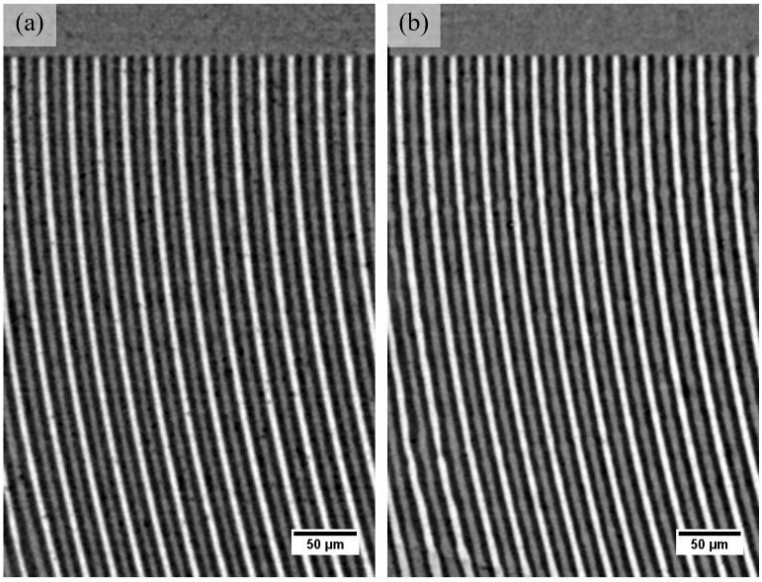

Figure 3-6. ABAC lamellar structure during an RDS experiment. (a) Top microstructure. (b) Bottom microstructure. CW, $\omega = 0.013$ °/s, and $\delta = 13$ µm.

An example of isotropic EG with ABAC pattern is shown in Figure 3-7. First, the sample was directionally solidified and close to the center of rotation, the directional growth was stopped, and the rotational movement was started. The image was taken when the sample is rotated 46º. In the isotropic EG, the ABAC pattern rotates floatingly and the triple-point junctions are following the direction of the thermal gradient. In Figure 3-7, as a result of continuous rotation of the sample, each interphase boundary is forming an arc of a spiral. Close to the center, irrespective of the grain type and experimental run, the pattern was commonly disturbed due to having a growth velocity close to zero.

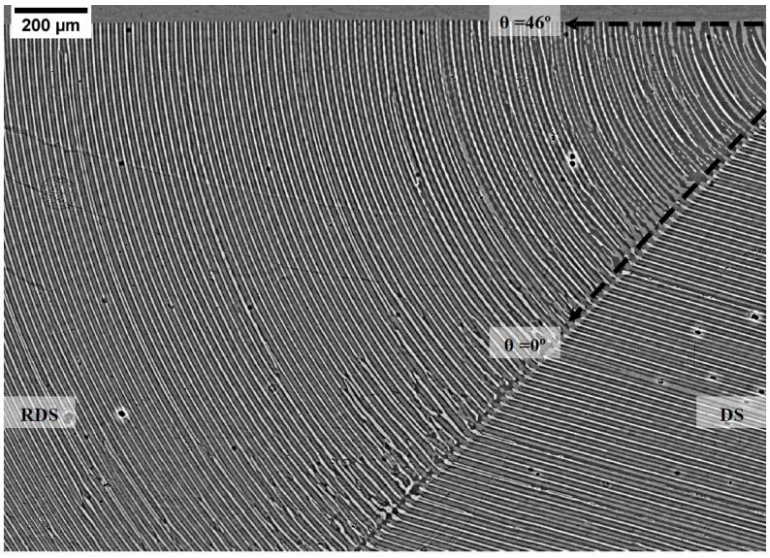

Figure 3-7. The isotropic EG with ABAC arrangement subjected to rotational motion. The pattern continues to grow by the onset of the rotational motion with ABAC arrangement. Bottom-right part is grown with DS, top-left side is grown by RDS. The perturbation in the pattern at $\theta = 0^{o}$ was due to start of RDS and stop of DS. CW, $\omega = 0.013$ °/s, G = 5.1 K/mm, and $\delta = 13$ µm.

Similar to the isotropic EG formed during DS experiments, both interphase boundaries are perpendicular to the growth front during the RDS experiment. Figure 3-8 shows close snapshots of the solidification front of isotropic EGs during DS and RDS experiments.

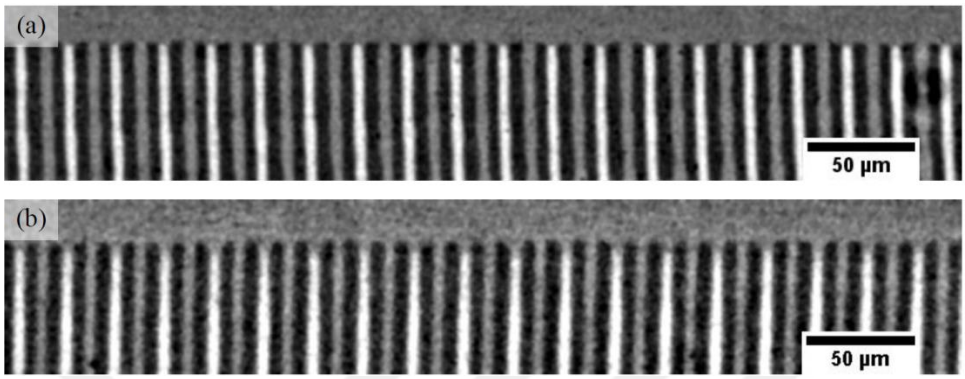

Figure 3-8. Comparison of the interphase boundaries observed during isotropic EG formed during RDS and DS experiments. (a) Isotropic EG in an RDS experiment. ω = 0.013 °/s, G = 5.1 K/mm, and δ = 13 μm (b) Isotropic EG in a DS experiment. V = 0.400 μm/s, G = 5.1 K/mm, and δ =13 μm.

Figure 3-9 shows the evolution of the ABAC pattern over 360º rotation of the sample. Regular ABAC pattern is preserved in entire orientation and this ensures that the EG is isotropic. In this example, the pattern is centripetal spiral and the position of each phase and interphase boundary can be fitted to the logarithmic spiral equation, *i.e.* r (θ) = *a*exp (*b*θ), where r is the distance from the origin, θ is the angle from the X-axis and *a* and *b* are constants. For the AC and AB interphase boundaries in Figure 3-9, the trace of the boundaries and the fitted logarithmic spiral equations are shown in Figure 3-10 and Table 3-1, respectively.

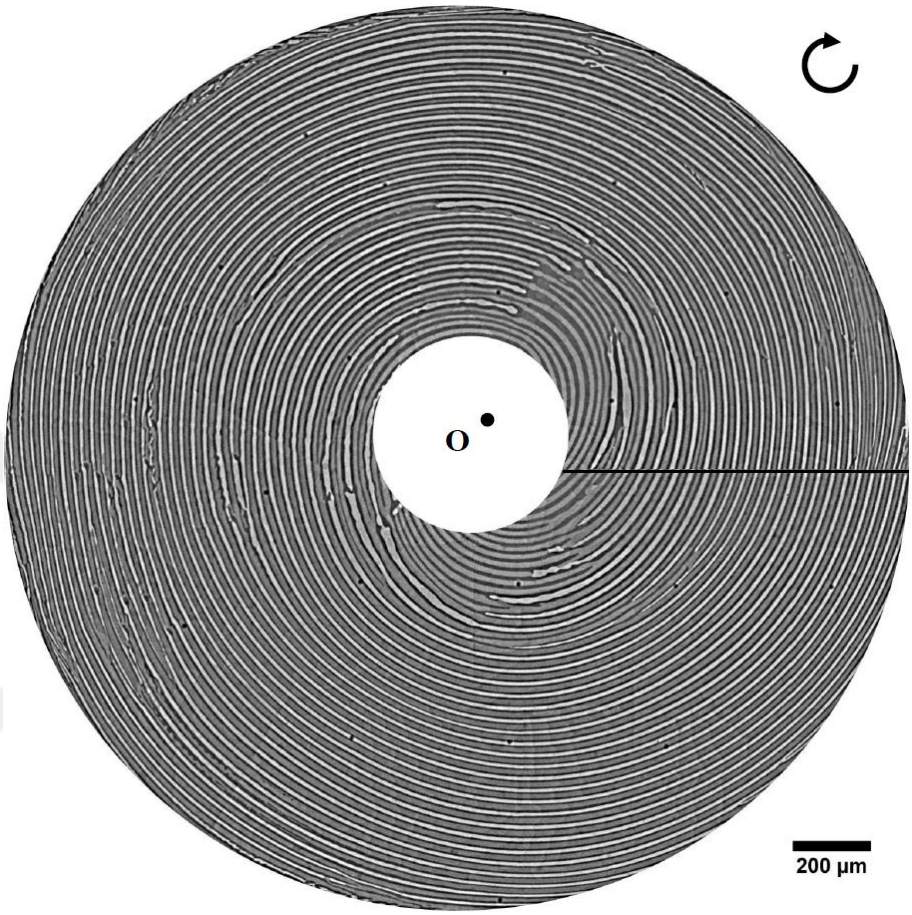

Figure 3-9. The evolution of the ABAC pattern in RDS experiment over 360º rotation of the sample. The pattern is centripetal spiral. The center of the spiral is marked (O). The horizontal line is separating the start and end of one turn rotation. CW, ω = 0.019 º/s, G = 5.1 K/mm, δ = 13 µm.

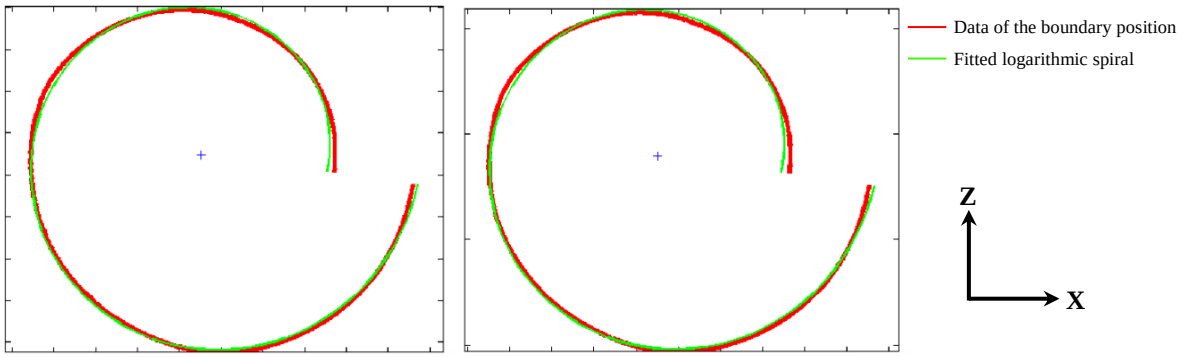

Figure 3-10. The trace left by the boundaries during an RDS experiment and the corresponding fitting to the logarithmic spiral equation. (a) AC boundary. (b) AB boundary. The red curves are the trace of the boundaries and the green curves are the fit obtained by using logarithmic spiral equations given in Table 3-1. Blue plus mark is the center of the fitted spiral.

Table 3-1. The logarithmic spiral equations fitted on two interphase boundaries of an isotropic ABAC pattern.

Interphase boundary	**Spiral equation**	**rms (μm)**
AC	$r = 618.3\, e^{-0.09\theta}$	11.6
AB	$r = 601.7\, e^{-0.09\theta}$	11.9

During RDS of an isotropic ABAC pattern, elimination and branching spacing adjustment mechanisms were observed, as shown in Figure 3-11, when the eutectic spacing goes beyond the lower and upper stability limits, respectively, as in the case of DS experiments [70]. Additionally, the same types of recovery mechanisms observed in isotropic

EG grown by DS, discussed in *chapter 2*, took place in EG growing floatingly during RDS. Owing to these mechanisms, ABAC pattern is adjusting its spacing at different velocities and it is recovered. Since these mechanisms are commonly ineffective in anisotropic EG, the presence of them in RDS pattern also confirms that the EG is isotropic.

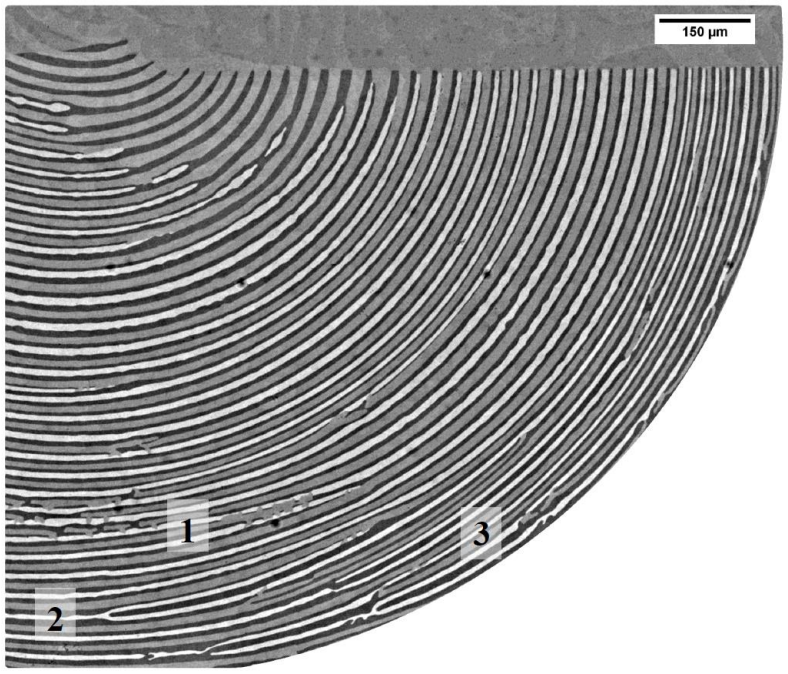

Figure 3-11. Spacing adjustment and recovery mechanisms observed during RDS of an isotropic ABAC pattern. Marked points are (1) Elimination. (2) Branching. (3) Recovery by phase-invasion mechanism within ABAC pattern during RDS. CCW, $\omega = 0.016$ °/s, G = 5.1 K/mm, and $\delta = 13$ µm.

3.4 Conclusion

In this chapter, the formation of the isotropic (floating) eutectic grains as a function of orientation of the interphase boundaries in three-phase system was investigated using RDS method. It is shown that in the absence of the anisotropy in both of the interphase boundaries in ABAC growth pattern, the triple-point junctions of the pattern floatingly follow the thermal gradient direction. Therefore, the interphase boundaries are perpendicular to the solidification front. In this case, the interphase energy is not a function of orientation and the expected 2D Wulff plot of both AB and AC boundaries are circles. Trajectories of the interphase boundaries in one turn of the sample form spirals instead of circles due to experimental difficulties about being right at the center of rotation. The boundaries could be fitted to logarithmic spiral equations with low rms values. In this type of grain, dynamics of ABAC lamellar growth is controlled by the eutectic adjustment mechanisms, namely elimination and branching during RDS experiment. Systematic occurrence of these mechanisms ensures that the grain is isotropic since they are not effectively active in an anisotropic eutectic grain. The ABAC pattern recovery mechanisms, such as phase-invasion reported in DS experiments operates efficiently in isotropic EG during RDS as well.

It should be mentioned here that orientation independency, in general terms, does not mean zero degree of anisotropy of the surface energy. Particularly, in terms of crystal/crystal interphase, there always exists some sort of anisotropy related to crystal lattice and misorientation of two different crystals with respect to each other. However, in isotropic

pattern the anisotropy related to the crystal lattice is probably weak in this case and does not affect the overall dynamics. In other words, the processes that control the microstructure in the isotropic ABAC pattern are phase-diffusion, eutectic spacing adjustment, and pattern recovery mechanisms.

The similarities in specific features of isotropic eutectic grains observed in two-phase and three-phase systems on one hand, consistency of these features between the nearly steady-state DS and RDS patterns on the other hand, highlight that the characteristic of the isotropic grain growth are the inherent properties of the eutectic grain, irrespective of the system.

Chapter 4 : Three-phase eutectic growth in the presence of S/S anisotropy in quasi-2D samples, Part A

4.1 Introduction

The energy of the interface between two phases is usually orientation dependent. The degree of anisotropy depends on the structure of the phases in contact and how they are oriented with respect to each other. For a small degree of anisotropy, the equilibrium shape is non-spherical but still smooth, *i.e.* one can get tangent of the whole interphase energy plot. On the other hand, if the energy contains deep minima in certain directions, the corresponding orientations are cusps in the Wulff plot. As a result of the cusps in the plot, the equilibrium shape of crystal has straight edges known as facets [80]. For very large anisotropy (deep cusps), certain orientations will be missed in the equilibrium shape, known as missing (forbidden) orientations. For instance, the anisotropy function for a hypothetical surface energy shown in Figure 4-1 has a four-fold symmetry with deep cusps singularities. The resulting equilibrium shape, thus, has four facets in the crystal equilibrium shape shown by solid lines and has '*ears*' shown by dashed lines, which shows the range of forbidden orientations.

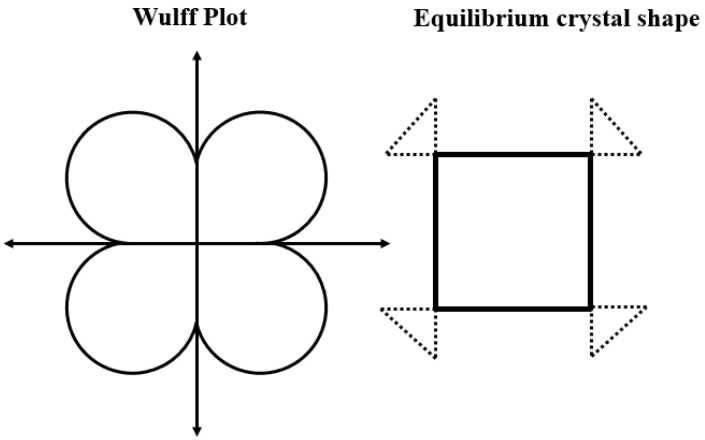

Figure 4-1. Hypothetical Wulff plot of an anisotropic surface with strong, four-fold anisotropy function. The Wulff plot has four cusp singularities and as a result of them, the equilibrium shape, shown by solid lines, has four facets. Dashed lines show the extend of forbidden orientations.

In the case of anisotropy in S/L interfaces, there are several methods to determine the anisotropy, experimentally. Measurement of the maximum undercooling required for the onset of nucleation [81], grain boundary groove method [82, 83], direct measurement by characterizing the equilibrium shape of solid particles in a liquid or liquid droplet in a solid, in transparent materials [84] and metallic materials [85] are some examples.

Numerical studies to construct the orientation dependency of the interfacial energy between two phases using phase-field modeling has been considered long ago. J. J. Eggleston *et al.* developed a successful model by incorporating the missing orientations in the case of very strong anisotropy in their phase-field model [86]. Figure 4-2 illustrates the results of

this study where the equilibrium shapes resulting from various degrees of anisotropy with four-fold symmetry are shown. Evolution from spherical shape that does not contain any anisotropy (a) to a square in the case of strong anisotropy (f) is successfully predicted. The '*ears*' in the equilibrium shape was removed from these images.

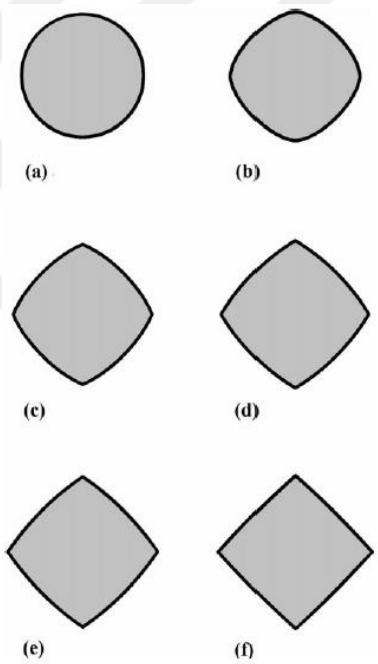

Figure 4-2. Equilibrium shapes of crystals with different degrees of four-fold anisotropy (ε_4) (a) $\varepsilon_4 = 0.00$. (b) $\varepsilon_4 = 0.05$. (c) $\varepsilon_4 = 0.10$. (d) $\varepsilon_4 = 0.15$. (e) $\varepsilon_4 = 0.20$. (f) $\varepsilon_4 = 0.50$ [86]. ε is the strength of anisotropy.

Coming back to the topic of lamellar eutectic growth, in the JH theory, the strong effect of surface energy of the solid/solid (S/S) interphase is left aside. Only in this circumstance, i.e. in the case of isotropic S/S interphases, the steady-state periodic lamellar structure is expected to grow parallel to the imposed thermal gradient upon directional solidification (DS) of thin samples. However, the S/S surface can exhibit degree of anisotropy which dramatically alters eutectic microstructure. The anisotropy of the S/S interphase boundary is not a fixed property of the material, but it varies from one grain to another. In a binary eutectic system, B. Caroli *et al.* concluded that in grains with phases having epitaxial orientation relationship, the lamellae pattern is inclined with respect to the growth direction [87]. Later, S. Akamatsu *et al.* using CBr_4-C_2Cl_6 and In-In_2Bi binary eutectic systems showed that, in anisotropic EG, the lamellae are locked onto the low-energy direction, which corresponds to the cusp singularity of the interphase energy. The examples of the locked grains in binary systems are shown in Figure 4-3. In an anisotropic grain, the shape of S/L interface stays approximately symmetric with respect to mid-plane. This assumption called as the "*symmetric pattern*" or "$\sigma \parallel Z$" approximation will be discussed in following sections. The phase-diffusion process is blocked by anisotropy of S/S boundaries in anisotropic EG with cusps singularity and the dynamics of the pattern mainly controlled by the anisotropy [88].

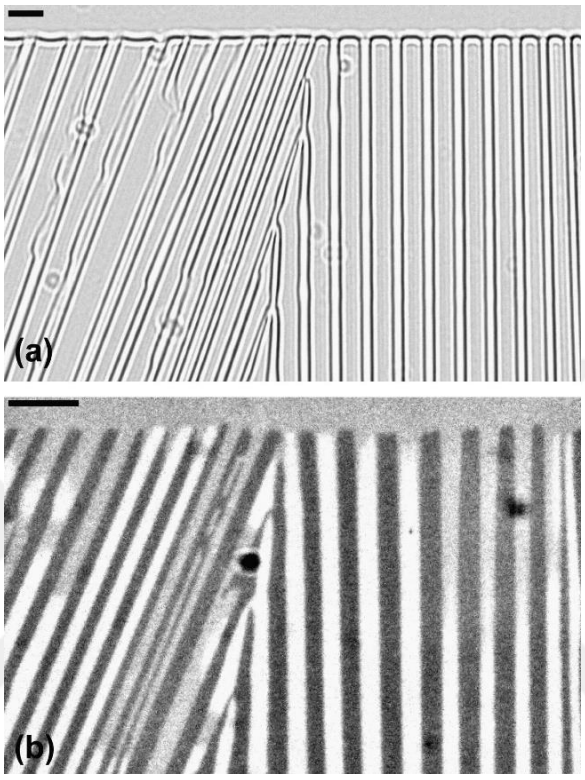

Figure 4-3. The locked lamellar structure in two-phase systems during DS experiments on left-hand side and isotropic grains in the right-hand side. (a) CBr_4–C_2Cl_6 two-phase organic eutectic system. (b) In–In_2Bi two-phase metallic eutectic system [77].

S. Ghosh *et al.* [89, 90] numerically studied the floating and locked EG growth dynamics using phase-field and dynamic boundary integral methods. By introducing the S/S surface energy anisotropy, they showed that the regular lamellar pattern evolves to inclined lamellae, confirming the experimental results obtained by RDS method.

Another type of the anisotropy-driven microstructure reported in [77] is called nearly-locked eutectic grain. In this type of eutectic grain, the S/S interphase contains nonsingular

minima in energy plot and as a result of them, the lamellar is inclined with respect to the thermal gradient. However, in contrast to fully-locked EG, in nearly-locked EG, the anisotropy does not block the spacing homogenization mechanism and therefore, the regularity of the microstructure is preserved in nearly-locked EGs.

Although the recent numerical and experimental studies revealed various aspects of the eutectic growth in three-phase systems, the effect of S/S anisotropy on three-phase eutectics growth pattern and dynamics are still not well-understood. In this chapter, the pattern formation dynamics of In-Bi-Sn three-phase eutectic system are investigated using RDS and DS techniques to examine the effect of S/S interphase anisotropy on the microstructure. The following questions are addressed: ***(i)*** What kind of microstructure forms if one or both of the existing S/S boundaries are anisotropic, *i.e.* in a locked grain? ***(ii)*** What are the dynamical characteristic features of the locked grains in three-phase systems? ***(iii)*** What are the dynamical features of pattern in the three-phase system if the interphase boundaries contain nonsingular minima? To answer these questions, systematic, reproducible and real-time DS and RDS experiments were performed using In-Bi-Sn three-phase eutectic alloy to obtain quantitative information on the pattern formation phenomena.

4.2 Experimental procedure

In this chapter, DS and RDS techniques described in *chapter 2* and *3* are employed to identify and characterize anisotropy-driven microstructures in three-phase In-Bi-Sn eutectic alloy system.

4.3 Results and discussion

In contrast to the isotropic EG, the surface energies of the interphase boundaries are orientation dependent in the locked EG. It means that in certain directions, the energy function has minima and consequently, the boundaries are locked to the low-energy direction. In the case of ABAC pattern, there are two interphases, namely AB and AC. A locked structure can be obtained as a result of anisotropy in AB or/and AC interphase boundary energy(ies). For an anisotropic interphase boundary energy, while the $\gamma_{S/S}$ is parallel to the corresponding interphase boundary, the surface tension (σ) of the interphase boundary remain perpendicular to the overall solidification front (symmetric pattern approximation). As a result, the anisotropic interphase boundary inclines θ degrees with respect to the surface tension, as schematically shown in Figure 4-4. In this case, the equilibrium at the triple-point junctions is given by Young-Herring equation:

$\gamma_{AL}+ \gamma_{BL}+ \sigma_{AB}= 0$ and/or $\gamma_{AL}+ \gamma_{CL}+ \sigma_{AC} = 0$

Where σ_{AB} and σ_{AC} are the surface tensions of AB and AC interphase boundaries, respectively. Figure 4-4 shows schematic representation of the three-phase eutectic grain with anisotropic interphase boundaries.

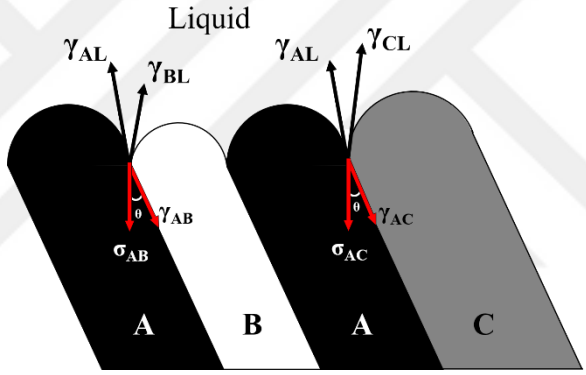

Figure 4-4. Schematic view of crystallographically locked lamellar pattern. While the interphase boundaries inclined θ degree with respect to the growth direction, the surface tensions of the interphase boundaries remain perpendicular to the front in the locked lamellar structure.

4.3.1 Fully-locked structure

Fully-locked pattern is characterized by the inclined lamellar structure with respect to the imposed thermal gradient direction, having irregular phase arrangement, and

heterogenous spacing distribution. In this type of structure, the anisotropy of the interphase boundaries is the dominant parameter and significantly alters the microstructure. An example of a locked pattern observed during standard DS experiment is given in Figure 4-5. In this example, an isotropic grain exists in the right side of the image. Coexistence of the two types of the grains at the same experimental conditions confirms the hypothesis that the formation of two grains formation is due to the internal properties of the grain and not directly related to the experimental parameters.

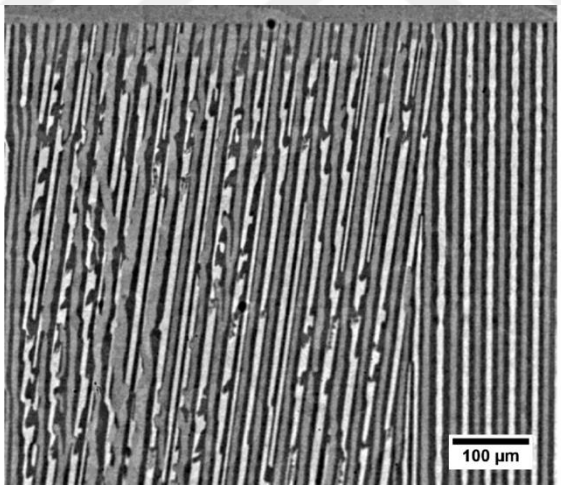

Figure 4-5. Coexistence of the locked pattern and isotropic ABAC patterns observed during standard DS experiment. V = 0.250 µm/s, G = 5.1 K/mm, and δ = 13 µm.

Although within the locked EG, small regions may preserve the ABAC stacking sequence, the overall phase arrangement is deviated from the ideal ABAC basic state.

Therefore, eutectic spacing, *i.e.* the width of the ABAC pattern, cannot be measured from the whole microstructure. Instead, one can measure the spacing between successive In_2Bi phases, irrespective of the neighboring phase identity, as suggested in the reference [68]. The spacing values measured in this way from a locked structure grown at V = 0.150 μm/s are tabulated in Table 4-1 and compared with the λ/2 value of the isotropic ABAC pattern grown at the constant velocity [70]. $\lambda/2_{min}$, $\lambda/2_{max}$, the difference between min and max ($\lambda/2_{min}$ - $\lambda/2_{max}$), $\lambda/2_{mean}$ and the standard deviation (STD) of the mean values are measured from the same pattern at five different growth lengths. For all the measurements taken at different locations during the growth of the locked pattern for more than 1000 μm growth length, the difference between the min and max λ/2 values was at least 20 μm. Compared to the value obtained for quasi-isotopic grains, *i.e.* 3.9 μm, this value is dramatically large, indicating that there is a non-homogenous spacing distribution in the locked EG. To investigate whether the spacing homogenization process [48, 49, 91] is active within the grain, five spacing measurements were performed from different locations. The selected area was followed within a fixed frame which included identical phases. The measured spacing value shown in Table 4-1 did not show any homogenization over time in the defined spacing, which shows that phase diffusion is not taking place in locked grains. This finding is consistent with what was observed in two-phase locked eutectic grains [77]. Comparing λ/2 values with the minimum undercooling spacing of an isotropic ABAC pattern [70] at the same growth velocity reveals that the spacing modulation in the locked structure dramatically large and essentially time-independent.

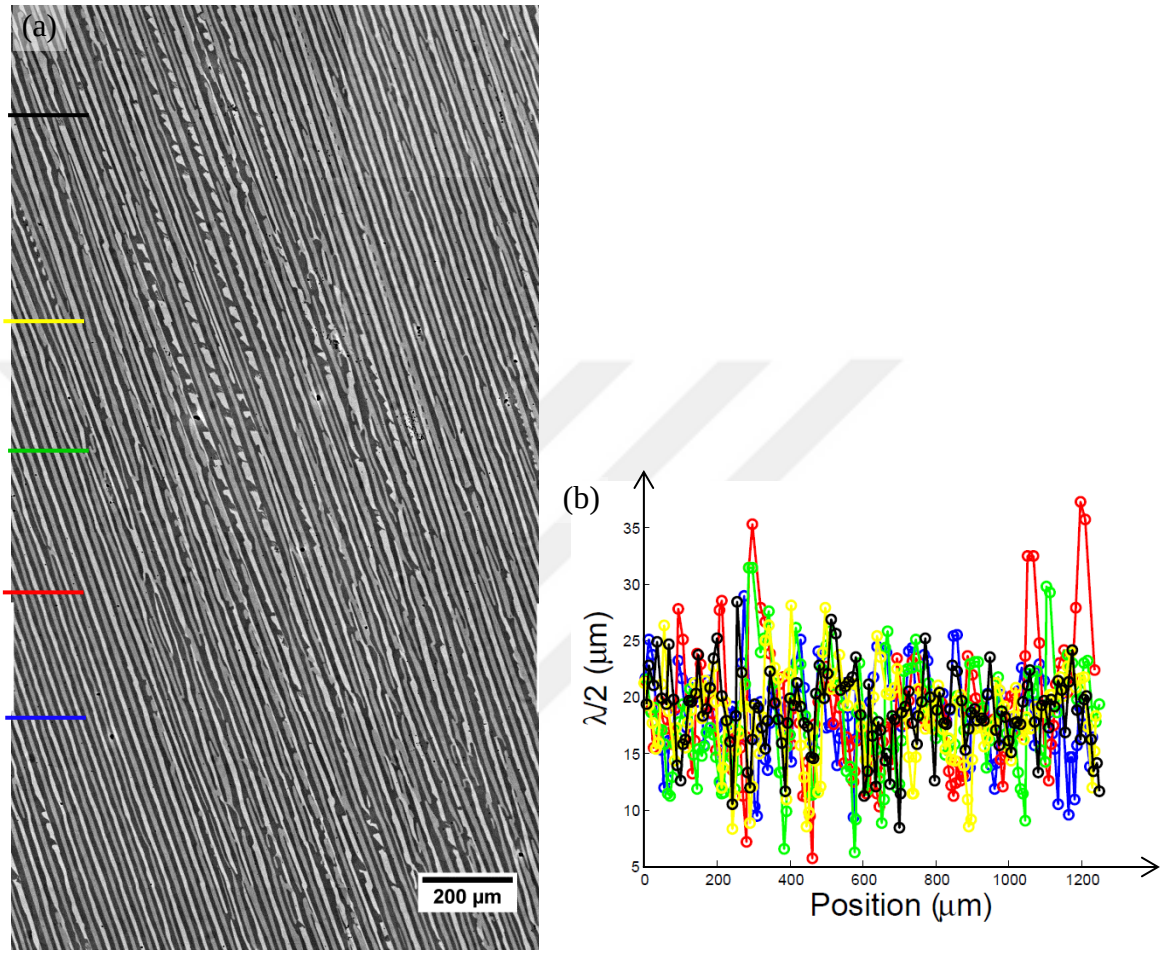

Figure 4-6. An example of the locked lamellar structure. (a) Marked lines are the position where the spacing values are measured. (b) The eutectic spacing plot measured from the microstructure given in (a). The spacing has non-homogenous distribution in locked structure. V = 0.150 µm/s, G = 3.3 K/mm, and δ = 23 µm.

Table 4-1. Five spacing values measured within a locked structure compared to the minimum undercooling spacing in the isotropic ABAC. No 1 measurement was taken as a reference point of growth length wherein the pattern is already grown more than 1000 μm.

No	$\left(\frac{\lambda}{2}\right)_{min}$ (μm)	$\left(\frac{\lambda}{2}\right)_{max}$ (μm)	$\left(\frac{\lambda}{2}\right)_{max} - \left(\frac{\lambda}{2}\right)_{min}$ (μm)	$\left(\frac{\lambda}{2}\right)_{mean}$ (μm)	STD of $\left(\frac{\lambda}{2}\right)_{mean}$ (μm)	Growth length (μm)
1	9.3	30.0	20.7	18.4	3.7	reference point
2	5.7	37.3	31.6	17.5	5.5	325±10
3	6.3	31.5	25.2	17.5	4.9	605±10
4	8.2	28.2	20	18.4	4.0	900±10
5	8.4	28.4	20	18.7	3.5	1350±10
Isotropic [70]	12.9	16.8	3.9	-	-	-

Close snapshot of the solidification front of a locked structure is shown in Figure 4-7. Similar to all locked grains observed during this study, both AB and AC interphase boundaries are inclined at the same angle with respect to the growth direction. This situation can be due to two possibilities: either both boundaries have the cusp singularities at the identical orientation or only the surface energy of one boundary have minima and the other one is forced to incline at the same orientation with the locked boundary. The first case has a very low probability to occur since each phase has unique lattice parameters. To investigate which boundary is responsible for locking, RDS experiments are performed and the S/S interphases of AB and AC boundaries are examined. For this particular case, however, it can be seen that the S/L interphase of C is asymmetric while A and B are symmetric. That means

AB interphase is the anisotropic interphase boundary and the reason of the locking while AC is tilted due to dynamical reasons.

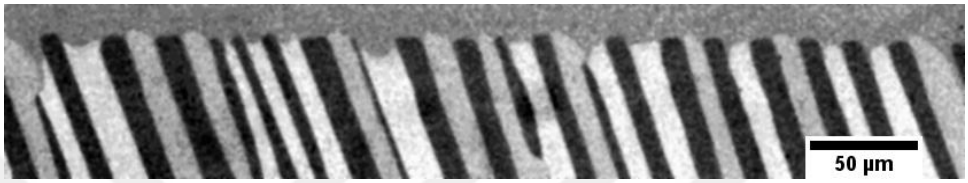

Figure 4-7. Close snapshot of the solidification front of a locked eutectic grain in three-phase system during DS experiment. Both boundaries were inclined 22º with respect to the thermal gradient direction. V = 0.080 µm/s, G = 3.3 K/mm, and δ = 23 µm.

During a full rotation of a locked EG, at some well-defined orientations, the interphase boundaries become highly inclined with respect to the thermal gradient direction. At this case, the structure cannot grow any further, and has to either lock into another orientation or unlock. This behavior is determined purely by the Wulff plot of the corresponding interphase boundary. In Figure 4-8 the full rotation of a locked EG during an RDS experiment is shown. In this case, when the inclination angle is high, the grain goes through a transient regime, after which it unlocks. Transient states which link each locking and unlocking states in Figure 4-8, have a noticeable sawtooth structure along the AB boundary and it is sometimes accompanied by branching events. The locking/transient/unlocking/transient sequences are followed during the rotation of the sample. In this figure, the pattern travel direction is centripetal spiral, where all the phases end up in the center of the spiral marked with “O”.

Locking occurs at the same inclination angle at the angular ranges marked with L_1 on Figure 4-8, which are 180º symmetric with respect to the center of the spiral. In other words, structures observed at L_1 angular ranges belong to the axisymmetric cusps of the corresponding Wulff plot. The transient states marked by T_{type1}/T_{type2} and isotropic part marked by I_1 also have 180° symmetry with respect to the center of the spiral. Therefore, the representing Wulff form of the interphase boundary contains two minima with 180º symmetry whereas it is circular in the unlocked orientations. This means, while the EG is floating during the circular portion of the Wulff plot, at the minima, it locks to the orientation of the cusps.

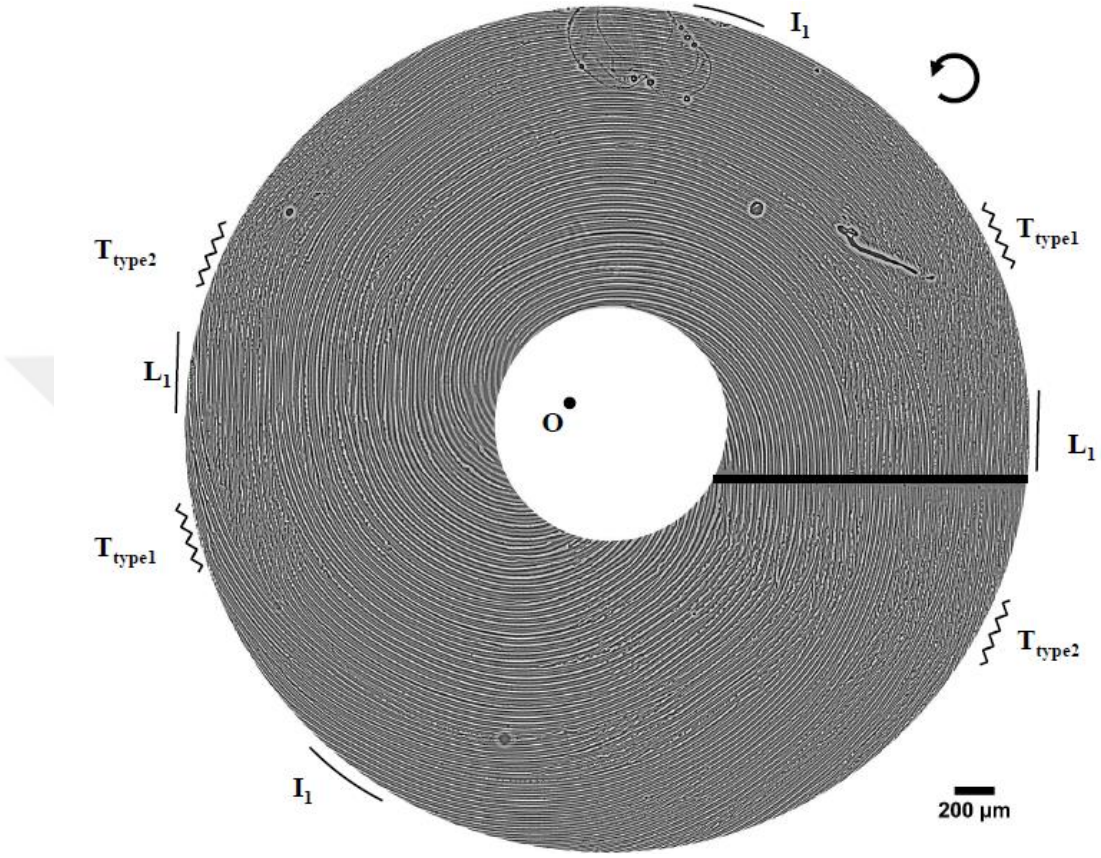

Figure 4-8. The RDS pattern showing evolution of the ABAC pattern to the locked pattern in two angular ranges with 180º symmetry with respect to the center of spiral. CCW, ω = 0.010 º/s, G = 5.1 K/mm, and δ = 13 µm.

The evolution of the pattern in Figure 4-8 is summarized in Table 4-2 where the microstructures obtained at different rotation angles are given along with the definition of each state and structure. The locked structure inclined at an angle of 6.6° with respect to the growth direction is followed by the transient state type 1. After this transient state, the microstructure unlocks which results in a gradual reduction of facets in the AB boundary and

eventually recovery of the regular ABAC pattern. The unlocked state corresponds to the circular portion of the Wulff plot. It should be mentioned that, in the unlocked state, some defects in stacking sequence might remain depending on the growth length in this state. As the rotation angle gets closer to 180º, the regular ABAC pattern evolves to the type 2 sawtooth structure. By 180º rotation of the sample, the pattern locks with the same angle as in the first locking occasion, indicating the existence of another cusp singularity at this angular range. The subsequent evolution of the pattern includes transient type 1/unlocking/transient type 2/locking sequence; all of which have 180º symmetry with respect to the previous occasion of the same type. Since the spiral is centripetal, the microstructure after 180° rotation is coarser than the first set due to being closer to the center.

Table 4-2. Microstructure evolution during the RDS experiment shown in Figure 4-8. Upon 180 º rotation, the same structure is obtained as shown below.

State	Structure	Rotation angle (º)	Microstructure	Rotation angle (º)	Microstructure
Locked	Inclined lamellae	0±2	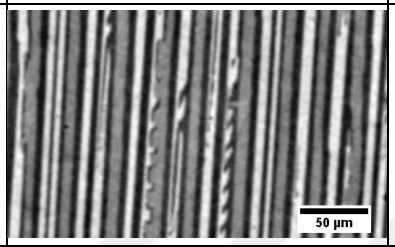	180±2	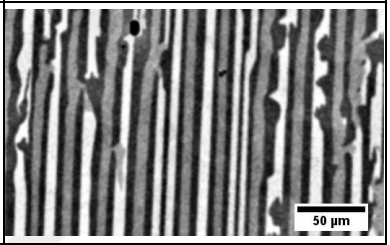
Transient Type 1	Sawtooth	24±2	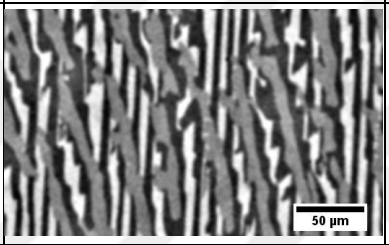	204±2	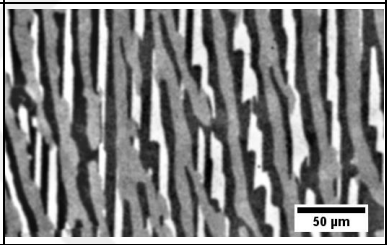
Unlocked	Regular ABAC	74±2	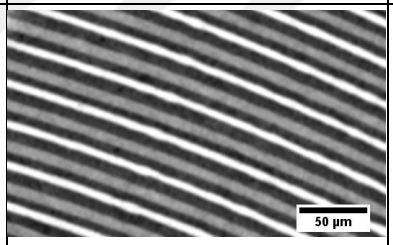	254±2	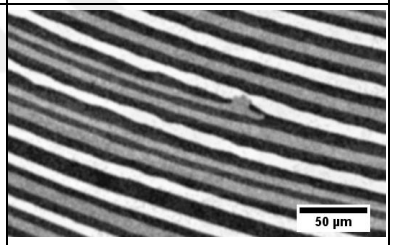
Transient Type 2	Sawtooth	153±2	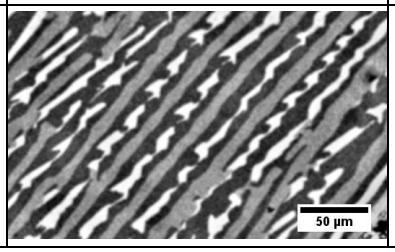	333±2	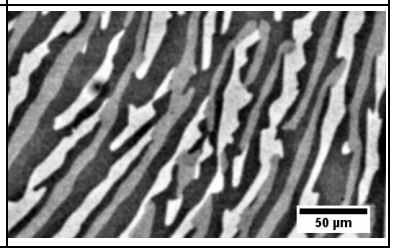

Each state of this microstructure evolution requires careful examination. In the locked state, illustrated in Figure 4-9, the pattern inclines with respect to the thermal gradient direction indicating that there exists a cusp singularity in the γ-plot. In this state, similar to the locked EG in DS shown in Figure 4-5 and Figure 4-6, the regularity of the ABAC pattern

is disturbed and both AB and AC boundaries incline at the same angle. Additionally, Figure 4-9 reveals that the pattern preserves the lamellar structure as the phase ordering at the top and bottom views of the microstructures are the same. The minor differences between the top and bottom structures is due to change of wetting properties of the β-In (white) phase when EG is locked. This phenomenon is commonly observed in locked EG of two-phase [77] and three-phase growth in In-Bi and In-Bi-Sn eutectic systems, respectively. Since white phase wets the glass much less in the locked EG, a liquid meniscus is left between the solid and the glass plate. Because this liquid is supercooled, when there is a chance, In_2Bi (black) phase grows rapidly within this meniscus. Therefore, in these images, AB interphase at the glass/solid surface is not always straight and the S/L interface of the white phase is commonly looks gray.

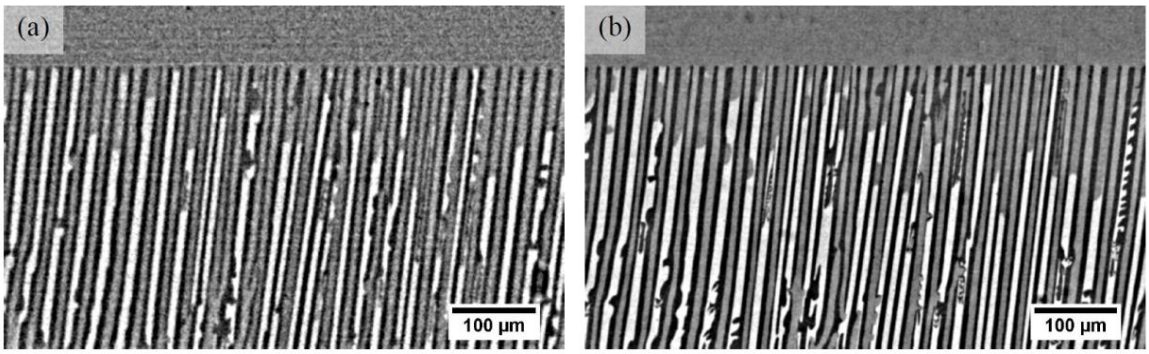

Figure 4-9. The locked structure observed during the RDS experiment. (a) Top microstructure. (b) Bottom microstructure. CCW, $\omega = 0.010^{o}/s$, G = 5.1 K/mm, and δ = 13 µm.

After the locking state, the transient state is appeared where facets formed along the AB boundaries as shown in Figure 4-10. This microstructure essentially has the same characteristics of the sawtooth lamellar trajectories reported in [77]. The orientations of the facets in the transient state belong to the forbidden orientations of the AB boundary in the corresponding Wulff plot. These forbidden orientations are present when the equilibrium crystal shape has sharp edges due to cusp singularities in the Wulff plot, and therefore, the Wulff planes will not be part of inner envelope [92]. Mathematically speaking, the condition for the existence of the forbidden orientations occurs when the surface stiffness, $\tau = \gamma' + \gamma''$, is negative value. As a result, the interface is not stable against a hill-and-valley instability [75] described by Herring [93]. The observed transient state can be described by a hill and valley structure proposed by Herring analysis [93] in which the break-up or faceting of an initially flat surface occurs if only its orientation is not present on the Wulff equilibrium shape. According to Herring, such event will lead to a reduction in total surface free energy of a system. From this analysis, it can be concluded that the driving force for the formation of sawtooth structure observed in this study is the minimization of the overall interphase surface energy, although the total surface area is increased.

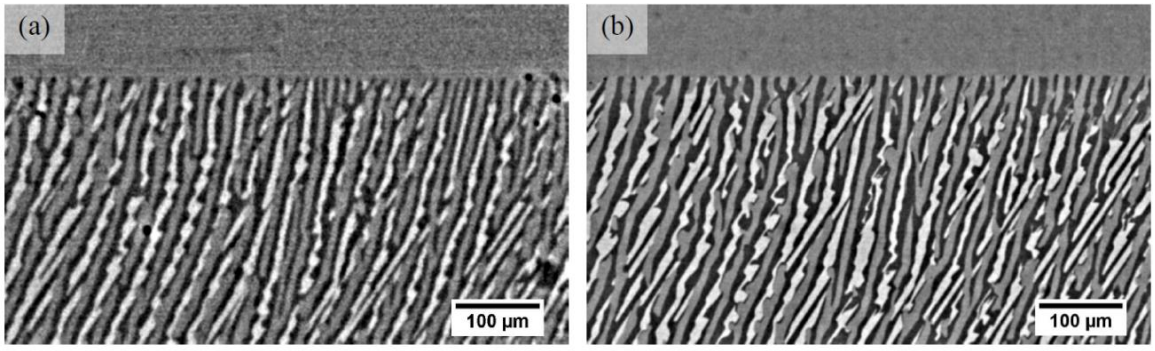

Figure 4-10. The transient state which separates locking and unlocking state during the evolution of a locked grain in the RDS experiment. (a) Top view. (b) Bottom view. CCW, $\omega = 0.010^{o}/s$, G = 5.1 K/mm, and δ=13 µm.

It should be noticed that in the transient state, the AC boundaries floatingly follow the patch of AB boundaries. The formation of facets is only observed in AB boundaries, which leads to a conclusion that in this example of the anisotropic EG, the AB interphases is the responsible boundary for the formation of the crystallographically locked EG. The AC boundaries in this grain, on the other hand, easily follow the locking and transient behavior of the AB boundaries due to having orientation-independent interphase energy.

4.3.2 Directional growth of the transient state

To characterize the microstructure formed in the transient state, the following experiment was performed. The locked grain formed in the previous experiment is melted

and rotated to grow the transient microstructure as extended as possible. Figure 4-11 shows the microstructure in the transient state formed during RDS. Then the rotational movement is stopped and therefore, the grain is kept in the transient state. Subsequently, the directional movement is started to observe the growth dynamics of the transient state in unidirectional movement.

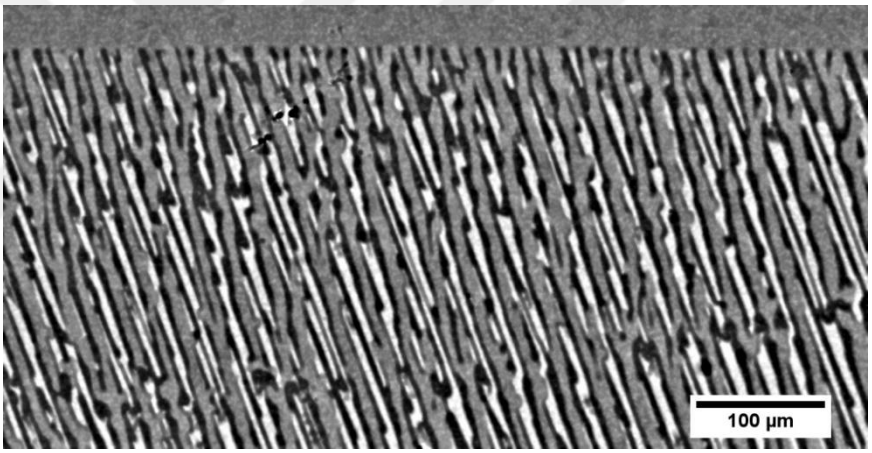

Figure 4-11. The transient state formed during the RDS experiment. CCW, ω = 0.013 °/s, G = 5.1 K/mm, and δ = 13 µm.

Figure 4-12 shows the directional growth of the pattern kept in transient state after 735 µm growth length. It can be seen from the Figure 4-12 that the facets on AB interphase boundary are present during directional growth as well. The AC interphase boundary, however, has floating growth dynamics and it is almost parallel to the direction of the thermal

gradient. It should be noted that the facets on the AB boundary affect the AC boundary and it cannot have a straight lamellar structure as it is the case in isotropic pattern. Consistency of features of the both interphase boundaries during DS and RDS experiments confirms the conclusion that in this type of the locked grain in three-phase system, the anisotropy of one of the interphase boundary, AB, governs the dynamics of locked structure. On the other hand, the AC interphase boundary contains negligible anisotropy, and does not affect the overall microstructure.

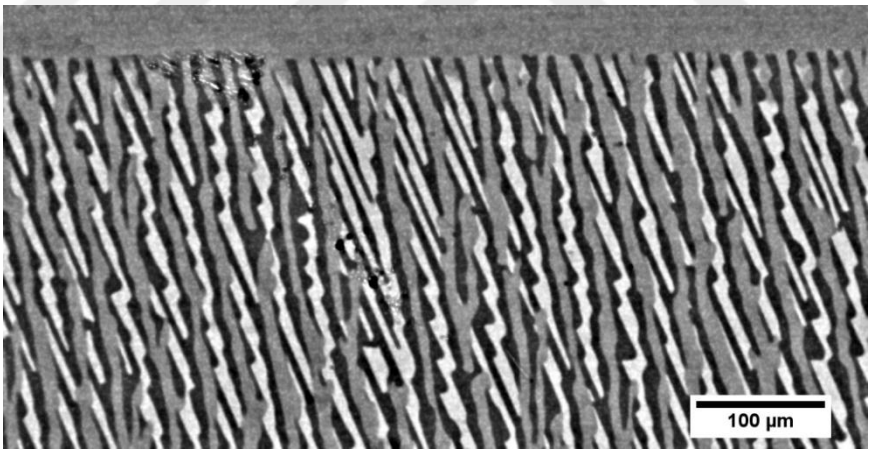

Figure 4-12. Directional growth of the transient state formed previously by the RDS experiment. V = 0.250 µm/s, G = 5.1 K/mm, and δ =13 µm.

4.3.3 Nearly-locked structure in the three-phase system

Nearly-locked eutectic grains are also observed in the three-phase system during RDS experiments. In this type of structures, the interphase has nonsingular minima in the S/S boundaries, observed in two-phase eutectics [77]. Since in this type of pattern the distinguishable dynamics of the fully-locked structures such as formation of facets, features related to the forbidden orientations and irregular phase arrangements are absent, the problem in three-phase eutectics arises that the interphase boundary that has these nonsingular minima is unknown. To overcome this problem, it is tried to set the experimental parameters such that an independent interphase boundary can be generated within a single three-phase grain. This means that while in one eutectic grain of the three-phase system, two boundaries are always present, namely AB and AC boundaries, it might be possible by setting experimental parameters such that in small region only two phases exist. Thus, only one boundary, AB or AC boundary, will be present. Let's first consider the evolution of the nearly-locked pattern during an RDS experiment. Figure 4-13 shows the microstructures during an RDS experiment in the state that the lamellar structure is considerably inclined with respect to the overall growth direction. The following evidences can be immediately driven from Figure 4-13. First, despite relatively steep inclinations of the lamellae, the overall phase arrangement is ABAC, although there are some faults in the pattern. Second, an ABACAC stacking fault in the middle of pattern, which is later removed by elimination of C and merging of two A phases. Third, one can realize the lamellar shape of the phases are preserved as the top and

bottom microstructures are identical. Finally, the phase arrangement in the inclined structure of this type of grains is more regular than the inclined microstructure of a fully-locked grain. It is means that the anisotropy does not block the spacing adjustment and homogenization mechanisms in this state.

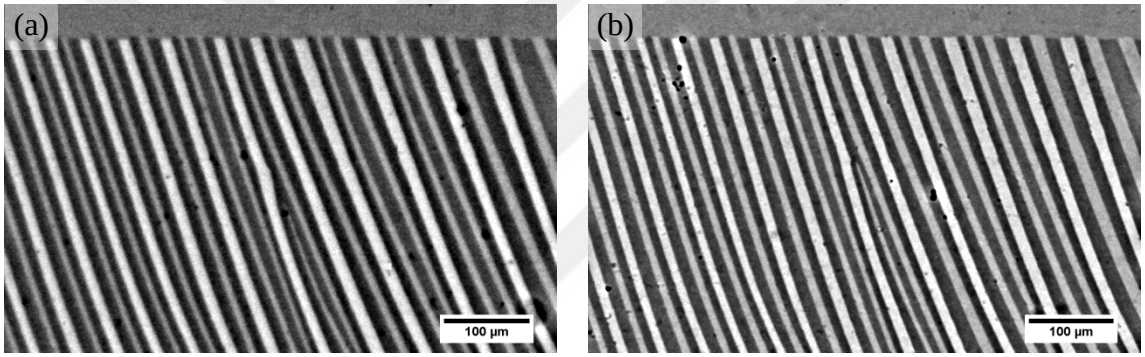

Figure 4-13. The inclined lamellar microstructure in nearly-locked EG during an RDS experiment. (a) Top microstructure. (b) Bottom microstructure. CCW, $\omega = 0.006$ °/s, G = 5.1 K/mm, and $\delta = 13$ µm.

As sample is rotated further, the next step before unlocking state is accompanied by the formation of the dense and continuous branching events of the phases. Figure 4-14 shows the microstructures corresponding to this state from top and bottom views. Even though the regularity of the microstructure is dramatically disturbed in this step, it is a smooth transition mode and there is no of forbidden orientations between nearly-locked and unlocked states. As it was shown earlier in this chapter, in fully-locked structures, the transition from fully-

locked to unlocked states is accompanied by a state which belonged to the forbidden orientations of AB interphase boundary.

The dense branching morphology formed in Figure 4-14 may be comparable with seaweed structure, which forms as a result of weak anisotropy of the S/L interface energy. The main characteristic of the seaweed is continuous splitting of the tip without an orientational order [53]. In the case of structure formed in Figure 4-14, the anisotropy, of yet-unknown interphase boundary, forced the lamellar structure to incline with respect to overall growth direction. However, when the interphase energy reaches to the isotropic portion of the corresponding Wulff plot by further rotation of the sample, the lamellae are weakly affected by the anisotropy. Hence, there has to be a mechanism using which the inclined interphases turn back to grow parallel to the imposed thermal gradient direction. Producing the new branched arms which are growing parallel to the gradient direction, most probably, is an efficient mechanism to unlock. The branching events occur at all types of phases to guarantee all boundaries to be able to grow floatingly in the isotropic portion of the corresponding Wulff plot. It is worth noting that the branching events in this state are different than what previously discussed as the upper limit of stability regime. While the former occurs during transition from nearly-locked to unlocked structure due to S/S anisotropy and it is independent of experimental conditions, the latter is the spacing adjustment mechanism that occurs in the absence of S/S anisotropy and, generally speaking, it is the response of the system to growth velocity change.

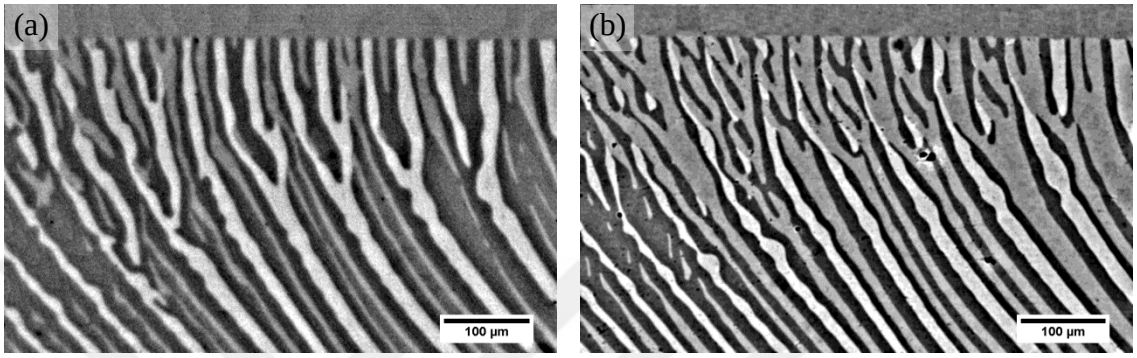

Figure 4-14. The microstructure showing the transient state between nearly-locked and unlocked states during an RDS experiment. (a) Top microstructure. (b) Bottom microstructure. CCW, $\omega = 0.006$ º/s, G = 5.1 K/mm, and $\delta = 13$ µm.

The unlocked state after the transient state includes very rapid recovery of the ABAC pattern. Many faults in the stacking sequence are quickly removed and ABAC pattern is regained. Formation of the ABAC pattern indicates that now the interphase boundary energy operates in the isotropic portion of the corresponding Wulff plot. Figure 4-15 shows the ABAC microstructure formation right after the transient state in nearly-locked EG.

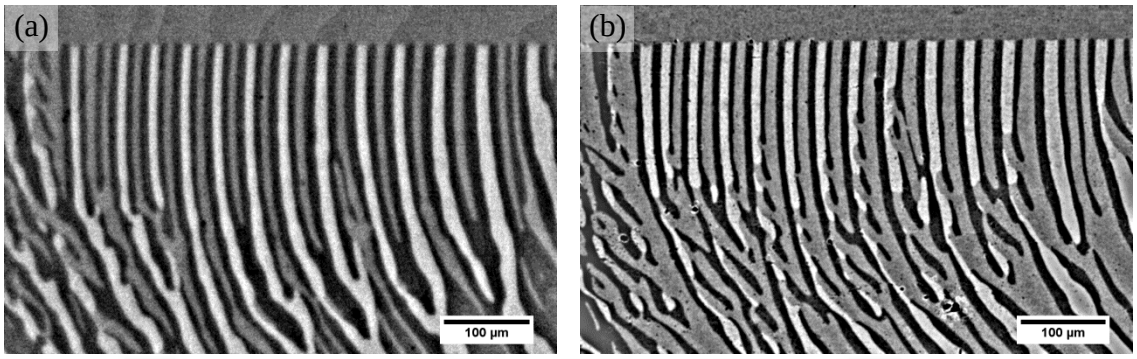

Figure 4-15. The microstructure showing the formation of ABAC structure after the transient state during an RDS experiment in nearly-locked EG. (a) Top microstructure. (b) Bottom microstructure. CCW, $\omega = 0.006$ º/s, G = 5.1 K/mm, and $\delta = 13$ µm.

Figure 4-16 shows the full turn evolution of nearly-locked eutectic pattern during an RDS experiment. The evolution sequence contains nearly locking, smooth transient and unlocking states. Nearly locking occurs in a large angular range with two-fold symmetry. The inclination angles of lamellar within a nearly locking angular are found to be different. This can be due to the nonsingularity of the minima values which allows to select different inclination angles, probably based on the induced growth velocity within different lamellae. However, locally following one interphase boundary, the inclination angles are the same after 180º rotation. Each-nearly locked state is linked to unlocking via a transient state which its area is defined by the induced growth velocity. It means that it is small region close to the center where the induced velocity is low, and it is large region when it is far from center wherein the induced velocity is relatively high. Additionally, by increasing induced growth

velocity from the central region towards the outer side, the number of branchings is dramatically increased. High velocity in fact provides more occasions.

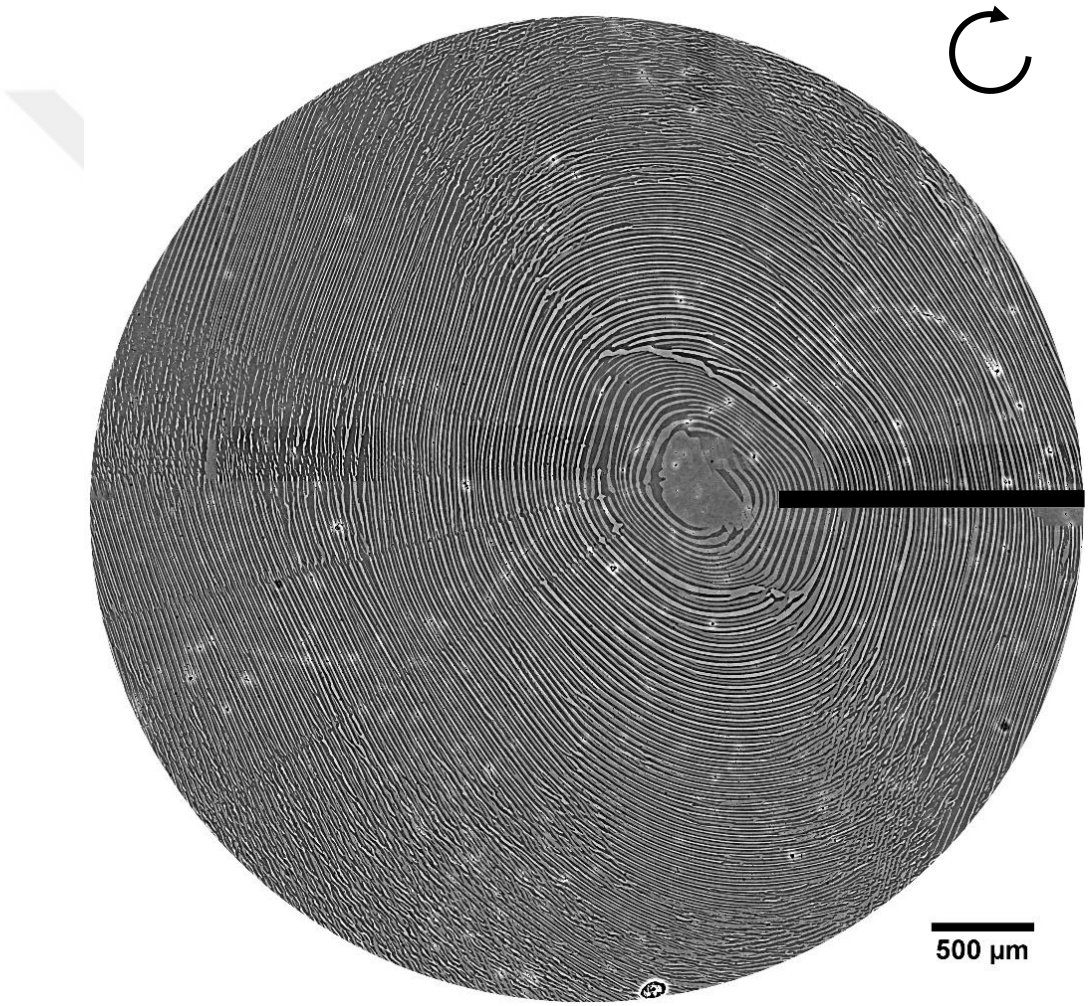

Figure 4-16. Full turn evolution of the nearly-locked structure formed during an RDS experiment. CCW, $\omega = 0.006$ °/s, G = 5.1 K/mm, and $\delta = 13$ µm. Black spots on the image are dirt on the glass plate.

In this experiment, the rotation speed is set to be very slow, $\omega = 0.006$ º/s, to avoid irregularities during transient state. At the same time, the slow rotation speed provides a region close the center, where only A and C are growing. This region enables investigation of AC boundary properties independently within the three-phase grain. Figure 4-17 shows the central part of the pattern which contains the alternation of mostly the two-phases, *i.e.* In_2Bi and γ-Sn.

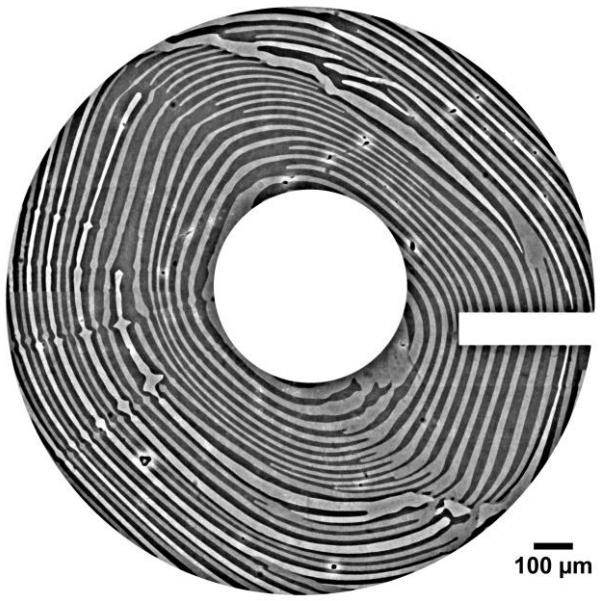

Figure 4-17. Central region of the pattern shown in Figure 4-16. The region contains only In_2Bi and γ-Sn phases. The lamellar trajectories are rectangular shape with smooth corner. $\omega = 0.006$ º/s, G = 5.1 K/mm, and $\delta = 13$ µm.

Even though this region is small, it provides valuable information about one of the boundary within the three-phase eutectic grain. The lamellae trajectories in Figure 4-17 ensure that the AC boundary contains the nonsingular minima in its Wulff plot. The anisotropy is two-fold type as the microstructure has two wide angular ranges with 180º symmetry and two short angular ranges with 180º symmetry, where the lamellae trajectories are growing at angle with respect to the imposed thermal gradient direction. Figure 4-18 (a) illustrates the trace of one AC boundary from Figure 4-17, clearly showing the angular ranges of nearly-locking and unlocking states of the boundary. Figure 4-18 (b) shows FFT (Fast Fourier Transformation) of the interphase boundaries trace of Figure 4-17, representing four angular ranges, where the nearly-locking is occurring. The AC boundary trace in Figure 4-18 (b) could be fitted using sum of sine function, r (θ) = $\sum_{i=1}^{5} a_i \sin(b_i + c_i\theta)$, with a_i, b_i, and c_i constant values shown in Figure 4-18 (c).

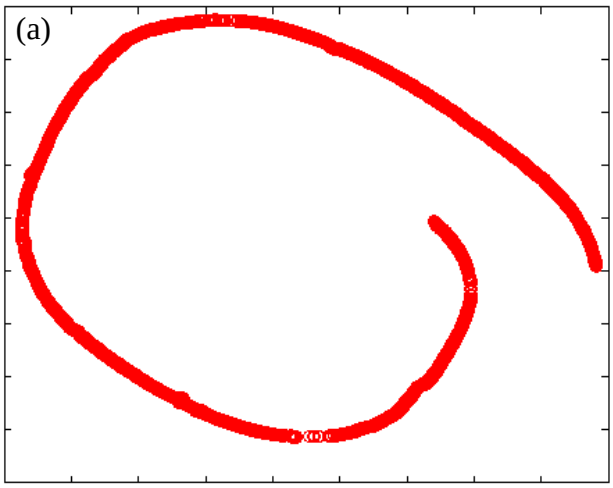

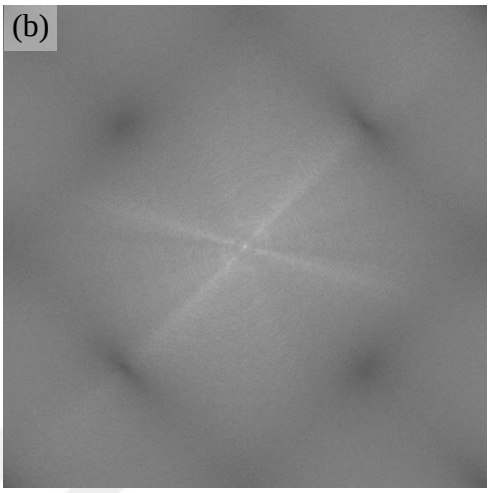

(c)

$r(\theta) = \sum_{i=1}^{5} a_i \sin(b_i + c_i \theta)$

rms = 3.6 μm

No.	a_i	b_i	c_i
1	1839.0	0.0064	0.55
2	1516.0	0.0073	3.60
3	48.6	0.0365	-1.15
4	15.8	0.0469	0.79
5	12.4	0.0705	0.79

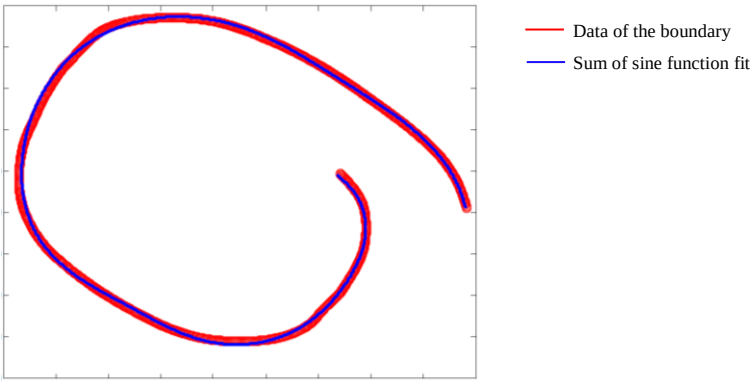

Figure 4-18. (a) The trace of one AC boundary from Figure 4-17 upon full rotation of the pattern in RDS experiment. (b) FFT image of the interphase boundary trace in Figure 4-17 showing four angular ranges of nearly-locked states. (c) Blue curve is the sum of sinuses function fit given in the table.

Nearly-locking state differs from the fully-locked lamellar structure shown in Figure 4-8, where there exist singular minima and forbidden orientations. Unlike the fully-locked lamellar structure, in nearly-locked structure, no facets formed at the interphase boundary and the transition between the states is a smooth transient. The differences in the nearly-locked structure between two-phase and three-phase systems is the dynamics of the transition between nearly-locked and unlocked states. While in two-phase system, the transition occurred in a very smooth way without any perturbation in the pattern at all, in the three-phase system within the transition state the pattern is disturbed by many branchings of all phases. This difference does not seem to be due to experimental conditions. The branching events in three-phase system should be unlikely related to the rotation speed as it is slower in the current study (0.006º/s) than what was reported in two-phase system (0.014º/s). This variation can have origins such as dissimilar anisotropy or interconnected effects of two interphase boundaries on each other in three-phase systems.

4.4 Conclusion

In the presence of S/S anisotropy, two distinct eutectic grains, namely fully-locked and nearly-locked are identified in there-phase system and their growth dynamics are discussed in detail. In contrast to isotropic EG explained in *chapter 2* and *3*, in the locked grains, the movement of the triple-point junctions deviate from the thermal gradient direction. The

preferred growth direction of the locked grain is the low-energy direction of the surface energy of interphase boundaries.

In the Wulff plot of the fully-locked structure, there exist singular minima in certain orientations. The lamellar structure is inclined with respect to the overall growth directions when the S/S interphase is within an angular range where the minima are effective. In the locking angular range, the regularity of ABAC pattern is intensively disturbed. The eutectic spacing in this state is essentially non-homogenous and time-independent and growth dynamics are no longer controlled by phase-diffusion, spacing adjustment and recovery mechanisms. During RDS experiments, it was observed that the locked state evolves to unlocked state in some angular ranges, where the isotropic ABAC pattern is formed. Each locking and unlocking state is linked by a transient state, which comprised of sawtooth lamellar trajectories. It is proposed that, only one of the boundaries of ABAC pattern namely AB, contains the minima with deep cusps. This is in agreement with observing sawtooth structure only in AB boundaries. On other hand, the AC boundaries, mandatorily follows the locked boundary. The transient state corresponds to the forbidden orientation of the surface energy of AB boundary. The facet formation in the AB boundary is analogous to the Herring's description of the break-up surface due to the forbidden orientations in the Wulff plot. In the studied locked type, eutectic grain there are two singular minima in 2D section of the Wulff plot with 180° symmetry. The properties of the fully-locked structure are consistent in RDS and DS experiments, indicating the features are the intrinsic property of

the eutectic grain. The dynamics of the locked lamellar structure in three-phase system are found to be very similar to the locked lamellar pattern in two-phase systems.

A eutectic grain with nearly-locked structure was identified in the three-phase system. The evolution steps of the grain during RDS experiment composed of the nearly-locking/ transient/unlocking/transient states. The lamellar structure is also inclined with respect to the overall growth direction within one relatively wide and one short angular ranges during nearly-locked states. However, during this state, the ABAC pattern does not lose its regularity as it was the case of fully-locked structure. Additionally, no facets formed in neither interphase boundaries. By continuous rotation of the sample, the unlocked state approaches in which pattern is recovered to floating type. These two states are linked by a transient state which is accompanied by the formation of dense branchings. The formation of these branchings is unlikely related the eutectic spacing adjustment. However, comparing to the transient state observed in the fully-locked structure, one can conclude that they are not due to any forbidden orientations and there is a smooth transition between the two states. The dynamics of independent AC boundary in the absence of AB boundary in the studied grain reveals that the AC boundary itself has the nearly-locked crystallographic dynamics. The trace of the boundary in the RDS experiment showed that this boundary has two nonsingular two-fold minima in 2D Wulff plot. As a result of it, the whole three-phase eutectic grain has the similar dynamical features. It is suggested that in this case, the main

responsible boundary for the nearly-locked behavior is the AC boundary and the other boundary, *i.e.* AB boundary, does not contain significant anisotropy in the interphase energy.

Chapter 5 : Three-phase eutectic growth in the presence of S/S anisotropy in quasi-2D samples, Part B

5.1 Introduction

The dynamics of the microstructural transformations are highly impacted by the intrinsic features of surface energies of the phases involved in the system. D. Hoffman and J. Cahn in the landmark article published in 1998 proposed a vector function $\zeta(\hat{n})$ for the free energy of an arbitrary anisotropic surface. They discussed that this vector has two components. The first component is the unit normal ($\hat{n}$) and tends to shrink the surface to minimize the free energy. The second component is off-normal and tends to rotate the surface in order to minimize free energy. The off-normal component of the defined vector is zero for an isotropic surface and therefore the surface does not have any driving force to rotate. In this case, the minimization of the energy occurs only by contracting the surface area. However, anisotropic surface has the off-normal component and thus torque arises to rotate the surface to minimize the free energy [94]. Therefore, one can expect changes in terms of shape and orientation in the physical surfaces when the surface is anisotropic.

Upon solidification, growth pattern is significantly affected by the surface tension anisotropy. In the absence of anisotropy of the S/L surface tension and at growth velocity satisfying constitutional law [95] the planar growth front is obtained. On the other hand, the microstructures such as dendrites and degenerated seaweeds arise from the anisotropy of surface tension between solid and liquid [96, 97]. Depending on the strength of the anisotropy, dendritic growth is expected in the presence of strong anisotropy and seaweeds

in the presence of low anisotropy cases [96, 98]. Figure 5-1 shows the examples of dendritic and seaweed structure formed during directional solidification of 0.25% SCN-PEO system.

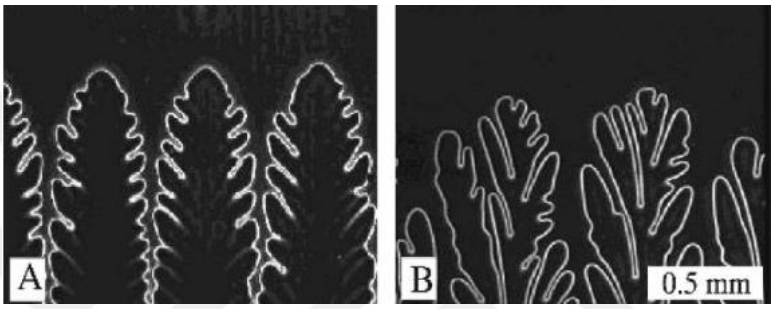

Figure 5-1. The experimental observation of (a) Dendrites. (b) Seaweed in 0.25% SCN-PEO system at the same experimental conditions [98].

When it comes to the anisotropy of the surface tension in S/S interface, it was discussed in *chapter 4* that in two-phase eutectics, the lamellar structure has the tendency to lock into the low-energy direction in order to decrease the overall interfacial energy. It was shown that similar dynamics takes place in the case of three-phase In-Bi-Sn system. However, due to the presence of two interphase boundaries in the system, the phenomena are more complicated. For the case of anisotropic eutectic grains, a new microstructure will be introduced in this chapter, to our best knowledge, has not been reported in the literature. The microstructure is called "separated structure" in which two phases of the system, *i.e.* A and B, are coupled and the third phase, C phase, is rejected from the coupled two-phase region.

This gives rise to formation of a 3D microstructure in the quasi-2D samples. The phase morphology, thus, changed from regular lamellar to a complicated morphology. It was discussed in *chapter 1*, the volume fraction of the phases affects the eutectic microstructure such that for equal phase fraction of the phases, the lamellar structure is the selected morphology to provide less surface area. In the case of small volume fraction of one phase, the rod morphology is favored due to having less surface area. This hypothesis was preserved in the anisotropy-driven microstructures discussed so far. In other words, although the anisotropy governs the dynamics of the lamellar growth, it does not significantly alter morphology of the phases. In this chapter, it will be shown that the anisotropy of the S/S interphase boundary directly alters the phase morphologies for the same volume fraction and experimental conditions.

5.2 Experimental procedure

The DS and RDS experimental methods explained in *chapter 2* and *3* were utilized to obtain the result explained in this chapter.

5.3 Results and discussion

5.3.1 Onset "Separated structure" formation

At the start of experiment, the sample is kept within the thermal gradient at zero velocity which results in formation of γ-Sn (C) as a multi-crystalline layer, as discussed in *chapter 2*. By the start of directional movement, In_2Bi (A) phase is growing from underlining crystals. Subsequently, two phases grow in a coupled manner for a certain amount of time. The two-phase growth length in a ternary system perhaps depends on the actual composition of the alloy and the experimental parameters. Since both of the phases are grown from the existing solid, crystallographic orientation as well as the interphase energy features are set by the initial solid seed crystals. Figure 5-2 shows the initial stage of the two-phase growth, where γ-Sn (C) and In_2Bi (A) phases are growing in a coupled way. In this example, first the structure was fast grown from the position in channel then the velocity is set to zero. Figure 5-2 shows a layer of γ-Sn (C) crystals is formed at V = 0. After growing of In_2Bi (A) phase with the start of the directional movement, two phases grow for relatively long length ~1750 μm. The growth dynamics of the two-phase structure, *i.e.* γ-Sn and In_2Bi can reveal the property of the AC interphase boundary in the early stage of the experiment. These crystals grow almost parallel to the thermal gradient direction (inclined ~3-4º).

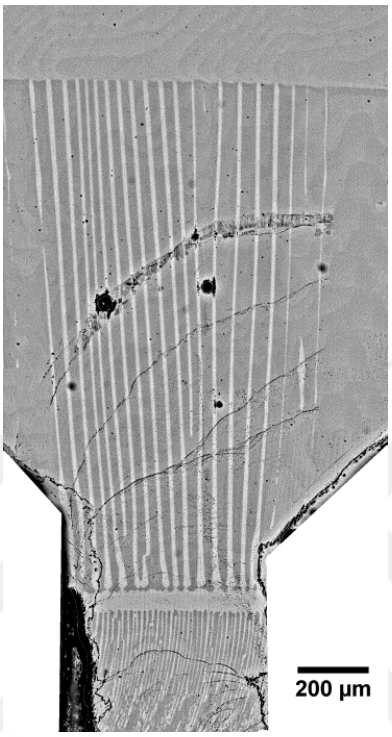

Figure 5-2. The initial stage of three-phase eutectic grain growth is accompanied by two-phase growth. At V= 0, the layer of γ-Sn is formed. By the onset of the directional movement, γ-Sn and In_2Bi phases grow in a coupled way. G = 3.3 K/mm, and δ = 23 µm.

The initiation of the third phase, *i.e.* β-In (B), creates the second interphase boundary in the system, meaning AB boundary. The onset of the β-In formation is basically a 3D mechanism, in which the phase invades the front while providing side-branches. The initiation of the third phase took place in a way that from the beginning, the created interphase boundary naturally appeared with a certain form of anisotropy in the interfacial energy.

Figure 5-3 shows the onset of the third phase, *i.e.* β-In, and the formation of associated AB interphase boundaries which contain facets whereas AC interface is nearly growing parallel to the growth direction. The facet directions are well-defined fashion within the EG. The inclined angles of the facets with respect to the growth direction are about +22° (inclined clockwise) and -22° (inclined counterclockwise). Close snapshot of the solidification front is illustrated in Figure 5-4.

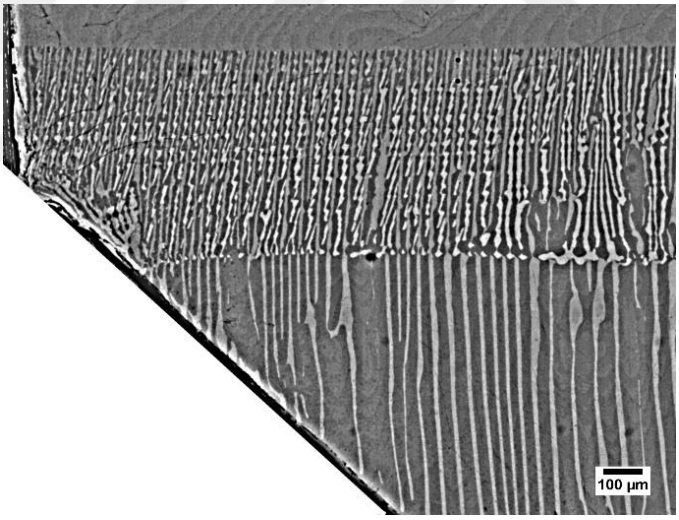

Figure 5-3. Initiation of β-In (B) phases during DS experiment. The initiation of the third phase is a 3D mechanism in which the phase invaded laterally over the front. The S/L interface was within the funnel section of the sample. Velocity is continuously increased from 0.090 to 0.180 µm/s. G = 3.3 K/mm, and δ = 23 µm.

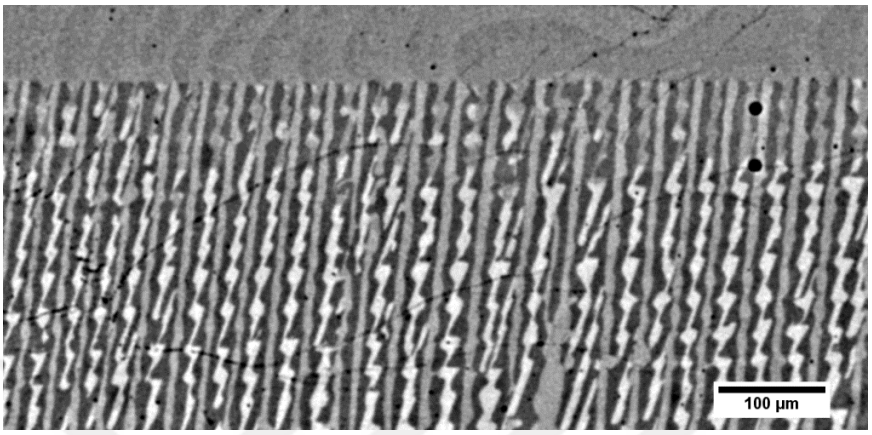

Figure 5-4. Close snapshot of the microstructure with the faceted AB boundary and regular AC boundary. B (white) phase does not wet the glass close to T_E. V = 0.180 µm/s, G = 3.3 K/mm, and δ = 23 µm.

Two main points are immediately noticed about this microstructure in Figure 5-4: first, even though the AB interphase boundary contains facets, the overall microstructure arrangement is mostly ABAC. This means that the anisotropy of the interphase boundary, does not break the symmetry of the basic state in early stages of the growth. Secondly, the microstructure is apparently two dimensional; meaning the morphology of the phases is still lamellae. This can be understood from the top and bottom images of the microstructure, shown in Figure 5-5.

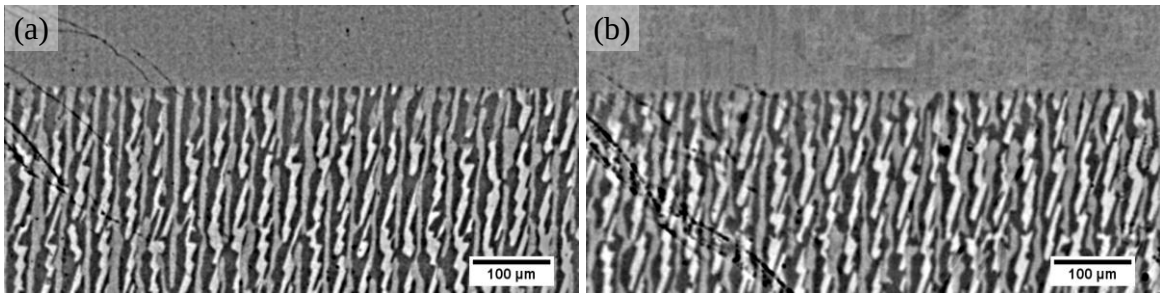

Figure 5-5. The early growth stage of the pattern with faceted AB boundary and isotropic AC boundary. (a) Top microstructure. (b) Bottom microstructure. V = 0.180 µm/s, G = 3.3 K/mm, and δ = 23 µm.

Figure 5-6 shows the evolution of the pattern after ~ 1350 µm growth length. The evolution process involves coupling of the β-In (B) and In_2Bi (A) phases, while the γ-Sn (C) phase is rejected either to the side of coupled β-In and In_2Bi regions in X direction or to the other side of the sample, *i.e.* in Y direction. In addition, a considerable number of branching events within the two-phase region occurs. Note that the inclination angle of the AB boundary with respect to Z is comparable to the initial inclination angle measured from the microstructure shown in Figure 5-4. This suggests the direction is dictated by a certain crystallographic property of the AB boundary, since the angle doesnot change with the velocity as in the case of tilted eutectic structure [77].

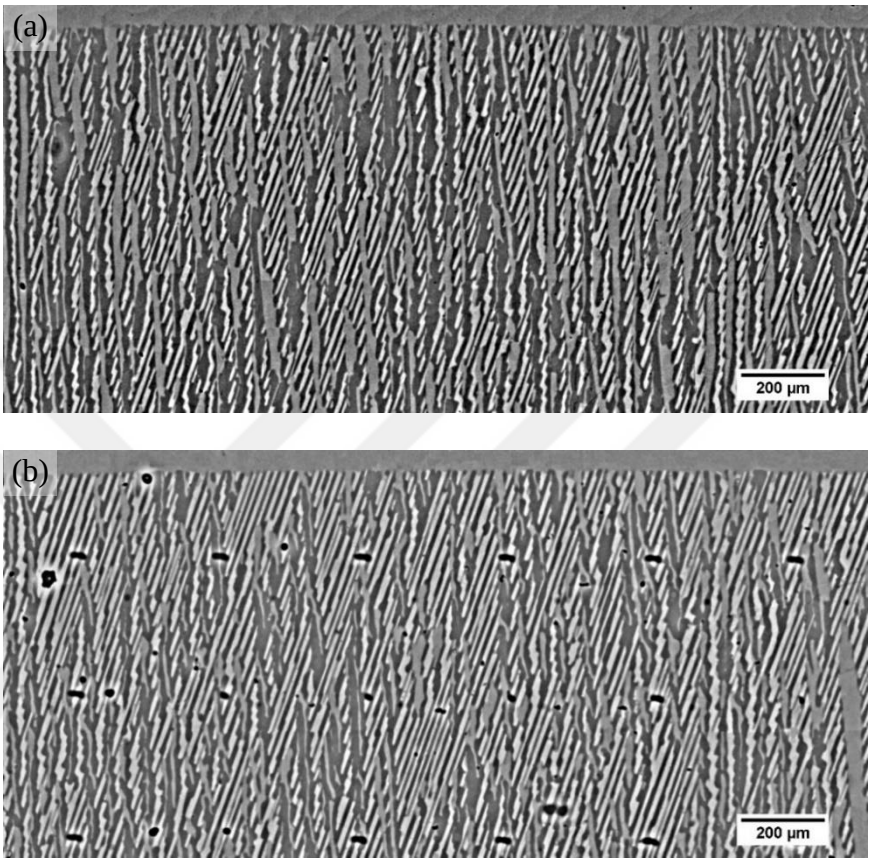

Figure 5-6. The evolution of the microstructure in Figure 5-5 after ~ 1350 µm. The microstructure evolves to coupled AB region and isolated C phase. (a) Top microstructure. (b) Bottom microstructure. V = 0.130 µm/s, G = 3.3 K/mm, and δ = 23 µm.

The last step of the evolution process is accompanied by further coupling of A and B phases and rejection of almost all C phases to either sides of the AB region in X direction or to the other side of the sample in Y direction. Figure 5-7 shows the evolution of the pattern after ~ 10000 µm growth length. It is clear now that the microstructures at top and bottom views are completely different. This means that the morphologies of the phase alter from

regular lamellar shape. We called the three-phase structure where two phases are coupled on one side of the sample and the third phase is rejected to the other side of the sample a "separated structure".

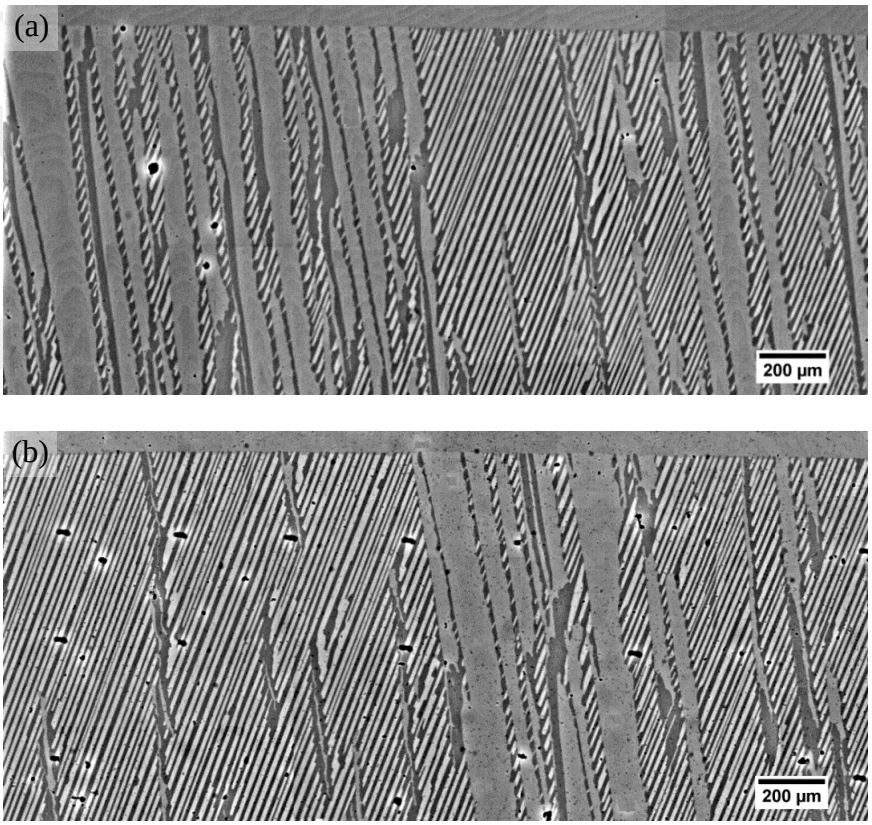

Figure 5-7. The evolution of the pattern after 10000 μm growth length. (a) Top microstructure. (b) Bottom microstructure. V = 0.080 μm/s, G = 3.3 K/mm, and δ = 23 μm. Black spots on bottom image are dust particle on the microscope lens during experiment.

Comparing the microstructure shown in Figure 4-12 in *chapter 4*, in which the grain in transient state grown directionally, with the one shown in one Figure 5-4, one can realize the similarities between them. In Figure 5-8 examples of two microstructures are brought together where (a) is the initial stage of the separated structure and (b) is transient state of the locked pattern. Microstructural features such as facet formation on AB boundaries, occasional branching events within AB regions, the floating behavior of AC boundaries are comparable between these two structures. If it can be accepted that the microstructure formed during the initial stage of the separated structure, is the same with that of the transient state, it can be concluded that the inclination angle of one of the boundary, in this case AB boundary, is located in the forbidden orientation angular range. Selection of the faceting direction for the surfaces which are located in the forbidden orientations is argued for the case of anisotropic S/L interface in [99]. It was stated that the S/L surface corresponding to a forbidden orientation can choose one of three possible states: being rough at the atomic scale, faceted at the atomic scale, or multifaceted at the microscopic scale. While being rough and faceted at the atomic scales represent equilibrium, multi-faceting represents a time-dependent state in which the interface evolves toward equilibrium. For the anisotropic S/S interface similar dynamics can be considered, therefore, it is suggested that the microstructure shown in Figure 5-7 is the consequence of the selection of the facets direction (~22° with respect to Z direction) in AB interphase boundary located in the forbidden orientation range and it evolves toward equilibrium with time.

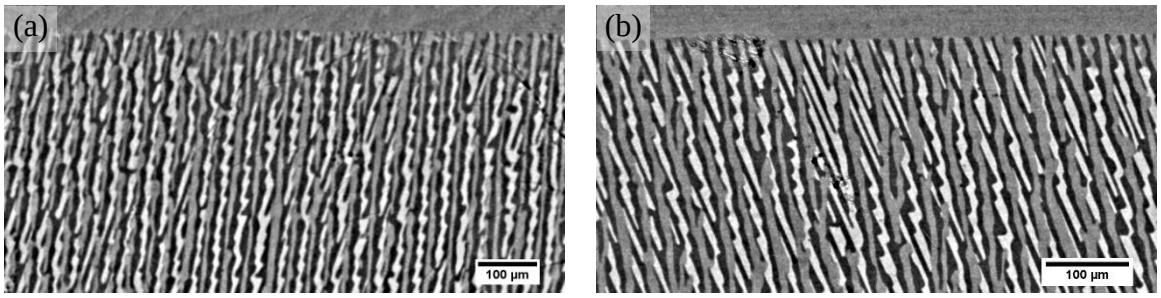

Figure 5-8. The comparison of microstructures formed during initial stage of separated structure and the transient state of the locked pattern. (a) The initial growth stage of the separated structure in DS experiment. V = 0.180 µm/s, G = 3.3 K/mm, and δ = 23 µm. (b) The microstructure formed by the directional solidification a transient state corresponding to the forbidden orientation. V= 0.250 µm/s, G = 5.1 K/mm and δ =13 µm.

The measured inclination angle of AB boundary within the separated region stays the same at three different growth velocities during the experiment, (within experimental errors). This indicates that the inclination angle is fixed by the crystallography of the boundary and it is velocity-independent. Table 5-1 shows the measured inclination angle of the AB boundary at different velocities.

Table 5-1. The measured inclination angles of AB boundary at different velocities.

V(µm/s)	Angle $_{mean}$ (°)	STD (°)
0.080	22	0.9
0.130	20	0.6
0.180	23	0.8

To investigate if the phase-diffusion process is active within two-phase AB alternation, the spacing is defined as the width of one motif of AB, and measured in different growth length from several coupled AB regions. Even though the measured area is not large, if the phase-diffusion was active, the homogeneous spacing would form after a long growth length. Figure 5-9 shows an example of a region from separated eutectic grain along with the measured spacing value within the two-phase structure. In this example, the measured spacing ranges from 9.6 to 30.6 μm and this range doesnot reduce. Nonhomogeneous and time-independent spacing distribution indicate lack of phase-diffusion process within AB structure. This leads to the conclusion that AB alternation in separated structure is crystallographically locked structure.

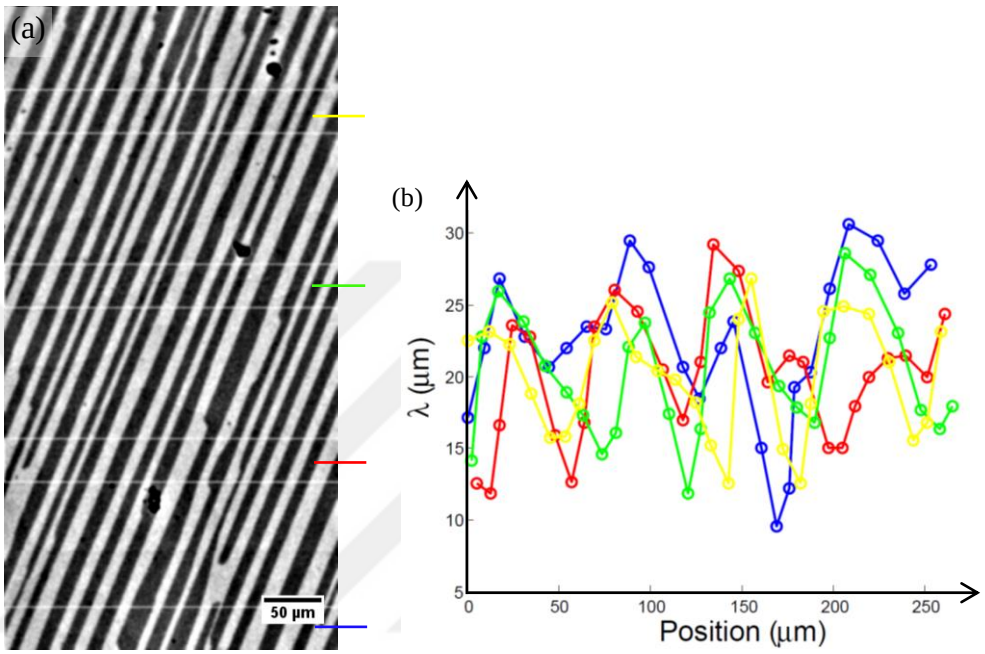

Figure 5-9. Locked two-phase region in separated structure. (a) The two-phase region in separated structure. The alternation AB structure is inclined with respect to growth direction. (b) The spacing measured at different locations. V = 0.080 µm/s, G = 3.3 K/mm, and δ = 23 µm.

5.3.2 Separated structure formation during RDS pattern

During RDS experiments, upon rotation of specific EG, the separated structure is observed. However, the features of this structure are somehow different than what is discussed in section *5.3.1*. Figure 5-10 illustrates top and bottom views from two

distinguished eutectic grains during RDS experiment. While on right-hand side typical ABAC pattern is growing floating, on left-hand side separated structure forms such as thermal gradient, composition, and similar growth velocities. Coexistence of these two dissimilar eutectic grains at the same experimental conditions ensures that two grains belong to different categories in terms of the interphase energy features.

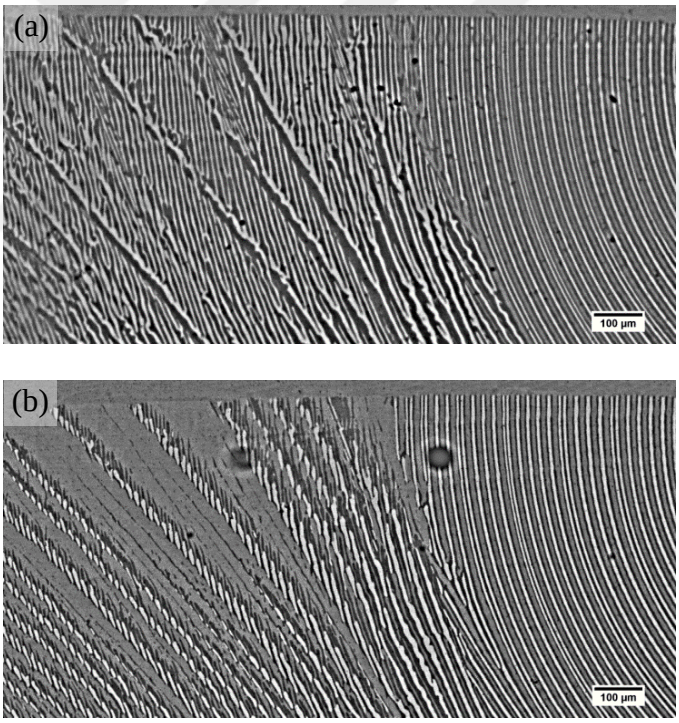

Figure 5-10. Coexistence of the isotropic eutectic grain with ABAC stacking sequence with the separated structure at the same experimental conditions. (a) Top microstructure. (b) Bottom microstructure. CW, $\omega = 0.019$ °/s, $G = 5.1$ K/mm, and $\delta = 13$ µm.

The formation of the separated structure in this case is accompanied by the coupling of the β-In (B) and In_2Bi (A) phases, similar to the structure given in Figure 5-7. The evolution of the pattern, however unlike the separated structure discussed in Figure 5-7 goes along with the formation of many branches from the main "*trunk*". Also, in this type, the branched arms grow parallel to the growth direction. Figure 5-11 shows the evolution of the pattern to a complete separated after 95° rotation of the sample. At this state of the evolution of the alternation of β-In and In_2Bi phases on top view of the sample, Figure 5-11 (a), and the bulk single γ-Sn phase on the bottom view of the sample, Figure 5-11 (b).

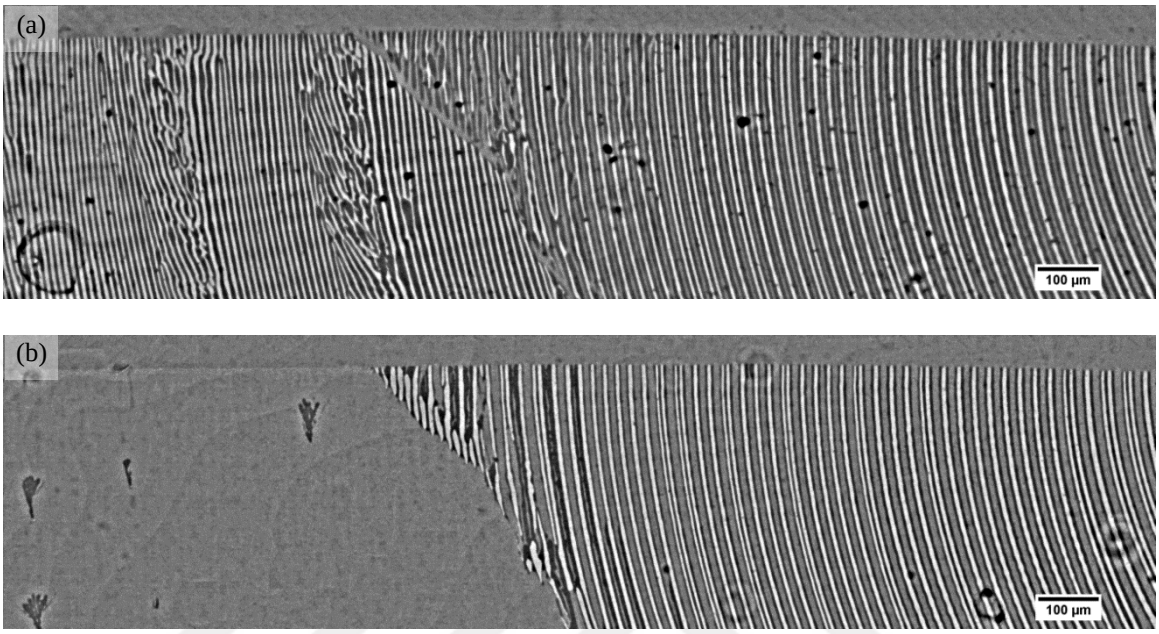

Figure 5-11. The growth of a separated structure during an RDS experiment next to a typical isotropic grain with ABAC arrangement. (a) Top microstructure. (b) Bottom microstructure. CW, ω = 0.019 º/s, G = 5.1 K/mm, and δ = 13 µm.

The main *trunks* observed during formation of separated structures are considerably tilted with respect to the overall growth direction and each has slightly different tilting angles with respect to each other. Figure 5-12 shows top and bottom views of the separated microstructure formed during another RDS experiment along with the micrograph showing the trace of AB interphase boundaries. The measured inclination angles of the main *trunks* with respect to Z direction shows an increase as they are approaching to the edge of the sample. The relation between the tilting angle of the *trunks* and the velocity is an open question.

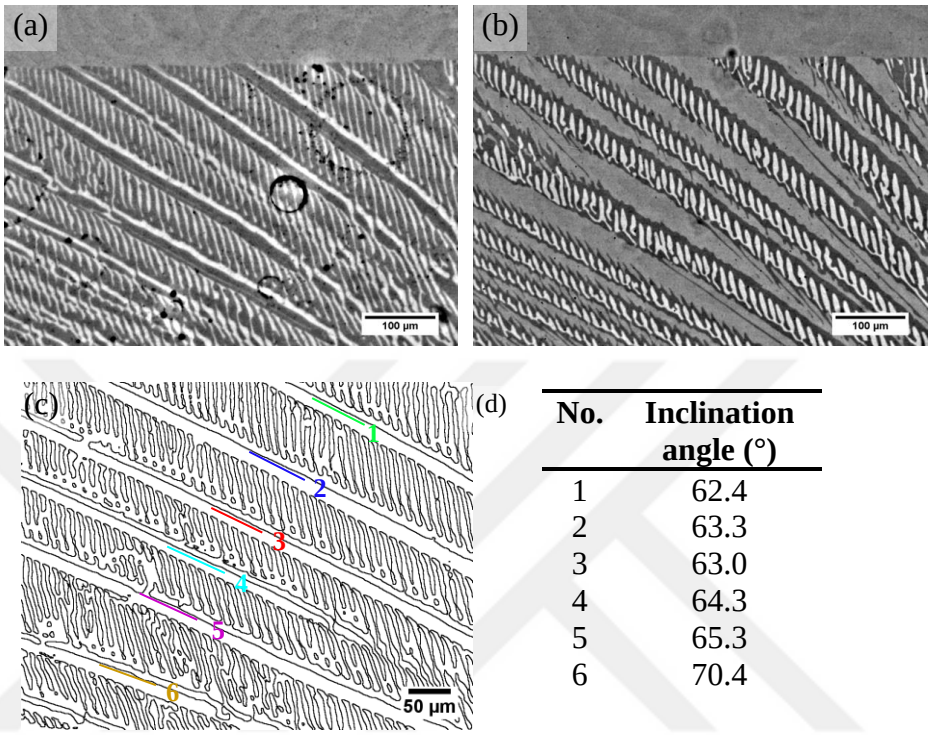

No.	Inclination angle (°)
1	62.4
2	63.3
3	63.0
4	64.3
5	65.3
6	70.4

Figure 5-12. The early stage of separated structure formation during an RDS experiment. (a) Top microstructure. (b) Bottom microstructure. (c) Micrograph of the trace of AB interphase boundaries, after 6° rotation of the microstructure shown in (a). The marked lines are the main *trunk* direction. (d) The measured inclination angle with respect to Z direction of the marked lines on (c). CW, ω = 0.026 º/s, G = 5.1 K/mm, and δ = 13 µm.

The traces of main *trunks* are clearly deviated from the direction of travel and are straight lines. For the six main *trunks* traces shown in Figure 5-12 (c), the linear fitting on the AB boundary data has been done, as shown in Figure 5-13 and Table 5-2. The R-squared

value (R^2) confirms the linearity of those *trunks*. The intercept values of the lines are not given since they take different values based on the reference point on the image.

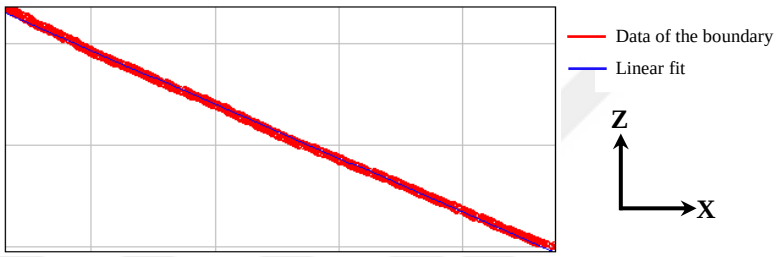

Figure 5-13. Example of linear fitting on the main *trunk* numbered as 1, in Figure 5-12.

Table 5-2. The linear fit equation of the six *trunks* shown in Figure 5-12 with the corresponding R^2 values.

No.	**Y = *b* + *a*x**	**R^2(%)**
1	Y= b_1-0.532x	99.86
2	Y= b_2-0.496x	99.96
3	Y= b_3-0.499x	99.93
4	Y= b_4-0.470x	99.94
5	Y= b_5-0.460x	99.85
6	Y= b_6-0.369x	99.70

The tilted main *trunk* with side-branches can be compared to the tilted dendrite formation. While the latter is a result of anisotropy in S/L interface energy, the former is due to the anisotropy in S/S interphase boundary. Figure 5-14 shows a typical dendritic array in the present of the anisotropy in S/L surface energy obtained by phase-field simulation during

directional solidification of a binary alloy. With strong anisotropy in S/L interface and at velocities above a certain threshold, dendrite morphologies formed with a tilt angle, and their growth directions are close to the preferred growth direction [53].

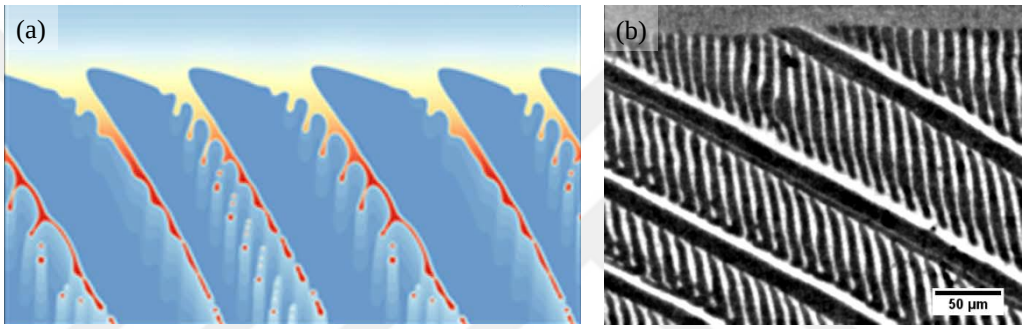

Figure 5-14. Comparison between tilted dendrites and the separated structure. (a) A typical tilted dendritic array with side-branching [53]. (b) Tilted main *trunk* and side-bracings in a separated eutectic grain. CW, $\omega = 0.026$ °/s, G = 5.1 K/mm, and $\delta = 13$ µm.

Evolution of the separated structure during an RDS experiment has significant dynamical details. Let's first examine a microstructure corresponding to a relatively isotropic portion of the interphase energy and therefore, the lamellar structure with ABAC arrangement follows the direction of the travel. Figure 5-15 (a) and (b) shows the microstructure formed during this step from top and bottom views. Even though the pattern has several faults in the arrangement, it can be considered as nearly-isotropic structure. Figure 5-15 (c) and (d) shows the evolution of the pattern after ~ 21° rotation of the sample.

Two main points can be extracted from the pattern formed during this step. First the lamellar structure is inclined with respect to the overall growth direction. Note that no facets exist in neither interphase boundaries. Secondly, the evolution process is accompanied by a decrease in width of C phases on top and an increase in their width on the bottom view. Indeed, at this growth velocity regime, the volume fractions of the phase are fixed by the phase diagram and it is not surprising that when C phase is getting narrower in one side, its width must increase on the other side. This step seemingly is the onset of phase morphology alternation from regular lamellar to yet-unknown one.

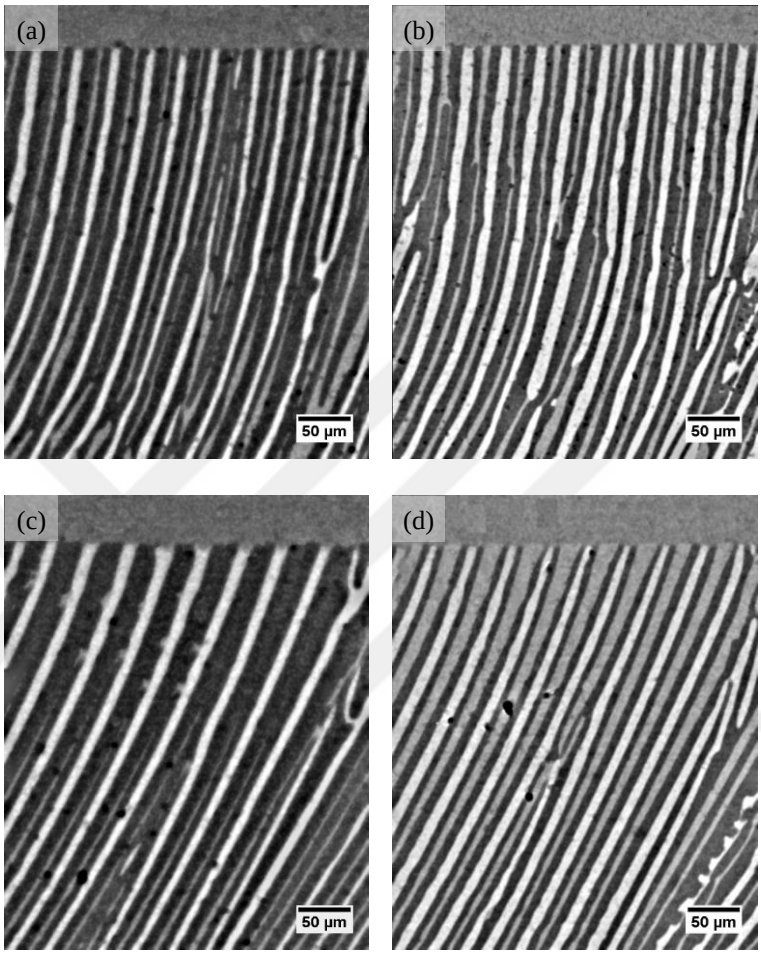

Figure 5-15. Onset of formation of the separated structure during an RDS experiment. (a) Top view. (a) Bottom view. (c) The evolution of the pattern to an inclined lamellar structure with a decrease in the width of C phases from top view after 21° rotation. (d) The evolution of the pattern to inclined lamellar structure with an increase in the width of C phase from bottom view. CCW, $\omega = 0.016$ °/s, G = 5.1 K/mm, and $\delta = 13$ µm.

After ~ 45 ° rotation of the sample, complete phase separation occurs. As it can be seen from Figure 5-16 (a) and (b), while top microstructure has the alternation of the A and B

phases, the bottom has only the C phase. By elimination of In_2Bi and β-In phases from bottom side, all γ-Sn phases are allowed to merge to form a single phase. As phases within one eutectic grain has the same crystallographic orientation, the merging occurs easily. Analogous to what is discussed in Figure 5-10, the successive lamellar splitting occurs in the two-phase AB region. The newly generated arms are in the direction of the thermal gradient, indicating that AB interphases are isotropic. One possible explanation to the phenomena can be that the AB interphase boundaries are forced by the anisotropy of the AC boundary, in any form, to incline significantly with respect to the overall growth direction. By elimination of the AC boundary during rotation, the driving force on the AB boundary is correspondingly removed. Therefore, the AB boundary no longer favors to incline with respect to overall growth direction. The splitting and providing new arms which are now able to follow the direction of the travel is the potential mechanism that the boundary can return to the favored direction in the absence of anisotropy, *i.e.* the imposed thermal gradient direction. Figure 5-16 (c) and (d) illustrates the complete separation of the AB alternation and single C phase after ~ 56° rotation of the sample.

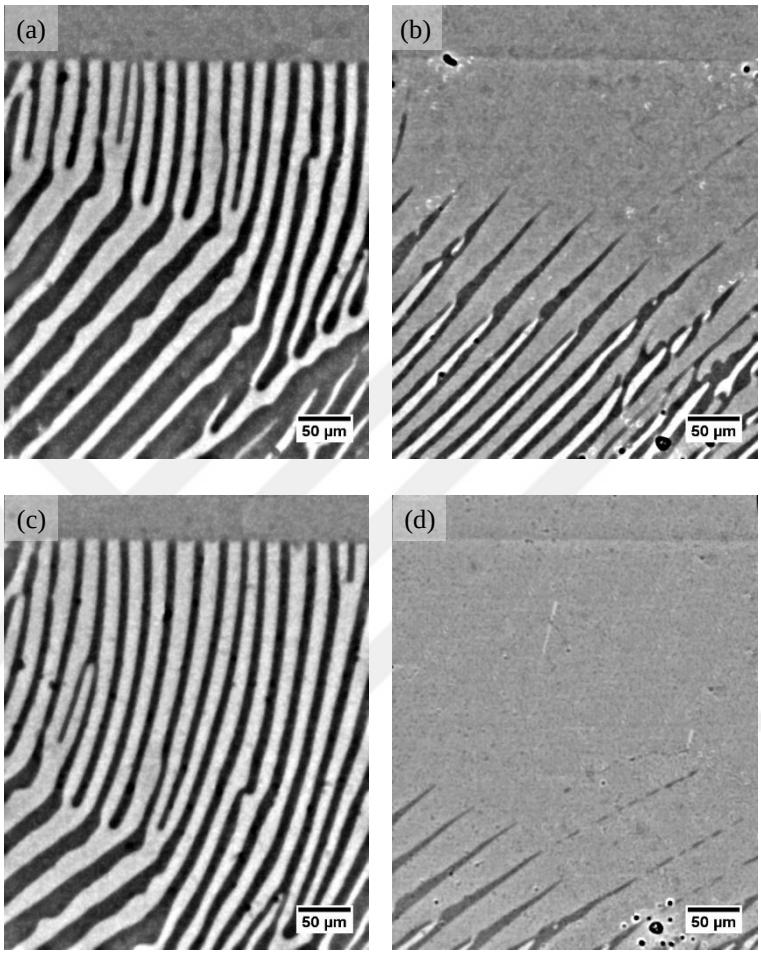

Figure 5-16. Evolution of the pattern to complete separated structure (a) Top view when the branching occurred within the two-phase structure after 45° rotation. (a) Bottom view showing the diminishing of the AB and AC boundaries and merging all of C phases to form a single crystal of γ-Sn. (c) Nearly homogenous distribution of A and B phases after 56° rotation. (d) The bottom view of the structure in (c) shows the formation of single γ-Sn crystal. CCW, $\omega = 0.016$ °/s, G = 5.1 K/mm, and $\delta = 13$ µm.

Three-phase eutectic growth in the presence of S/S anisotropy in quasi-2D samples, Part B

Figure 5-17 shows full rotation of the grain discussed in Figure 5-15 and Figure 5-16. The characteristic features of the grain evolution can be categorized as follows: there are four nearly-locked angular ranges shown by the solid lines NL_1 and NL_2. NL_1 and NL_2 have 180° symmetry. Two relatively wide angular ranges corresponding to the separated region with 180° symmetry as well, shown by the dashed curves, S. NL_1 and NL_2 states are connected by a nearly-isotropic transient state, which is more regular close to the center.

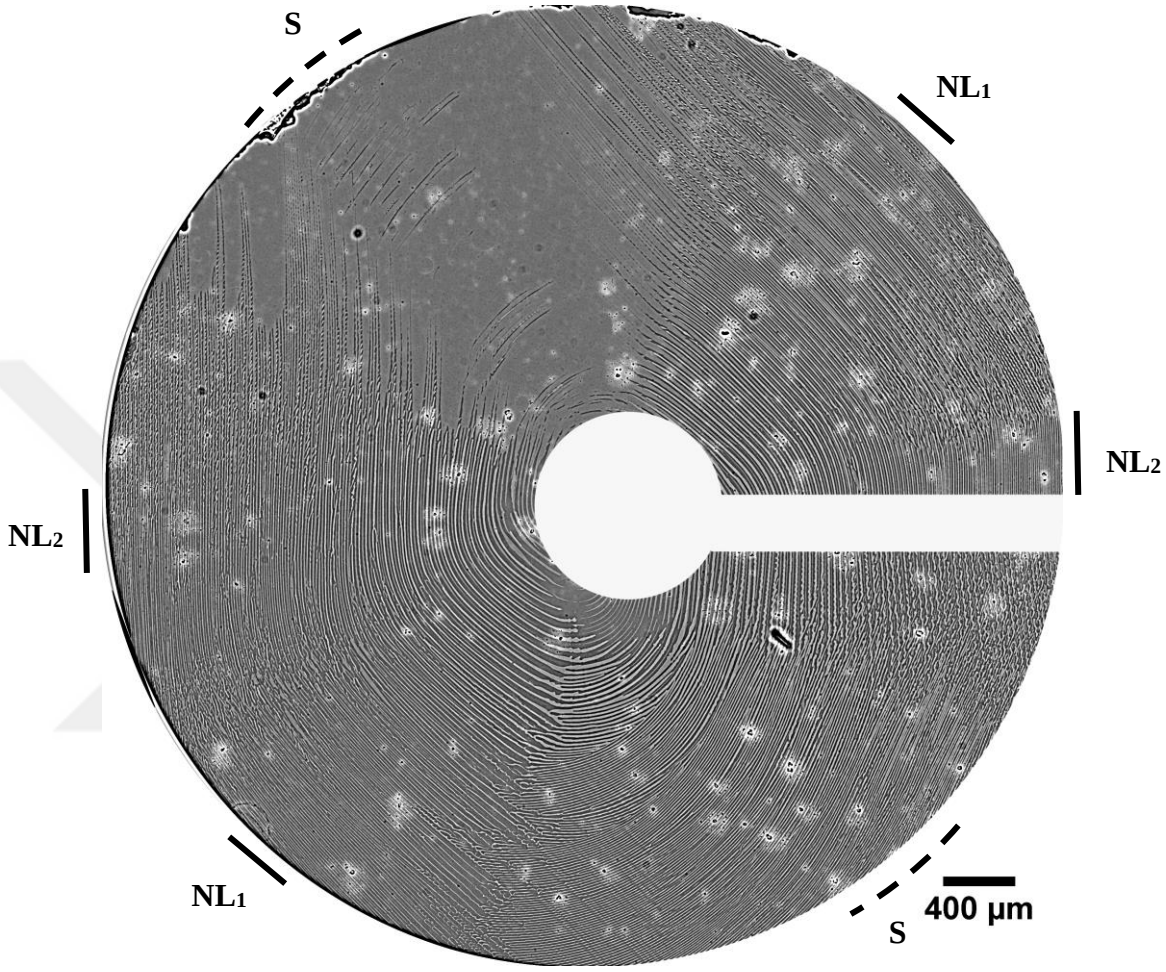

Figure 5-17. Full evolution of the grain having separated structure during an RDS experiment. Black dots are dirt on the glass plate. CCW, ω = 0.010 º/s, G = 5.1 K/mm, and δ = 13 µm.

5.3.3 Directional growth of the separated structure formed by RDS

To investigate the behavior of the separated structure while growing in on direction, same method described in *4.3.2* is used. The pattern is rotated to reach the separated structure

and subsequently, the all other structures are melted to have mostly a seed in the bottom of the sample with the characteristic separated nature. Then, directional movement is started to examine how the boundaries would respond to force to grow in a fixed direction which is the thermal gradient direction. Figure 5-18 shows the microstructure formed after 550 μm growth length at V = 0.150 μm/s. The two-phase structure in the bottom side of the image is grown by RDS and then it was subjected to directional growth.

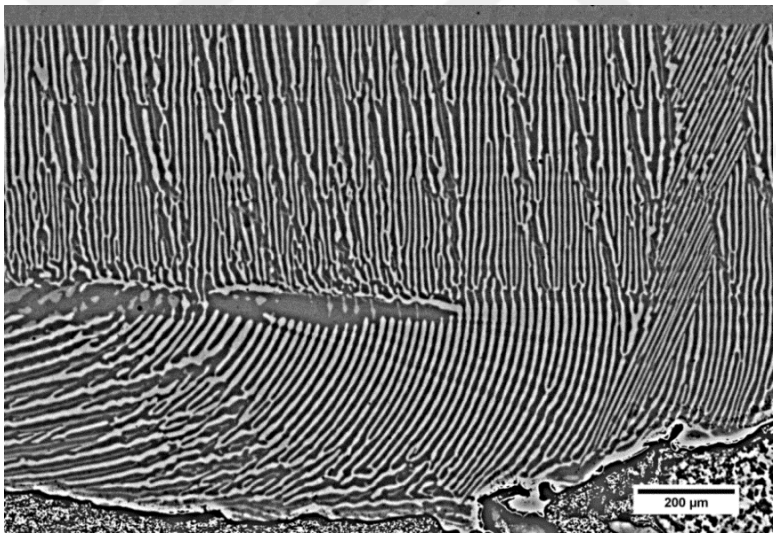

Figure 5-18. Directional growth of the separated structure. V = 0.150 μm/s, G = 5.1 K/mm, and δ = 13 μm.

Apparently, there are at least two different types of separated structure region. In one of them on the left side of Figure 5-18, AB boundary is isotropic, similar to Figure 5-16,

versus, close to the right side of image shown in Figure 5-18, the AB boundary is locked to a certain direction, similar to Figure 5-7. The continuous growth of two-phase AB structure with isotropic interphase boundary in DS is not surprising as it was already isotropic during rotation. In other words, when the interphase boundary is kept in the isotropic portion of its corresponding Wulff plot, it will essentially grow in the direction of the imposed thermal gradient during DS experiment. However, the formation of the locked two-phase AB in this example is not understood at the moment. Especially, it seems that it is initiated from the same *trunk* as the isotropic two-phase AB initiated.

The pattern is let to directionally grow and after 1500 μm growth length, two different separated structures are clearly distinguishable as illustrated in Figure 5-19 (a). While on the right-hand side the locked two-phase AB is growing at an angle with respect to Z, right next to it, the isotropic two-phase AB structure is growing in the direction of Z. For both structures, the bottom view has bulk single C phase, as shown in Figure 5-19 (b). Two different two-phase AB structures indeed have almost the same structure on top view. Note that there exists a eutectic grain on the left-hand side of the images with regular lamellar ABAC pattern with same faults.

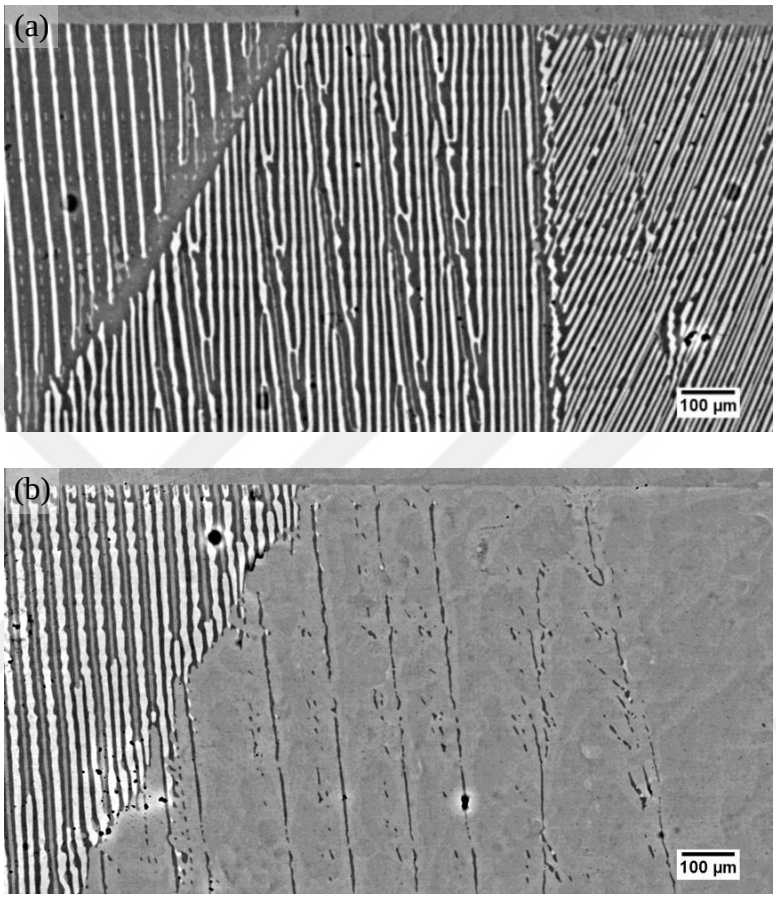

Figure 5-19. Two different separated structures formation. (a) The microstructure in the top view consists of three different structures: on left-hand side, a grain with ABAC arrangement (with very narrow C phase), in the middle the isotropic two-phase AB and on the right-hand side, locked AB two-phase. (b) Bottom view consists of two distinguishable microstructures: on the left-hand side, a grain with ABAC arrangement and on right-hand side bulk single C phase. V = 0.150 μm/s, G = 5.1 K/mm, and δ = 13 μm.

Undoubtedly, the separated structure is a 3D microstructure and morphologies of the phases must be different from lamellar. Considering two-phase alternation of AB structure

on one side and single C phase on the other side of the sample, the possible morphologies in cross-sectional view are schematically shown in Figure 5-20 (a) and (b) in comparison with the regular ABAC structure, Figure 5-20 (c). Although it is theoretically possible to form Figure 5-20 (b), the formation of this structure would be accompanied by the formation of nonexistent BC boundary in the system, which is indeed not favored from energetic point of view. In addition, the growth of β-In and γ-Sn next to each other is not favored from the solute distribution point of view. Due to similar chemical composition of them, most of the solute exchange occurs between β-In and In_2Bi phases and between γ-Sn and In_2Bi phases. Therefore, the growth of β-In and γ-Sn side-by-side is expected to increase the diffusion undercooling. Conversely, schematic proposed in Figure 5-20 (a) is the reasonable solution to the morphology of the phase in the separated structure, to adjust not only the surface area to have the possible minimum value without creation of new interphase boundary but also it did not change the efficient solute exchange path.

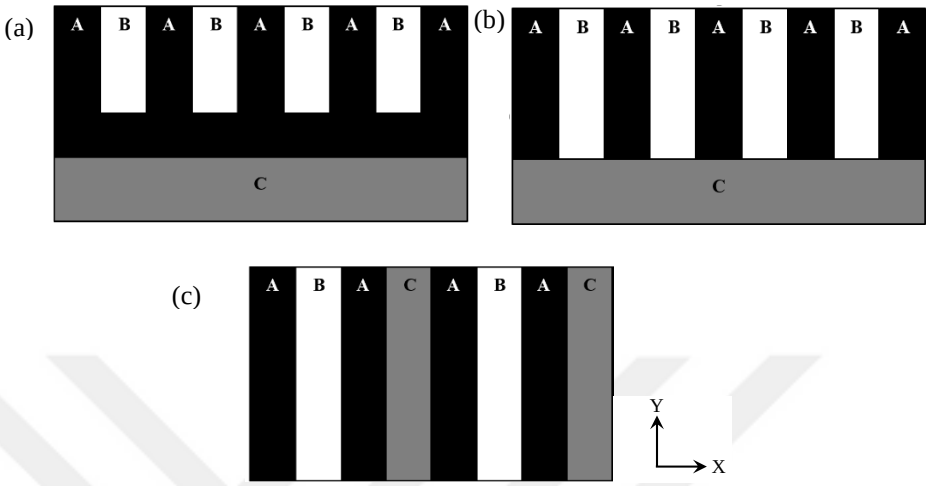

Figure 5-20. Schematics of possible morphologies of the phases in the separated structure along with the basic ABAC lamellar morphology. (a) Alternation of the AB on one side such that a continuous A phase encloses B phases and bulk C on the other side. (b) A and B phases have the same morphology; C phase is still lamellae. The AC phase is parallel to the glass wall. (c) Isotropic lamellar ABAC pattern, each phase is a lamella ideally perpendicular to the glass wall.

To examine the cross-section of the patterns formed in Figure 5-19, the alloy is removed from the glass container and vertically fixed between two stainless steel pieces with mirror-like surfaces and together mounted in epoxy and prepared for conventional metallography. The cross-section of the sample was observed under a Scanning Electron Microscope (SEM), using Backscattered Electron (BSE) detector. It should be mentioned that, in SEM/BSE images, the In_2Bi has white color while two others have gray color. The similar chemical composition of β-In and γ-Sn phases causes unremarkable color contrast, and both have gray

color in the BSE detector used in this study. However, using Energy Dispersive X-ray (EDX) analysis, the phases are distinguishable and by this way, the identity of the phases is established. Figure 5-21 shows the cross-sectional view of a standard ABAC pattern. In an isotropic ABAC-type pattern, each phase is a lamella extending from one glass wall to the other glass wall, nearly normal to them.

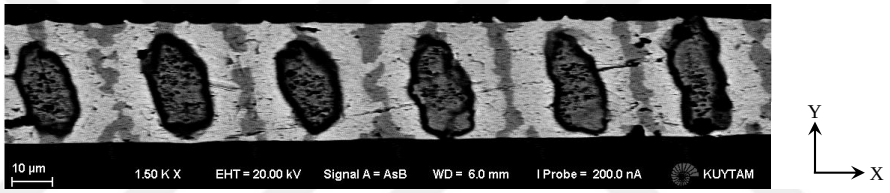

Figure 5-21. The regular ABAC pattern from cross-sectional view. In isotropic eutectic grain, each phase is a lamella confined between glass walls. Due to etching in the air, and decomposition of the phases, the interphase boundaries are not straight as they were in real-time images.

Figure 5-22 (a) and (b) shows the cross-section of the microstructure corresponding to locked and isotropic two-phase AB in the separated structures, respectively, in Figure 5-19. Geometrically speaking, the proposed schematic in Figure 5-20 (a) is the corresponding morphologies of the phases in the separated structure. While C phase is a continuous phase on the top side with lamellar morphology, A phase is the continuous matrix in AB alternation, which encloses B phases. From diffusional point of view, in such phase arrangement solute

distribution should be similar to ABAC lamellar alternation. In_2Bi phase acts as a source to provide Sn element to both β-In and γ-Sn phases as it does not contain any Sn in its chemical composition. On the other hand, both γ-Sn and β-In phases have higher Sn and lower Bi content in their chemical composition than In_2Bi phase. Thus, γ-Sn and β-In phases does not need to grow in parallel, as it is the case in ABAC pattern. Existing two mirror planes in this arrangement, in the middle of A and B phases, is likely responsible to the formation of the steady-state separated microstructures, specifically in the reported DS experiment which was sufficiently long enough to reach to nearly-steady state conditions.

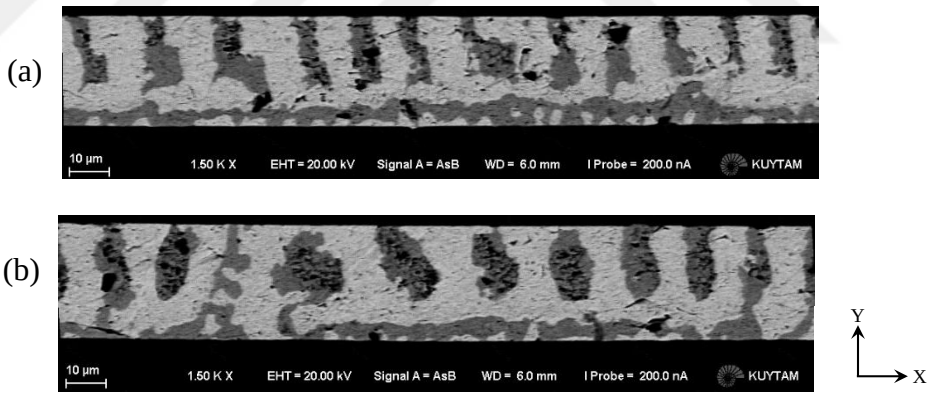

Figure 5-22. SEM/BSE images of the cross-section of the microstructure in Figure 5-19. (a) Locked AB two-phase in separated growth pattern. (b) Isotropic AB two-phase in separated growth pattern.

The changes in the separated structure are not only related to the shape and size of phases, but also it is accompanied by 90° rotation of AC boundary. It means that while in

normal lamellar structure both interphase boundaries are perpendicular to the glass wall, in the separated structure AC boundary is parallel to the glass wall. Such rotation of surface most likely relates to off-normal component of the anisotropy operating on AC surface, described by D. Hoffman and J. Cahn [94]. It is suggested that in this separated structure, off-normal component of the anisotropic surface, AC surface, provides the necessary torque to rotate the AC boundary.

Additionally, the shapes of B phases are different in two cases shown in Figure 5-22. In the locked AB structure, the B phases have somehow faceted shape while in the isotropic one, they have more rounded in shape. This can be related to the different properties of AB interphase in two cases. In Figure 5-22 (a), due to anisotropy in AB interphase boundary and locking to a certain direction, the shape of B phases are faceted-like whereas the rounded shape of B phase is the result of orientation-independent property of the AB boundary in Figure 5-22 (b).

5.4 Conclusion

In this chapter, a new microstructure called “separated structure” in three-phase eutectic system is introduced which, to our best knowledge, has not been reported in literature so far. This microstructure is characterized by the coupling of two phases (In_2Bi and β-In) out of three in the system on one side of the sample, and single crystal of the third phase (γ-

Sn) on the other side of the sample. The separated structure is further classified into main groups based on crystallographic characteristics of the AB boundary:

In the first type, the coupled AB structure is inclined with respect to the overall growth direction and the inclination is clearly related to locking of the boundary. The characteristic features of the locked AB pattern can be detected in this pattern: (***i***) The locking angle is independent of the growth velocity, (***ii***) The spacing in AB region is non-homogenous and time-independent, *i.e.* no phase diffusion, (***iii)*** The formation of facets in AB boundary through early stages of the growth are associated with the forbidden orientation of the AB boundary. In the early stage of the growth and absence of AB interphase boundary, *i.e.* AC boundary grows relatively parallel to the thermal gradient. As it is not possible to change its relative crystallographic orientation upon growth, *i.e.* the properties of the interphase orientation are fixed and independent of the experimental conditions, their behavior in the initial growth may indicated that at least, there is not a significant anisotropy associated with the AC boundaries. The AB coupling and C rejection process is a slow and a gradual event. The successive branching events within AB region assist the coupling process of these two phase and C phase is rejected from the coupled region. It is proposed that the final microstructure results from the selection of the minimum energy orientation of the AB boundary. It should be mentioned that the formation of this pattern was a rare event in DS experiments.

The second type of the separated structure is observed during RDS experiments. Despite coupling of two phases (A and B) and rejection of the third phase (C), two-phase region is an isotropic structure. The triple-point junctions within AB alternation floatingly follow the direction of imposed thermal gradient. The RDS experimental results reveal that the formation of such structure should be related to the anisotropy in the interphase energy. In the studied example, the eutectic grain has the separated structure with 180° symmetry and it is reproducible in several full turns of the sample. The evolution of the separated grain during an RDS experiment is highly complex, and in addition to the angular ranges where separation occurs, it consists orientations wherein nearly-locking occur. In addition to different crystallography of AB boundary compared to previous example of separated structure, the kinetic of the event is dissimilar. The formation of separated structure during RDS experiment is fast and clearly related to the shape of the corresponding Wulff plot. Whenever the interphase boundary reaches to the certain angular range, the separation rapidly occurs. The process should not be related to experimental conditions because the same phenomena are observed in different rotation speeds and samples. In contrast to the first type, formation of the separated structure during RDS was a frequent event.

Cross-sectional post-mortem analysis of the separated structure reveals that the morphologies of all phases are changed, and the microstructure is no longer 2D during steady-state. In_2Bi phase is a continuous matrix and encloses β-In phases, whereas γ-Sn phase is a lamella oriented through the width of the sample instead of the sample thickness. Not

only the shape the phases are affected by the anisotropy, but also the direction of the interphase boundary is changed. In this separated structure, it is proposed the off-normal component of the surface energy of the AC boundary provides the necessary torque to rotate the AC boundary from normal to the glass wall to parallel to the wall. Despite the remarkable variations in the morphologies of the phases, the arrangement is in a way that the solute redistribution ahead of the solidification front does not depart far from the ABAC stacking sequence. In the new morphology, two mirror planes exist in the middle of A and B phases which is suggested to assist the steadiness of the structure.

Chapter 6 : Other microstructures

6.1 Introduction

It was shown in the previous chapters that the lamellar structure with ABAC type-growth pattern is the basic state of the three-phase system in absence of S/S anisotropy. In the presence of different forms of anisotropy in AB and/or AC, however, various microstructures are identified and characterized. Within the employed experimental conditions, such as growth velocity, thermal gradient, sample thickness and so on, in addition to the microstructures that were characterized in the previous chapters, other nearly stationary microstructures observed during this study. Among the parameters that affects the microstructures, the influences of the characteristic features of the interphase boundaries and the sample thickness seem to be the pronounced factors on the formation of various patterns. Even though the formation mechanisms of all the observed microstructures are not well-understood, these microstructures are categorized, and their possible origins discussed. These microstructures are classified into two broad groups based on their interphase boundary properties as nearly-isotropic microstructures and anisotropy-driven microstructures.

6.2 Experimental procedure

The DS and RDS experimental methods explained in *chapter 2* and *3* were performed to obtain the results explained in this chapter.

6.3 Results and discussion

6.3.1 Nearly-isotropic microstructures

In this type of microstructures, it is suggested that the foremost factor to determine the microstructures is the geometry of the sample. This does not oppose the impact of the possible interphase anisotropy; however, the decreased confinement effect on the growth dynamics is pronounced.

6.3.1.1 Rumi [1] structure

The microstructure called “Rumi” structure is characterized by the floating movement of the triple-point junctions parallel to the solidification front. In_2Bi and β-In phases are spiraling while γ-Sn phases are forming almost continuous lamellar morphology. In this microstructure, the lamellar structure is non-continuous however, interestingly, the phase alternation is nearly-ABAC. In this structure, B and C phases are sometimes connected but continuous BC interphase boundaries do not exist. Figure 6-1 shows one example of “Rumi” structure which grew nearly stationary for about 2700 μm.

[1] The name “Rumi” is inspired by the Persian poet, theologian, and Sufi mystic. His followers founded Mevlevi Order, which is a famous dance of whirling Dervishes. The freely whirling of the A and B phases around each other in this microstructure resembles the dance performed by the Rumi followers.

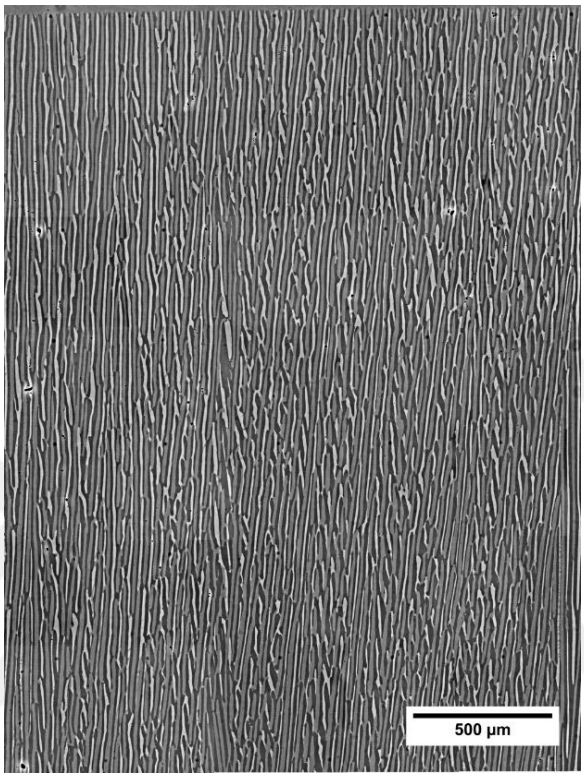

Figure 6-1. “Rumi” structure observed in a DS experiment. The microstructure is characterized by freely moving triple-point junctions and non-continuous lamellae. V = 0.150 µm/s, G = 3.3 K/mm, and δ = 50 µm.

No facets are formed in neither of the interphase boundaries of “Rumi” structure. Therefore, the formation of such floating structure can be unlikely related to S/S anisotropy and possibly have dynamical origins. It is suggested that the formation of this structure has thickness-related origins. Figure 6-2 shows the “Rumi” microstructure from top and bottom views. It can be seen the microstructure is 3D as it has a lamellar morphology on top view and “Rumi” structure on bottom view. Even though the phase alternation is deviated from

the ideal periodic ABAC pattern, the eutectic spacing can be approximately measured from the top view. The measured average spacing is 38.4 μm and it is well inside the stability region of the ABAC pattern at V = 0.150 μm/s. As the microstructure scaling at this velocity is less than the sample thickness (>50 μm), it is not surprising that addition of degree of freedom due to the relatively high thickness of the sample leads to formation of a 3D microstructure.

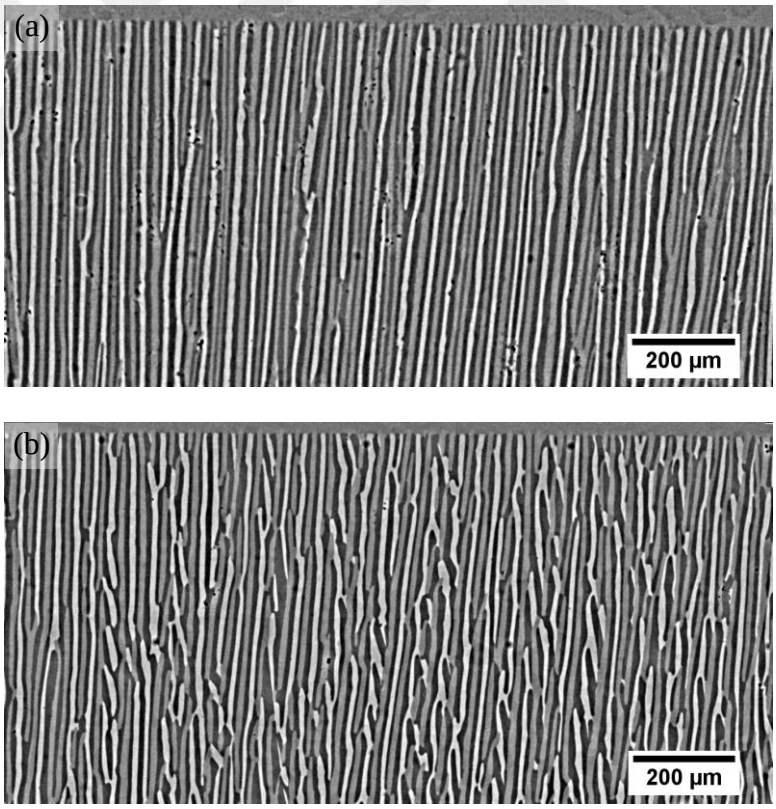

Figure 6-2. 3D microstructure observed in a DS experiment. (a) Top microstructure with lamellar structure. (b) Bottom microstructure with “Rumi” structure. V = 0.150 μm/s, G = 3.3 K/mm, and δ = 50 μm.

6.3.1.2 Asymmetric ABAC pattern

The phase fraction within a eutectic grain growing with local-equilibrium conditions is dictated by the phase diagram of the system and therefore, the width of lamellae in 2D samples are fixed by a global concentration. In the simple phase arrangement such as ABC, the width of each phase is set by the lever rule and is a constant. However, in an arrangement such as ABAC, ABABAC, etc. due to existence of more than three phases in the basic state, the width of the repeated phase, is a variable parameter. In the case of ABAC pattern, therefore, the width of A phases can be different within one motif. In nearly steady-state isotropic ABAC, the width of A phases within one motif is equal. As the width of A phases can be freely chosen by the system, in some experiments, the asymmetric width of the A phases within ABAC arrangements are observed. However, such inequality in the width of the A phases violates the symmetry provided by mirror planes in the middle of B and C phases in one motif. Numerically, it is found that the average undercooling of the symmetric ABAC unit front is lower than that of asymmetric ABAC alternation [57]. Although the asymmetric ABAC pattern still provides the efficient solute redistribution ahead of the front comparing to the other arrangements, it must be less favored than the symmetric ABAC pattern. This can be the reason why, statistically speaking, the number of observed asymmetric ABACs is considerably less than symmetric ones. Figure 6-3 shows an example the asymmetric ABAC microstructure formed during standard DS experiment.

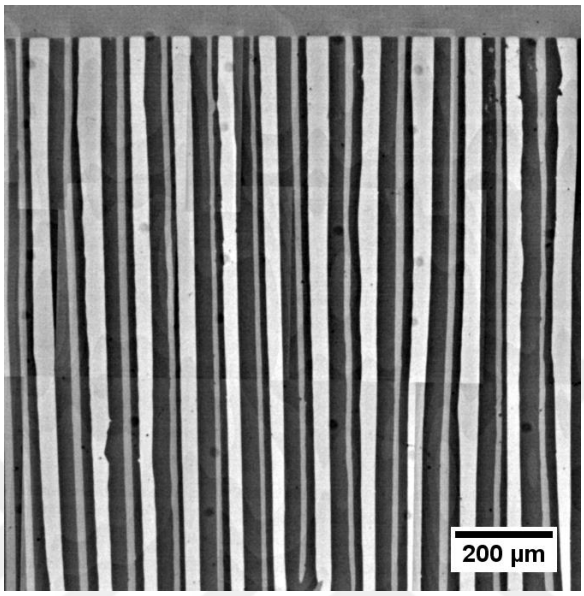

Figure 6-3. Asymmetric ABAC pattern formation during a DS experiment. In this structure, the width of A phases within one motif of ABAC is not equal. V = 0.020 µm/s, G = 3.3 K/mm, and δ = 50 µm.

6.3.1.3 Fragment lamellar structure

Fragment lamellar structure is characterized by the formation of discontinuous lamellae of any of the phases or all of them. Figure 6-4 shows an example of the fragment lamellar structure formed during a DS experiment. Surprisingly, it was observed that the lamellar structure in the bottom view is almost continuous lamellar structure.

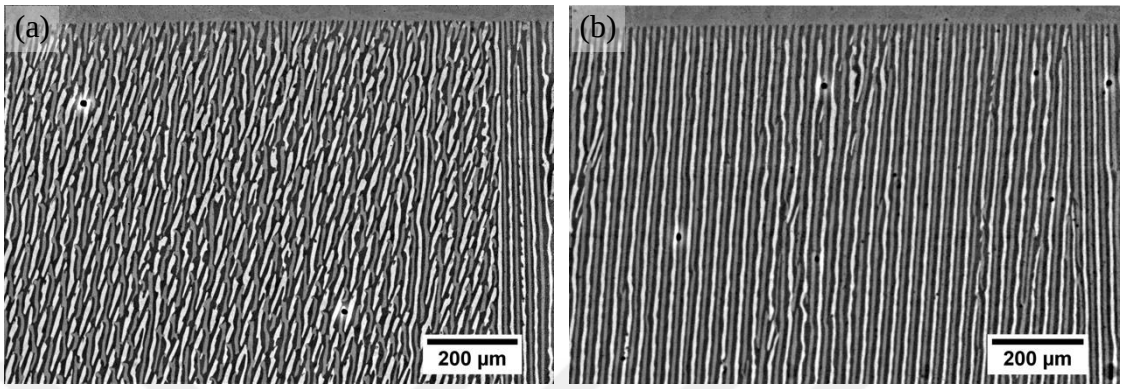

Figure 6-4. Fragment lamellar structure. (a) Top microstructure has discontinuous lamellar structure. (b) Bottom microstructure has almost continuous lamellar morphology. V = 0.250 µm/s, G = 3.3 K/mm, and δ = 50 µm.

Figure 6-5 (a) shows a similar fragment lamellar structure which formed during initial growth before an RDS experiment. The structure was later subjected to rotation to examine the orientation dependency of the microstructure. Figure 6-5 (b) shows the microstructure after 23° rotation of the sample. With the onset of the rotation, the structure immediately turns to isotropic lamellar structure with ABAC pattern. Such an abrupt transition in the structure is unlikely associated with the anisotropy of S/S interphase boundary. As it was discussed in many cases in previous chapters, the microstructural changes as a result of S/S anisotropy have well-defied angular ranges in which the phenomena occur. Therefore, it is suggested that such microstructure formation has dynamical origin and even if there are some sort of S/S anisotropies, it is not the main reason of the fragment lamellar structure formation.

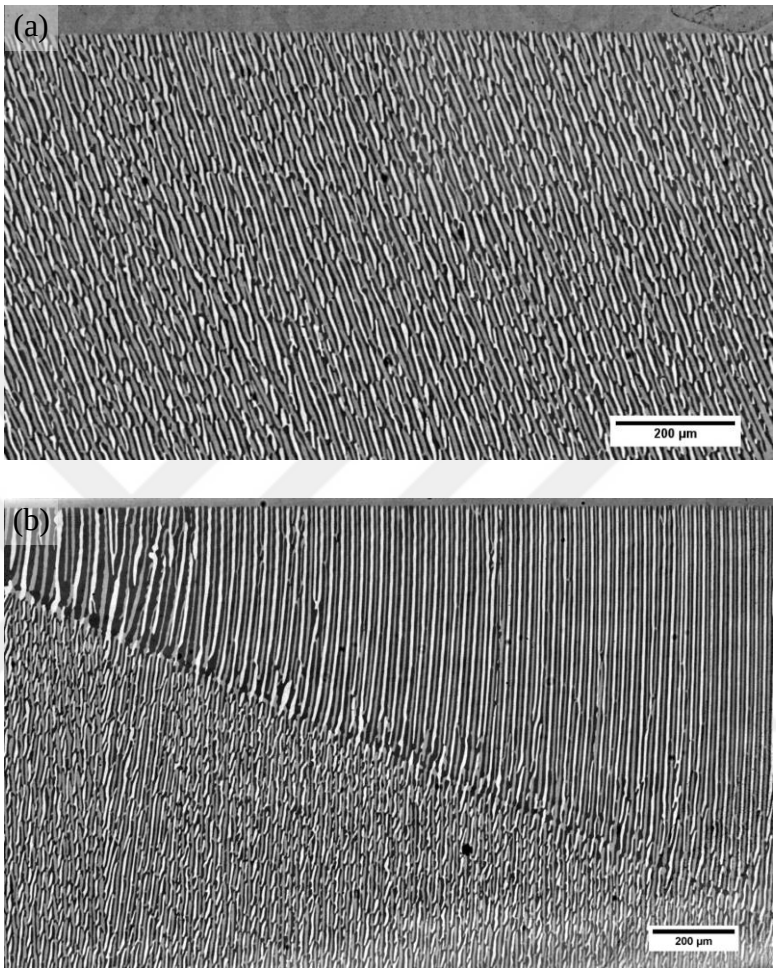

Figure 6-5. Fragment lamellar structure evolution by onset of rotation. (a) The growth of the fragment lamellar structure by directional solidification in the initial stages of an RDS experiment at V = 0.500 µm/s. (b) The rapid evolution of the fragment lamellar to continuous lamellar structure by onset of the rotational motion. CCW, $\omega = 0.013$ º/s, G = 5.1 K/mm, δ = 13 µm.

Figure 6-6 (a) shows another example of the fragment lamellar structure in which only one of the phases, *i.e.* C phase is forming discontinuous lamellar. The microstructure is in

fact is a result of the oscillation of C phase within the thickness of the sample. At a constant growth velocity, the modulation of the eutectic spacing before and after C phase discontinuity in various occasions were measured within 750 µm growth length as shown in Figure 6-6 (a). Figure 6-6 (b) demonstrates the λ-plots of marked positions on the microstructure. Even though before each discontinuity of C phase, the λ-plot contains a minimum, similar to an elimination event, it rapidly relaxes around the minimum positions after the appearance of the phase. Eight measured eutectic spacing values within 750 µm are summarized in Table 6-1. The λ_{mean} does not show significant variation after the events and the measured spacing values stay between 28.62- 29.39 µm, which is inside the stability region ABAC pattern growing V= 0.280 µm/s.

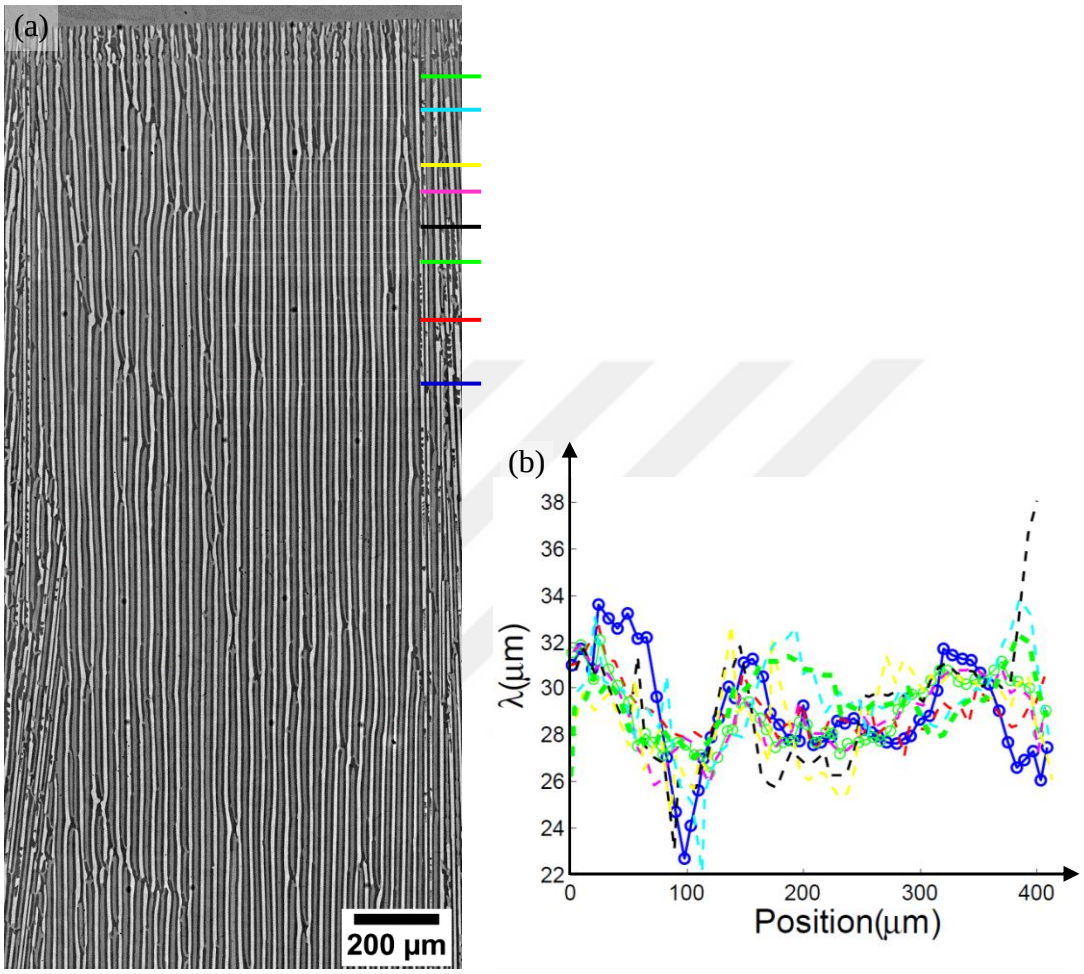

Figure 6-6. Fragment lamellar strucure in which the C phases oscillated within the thickness of the sample. (a) Only C phases have the discontinuous growth dynamics. (b) λ-plots taken from the marked positions on the microstructure. V = 0.280 µm/s, G = 3.3 K/mm, and δ = 100 µm.

Table 6-1. The minimum, maximum, and mean eutectic spacing values corresponding to the marked positions on Figure 6-6.

No	**1**	**2**	**3**	**4**	**5**	**6**	**7**	**8**
λ_{min} (µm)	22.68	27.11	26.39	25.86	23.08	24.66	22.07	26.22
λ_{max} (µm)	33.59	32.96	32.09	31.92	38.07	32.73	33.85	32.32
λ_{mean} (µm)	28.98	29.03	28.91	28.79	29.07	28.62	29.39	29.37
STD (µm)	2.28	1.15	1.44	1.51	2.64	1.92	2.11	1.34

6.3.2 Anisotropy-driven microstructures

The second class of the microstructures in this chapter is anisotropy-driven microstructures. It is suggested that in this category, the determinant factor in the microstructure selection is some sort of anisotropy in the interphase boundary energy.

6.3.2.1 Tilted lamellar structure

In this type of lamellar structure, the interphase boundaries are significantly inclined with respect to the growth direction. Figure 6-7 shows an example of the tilted lamellar structure from top and bottom views, in which the lamellar structure is inclined 10.5° with respect to the overall growth direction. Despite the steep inclination of the structure, the ABAC order is preserved in the microstructure. Other characteristic features include the

phase width difference between the top and bottom structures and facets observed on the AB boundaries

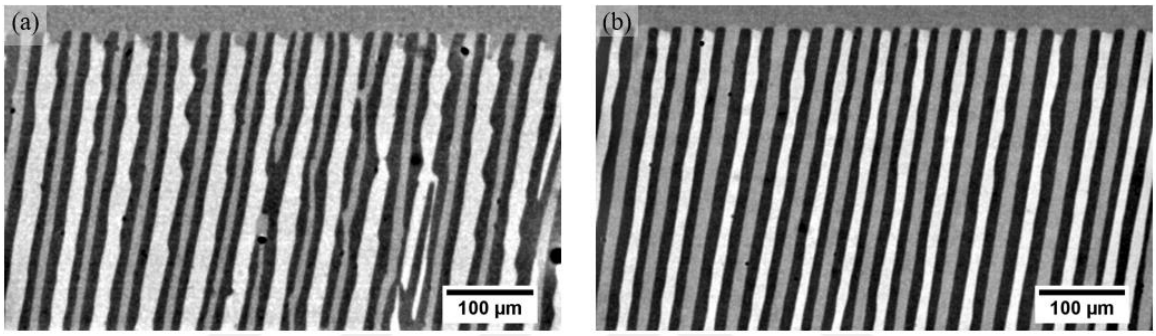

Figure 6-7. A tilted ABAC structure formed during standard DS experiment. (a) Top microstructure. (b) Bottom microstructure. V = 0.140 μm/s, G = 3.3 K/mm, and δ = 50 μm.

To examine the response of the structure to velocity change, the microstructure shown in Figure 6-7 was subjected to a downward velocity jump from 0.18 to 0.140 μm/s. Figure 6-8 shows elimination event occurred as a result of the velocity decrease and the corresponding λ-plot showing a minimum in the spacing at the onset of the elimination.

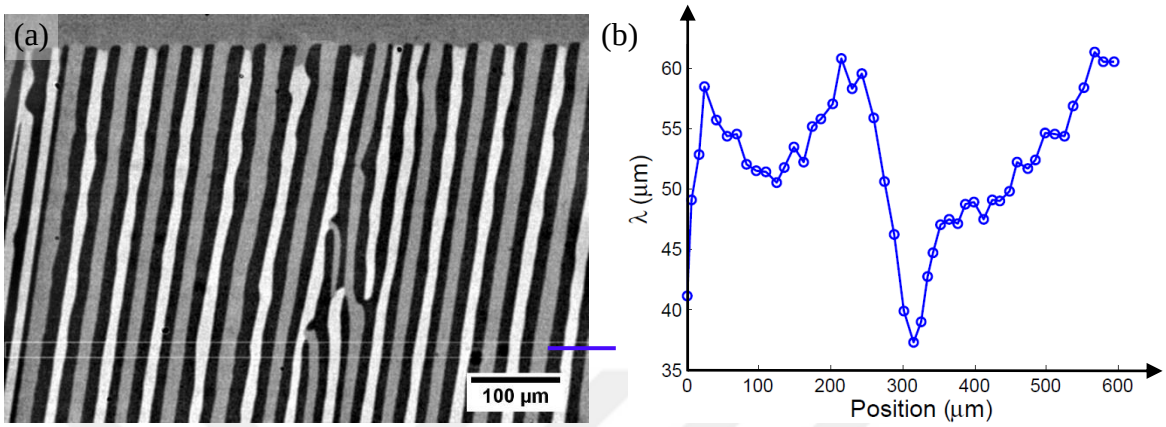

Figure 6-8. Elimination observed during growth of the tilted structure formed during DS experiment. (a) Onset of elimination in the tilted structure as result of a decrease in the velocity. (b) λ-plot taken before the elimination event. The position where the measurement is taken, is marked on the microstructure with the blue solid line. V_i = 0.180, V_f = 0.140 µm/s, G = 3.3 K/mm, and δ = 50 µm.

To examine if the phase-diffusion process is active after elimination, the λ-plots were taken within 2150 µm growth length without any velocity change. Figure 6-9 shows the microstructure after the elimination event along with the corresponding λ-plots.

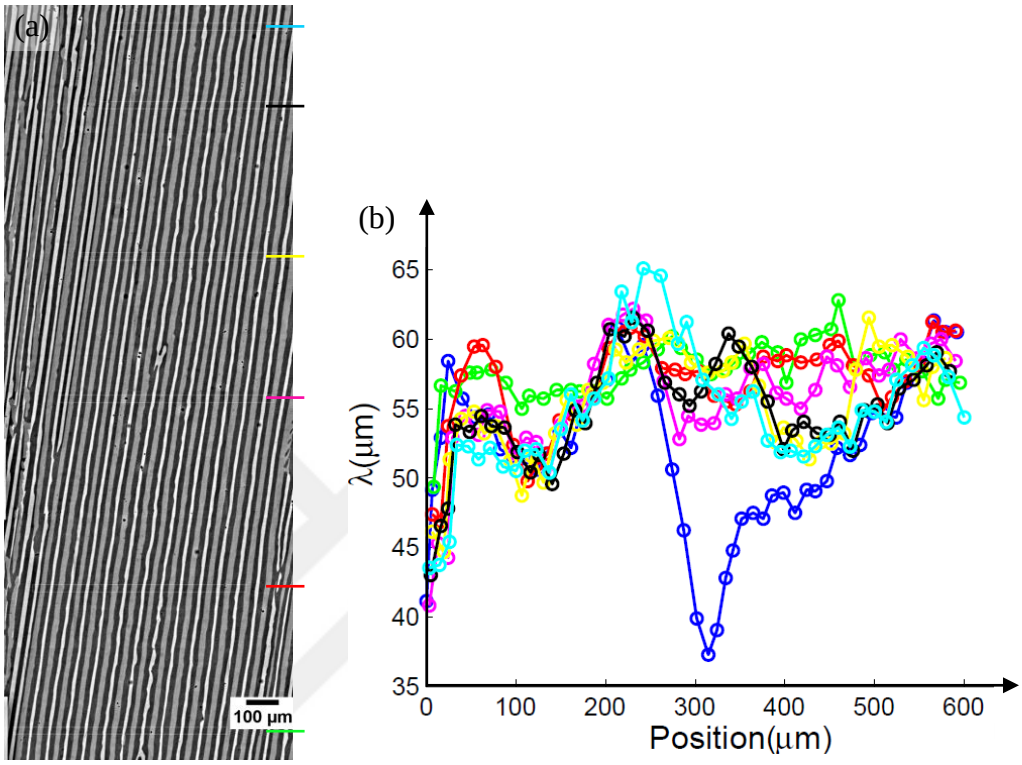

Figure 6-9. Tilted ABAC pattern recovery after elimination shown in Figure 6-10. (a) Tilted structure showing recovery after the elimination during DS. (b) λ-plot from different locations of the microstructure in (a). The blue curve corresponds to the onset of the elimination. V = 0.140 µm/s, G = 3.3 K/mm, and δ = 50 µm

By decreasing velocity from 0.18 to 0.14 µm/s the eutectic spacing shows a minimum at 37.25 µm. This spacing is higher than the elimination threshold of the isotropic ABAC (27.41 µm) at the same velocity. The spacing is rapidly relaxing after the elimination event, shown by the green curve, and subsequently ABAC pattern is recovered. The spacing values do show significant changes afterwards and it is not completely homogenized within the

measured growth length. To sum up, some sort of anisotropy, possibly in AB boundary, is associated with the tilted structure; however, the anisotropy does not totally prevent the spacing adjustment mechanisms and homogenization, even though it is slow. The structure may be analogous to nearly-locked structure discussed in *chapter 4*, in which the lamellae structure is inclined with respect to the overall growth direction; however, the dynamics of the growth are controlled by the phase-diffusion, spacing adjustment, and recovery mechanisms.

6.3.2.2 Brick-like structure

One of the widely studied ternary systems experimentally [100-103] and by phase-field simulation [104] is the Al–Ag–Cu alloy. The most widely observed cross-sectional microstructure of bulk samples in the system is the brick-like structure, shown in Figure 6-11 (a). This microstructure is characterized by the alternation of Ag_2Al and Al_2Cu phases (gray and white), while the black phase (Al) is forming matrix and it goes between the blocks of the two-phase alternation. In the quasi-2D sample of In-Bi-Sn system, a structure analogous to brick-like structure is observed. However, the direction of observation in current study is longitudinal while in Figure 6-11 (b), the direction of observation was cross-sectional.

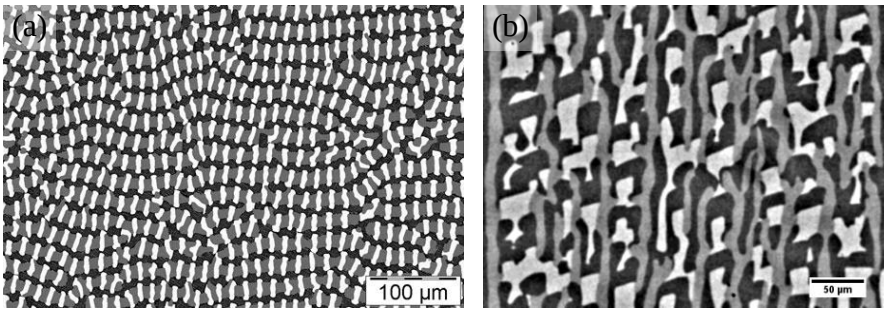

Figure 6-11. Comparison between brick-like structure in Al–Ag–Cu with ternary system In-Bi-Sn. (a) Cross-sectional view of directionally solidified bulk sample of Al–Ag–Cu three-phase system [103]. (b) Longitudinal section of directionally solidified quasi-2D sample of In-Bi-Sn system.

Figure 6-12 shows the early stages of brick-like structure formation. The structure started with very irregular shape of the phases, shown in (a) and (b). By further growth, the structure began to form more regular structure (c) and (d).

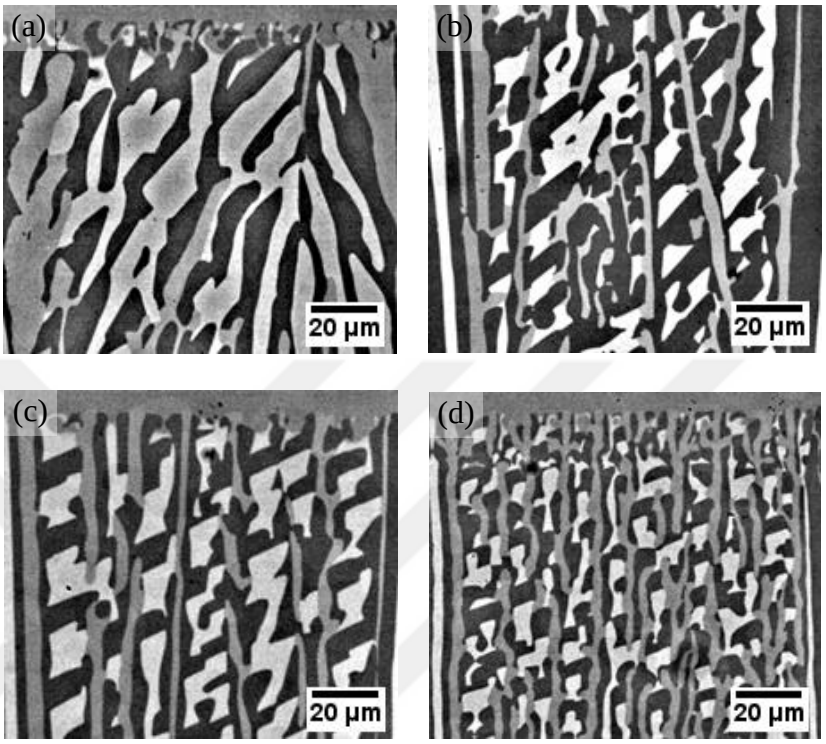

Figure 6-12. Brick-like structure observed during a DS experiment. (a) Initial growth of the brick-like pattern. (b) The microstructure after ~ 4030 µm growth length from funnel. (c) The evolution of the microstructure after ~ 10210 µm growth length. (d) The microstructure after ~ 20260 µm growth length. G = 3.3 K/mm and δ = 50 µm.

Figure 6-13 shows the final brick-like microstructure, in which new morphology of the A and B phases were observed. The microstructure contains relatively thick plates of coupled A and B phases and the third phase, γ-Sn, phase is repeating between the block of two-phase alternation. In Figure 6-13, right next to Brick-like structure, an isotropic grain with ABAC arrangement grows.

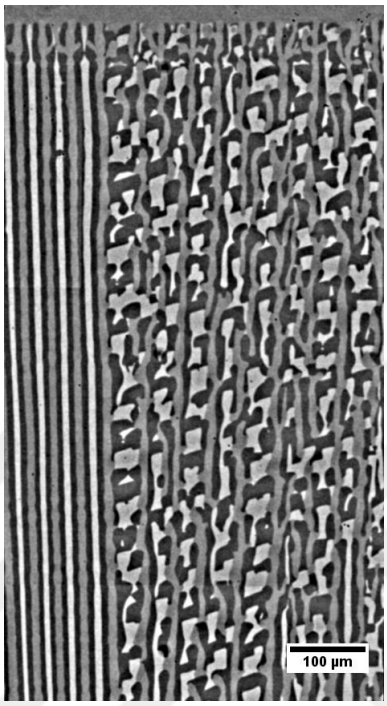

Figure 6-13. Different morphologies of A and B phases observed in brick-like structure. A and B phases were coupled, and C phases keep almost lamellar shape. V = 0.150 µm/s, δ = 50 µm, and G = 3.3 K/mm.

The formation of the brick-like structure is unlikely related to the experimental conditions. Existence of the isotropic grain with ABAC order next to it and its stationary growth despite the velocity jumps within the range of 0.060 - 0.180 µm/s confirm that the microstructure selection is due to the intrinsic properties of the grain. Relatively faceted shapes of B phases on one hand, the floating dynamics of AC boundaries on the other hand leads to the conclusion that the formation of this microstructure most probably is related to

some sort of crystallographic relationship between A and B phases. In other words, it is suggested that anisotropy in the AB interphase boundaries energy resulted in such a unique microstructure.

6.4 Conclusion

In this chapter, beside the regular lamellar ABAC pattern and the characterized anisotropic structures, other microstructures which observed during this study are categorized and their possible origins are discussed. Other microstructures are categorized into two main groups as nearly-isotropic and anisotropy-driven microstructures.

In the class of nearly-isotropic microstructures, it was shown that by increasing sample thickness or in other words, decreasing confinement effect on the growth dynamics, the lamellar structure is not stable anymore and depending on the experimental conditions, different shapes of phases may form. 3D microstructures such as “Rumi” and fragment lamellar structures have thickness-related origins. Dissimilar microstructures on the sides of the sample confirm that the increase in thickness of samples assists the microstructures to gain the additional degree of freedom in growth. This leads to the formation of complicated microstructures rather than regular lamellar microstructures. In the class of nearly-isotropic structure, the asymmetric ABAC pattern is also introduced in which the width of A phases

within an ABAC motif are unequal. It was discussed that formation of asymmetric ABAC may be associated with additional undercooling and therefore it is not favored by the system.

In the second class, the microstructures that are possibly affected by the S/S anisotropy are introduced. Tilted lamellar structure with ABAC alternation is identified where the growth dynamics are still governed by phase-diffusion, spacing adjustment and recovery mechanisms despite the anisotropy in the interphase boundary. The formation of the brick-like of this structure is linked to a particular form of anisotropy of AB boundary while AC boundary most likely is isotropic.

Among many different and complex microstructures that are observed during overall study, the ones that are discussed in this chapter are the more frequent ones. The formation of these microstructures indicates that three-phase eutectics are pattern-rich systems and small changes in the experimental conditions as well as the internal properties of system dramatically alters the microstructure formation.

Outlines of future studies

In this study, the effect of the sample thickness on the stability limits of the ABAC pattern was established. It will be interesting to investigate the pattern formation phenomena in the bulk samples, true 3D geometry. The preliminary studies on the bulk samples within this work showed the formation of lamellar ABAC pattern as well as other microstructures. Some of the results of the bulk samples experiments are given in appendix, however, full characterization of the 3D microstructures remains to investigate in the future.

Using RDS experimental technique, four types of eutectic grains are identified. It is expected that other classes of the grains exist in the three-phase systems, depending on the relative orientations of the phases. further RDS experiments are required to identify other possible eutectic grains in the three-phase systems.

It is well established in this study that each of the interphase boundaries of the systems, *i.e*. AB and AC, can have different properties, depending on how the crystals of the system are oriented. X-ray and electron backscattered diffraction studies would be necessary to identify crystallographic orientation relationships between two neighborhood phases in each eutectic grain. This will be a challenging task since the alloy is sensitive to the air and once the sample alloy is removed from the glasses, it will be oxidized. Also, there is a solid-solid

phase transformation, which leads to the significant changes of the pattern after solidification completion. These two points will result in difficulties in the investigation however, this will be highly valuable if one can perform the crystallographic analyses by overcoming these difficulties.

It is well-known that the microstructures control the properties of materials. It will be highly valuable if one can correlate the microstructures of the three-phase systems established in this study, with the properties. As the alloy is one of the potential materials for soldering, investigating how the mechanical and electrical properties are affected by the different microstructures is critical.

BIBLIOGRAPHY

[1] W. Kurz, D.J. Fisher, Fundamentals of solidification, Trans tech publications (2005).

[2] ASM Handbook, Volume 15 casting, ASM International

[3] H.R. Kotadia, P.D. Howes, S.H. Mannan, A review: On the development of low melting temperature Pb-free solders, Microelectronics Reliability 54(6) (2014) 1253-1273.

[4] S.A. David, S.S. Babu, J.M. Vitek, Welding: Solidification and microstructure, Journal of The Minerals, Metals & Materials Society 55(6) (2003) 14-20.

[5] S.A. David, T. Debroy, Current issue and problems in welding science Science 257(5069) (1992) 497-502.

[6] J.N. DuPont, ASM Handbook, ASM International (2011).

[7] W.E. Frazier, Metal additive manufacturing: A Review, Journal of Materials Engineering and Performance 23(6) (2014) 1917-1928.

[8] L.A. Tarshis, J.L. Walker, M.F.X. Gigliotti, Solidification, Annual Review of Materials Science 2 (1972) 181-216.

[9] M.E. Glicksman, Principles of solidification, pringer Science+Business Media (2011).

[10] R. Trivedi, W. Kurz, Microstructure selection in eutectic alloys systems, Solidification processing of eutectic alloys (1988).

[11] W.C. Winegard, S. Majka, B.M. Thall, B. Chalmers, Eutectic Solidification In Metals, Canadian Journal Of Chemistry-Revue Canadienne De Chimie 29(4) (1951) 320.

[12] J.A. Dantzing, M. Rappaz, Solidification, EPFL Press (2009).

[13] R. Trivedi, J.T. Mason, J.D. Verhoeven, W. Kurz, Eutectic spacing selection in lead-based alloy systems, Metallurgical Transactions A 22A (1991) 2523-2533.

[14] H.E. Cline, Directionally solidified thin-film eutectic alloys, Journal of Applied Physics 52(1) (1981) 256-260.

[15] R.M. Jordan, J.D. Hunt, The growth of lamellar eutectic etructures in the Pb-Sn and Al-$CuAl_2$ eystems, Metallurgical and Materials Transactions B 2 (1971) 3401.

[16] E.G. Çadırlı, M., Directional Solidification of the Aluminium-Copper Eutectic Alloy, Journal of Materials Processing Technology 97 (2000) 74–81.

[17] E.K. Cadirli, H.; Gunduz, M., Effect of growth rates and temperature gradients on the lamellar spacing and the undercooling in the directionally solidified Pb–Cd eutectic alloy, Materials Research Bulletin 38 (2003) 1457-1476.

[18] H.C. Kaya, E.; Gunduz, M., Effect of growth rates and temperature gradients on the spacing and undercooling in the broken-Llamellar eutectic growth (Sn-Zn eutectic system), Journal of Materials Engineering and Performance 12(4) (2003) 456-469.

[19] S. Akamatsu, S. Bottin-Rousseau, G. Faivre, Determination of the Jackson-Hunt constants of the In-In2Bi eutectic alloy based on in situ observation of its solidification dynamics, Acta Materialia 59(20) (2011) 7586-7591.

[20] S. Akamatsu, S. Bottin-Rousseau, M. Perrut, G. Faivre, V.T. Witusiewicz, L. Sturz, Real-time study of thin and bulk eutectic growth in succinonitrile–(d)camphor alloys, Journal of Crystal Growth 299(2) (2007) 418-428.

[21] L. Sturz, V.T. Witusiewicz, U. Hecht, S. Rex, Organic alloy systems suitable for the investigation of regular binary and ternary eutectic growth, Journal of Crystal Growth 270 (2004) 273-282.

[22] S. Bottin-Rousseau, M. Perrut, C. Picard, S. Akamatsu, G. Faivre, An experimental method for the in situ observation of eutectic growth patterns in bulk samples of transparent alloys, Journal of Crystal Growth 306(2) (2007) 465-472.

[23] V.T. Witusiewicz, U. Hecht, S. Rex, Top-view approach for in-situ observation of growth morphology in bulk transparent organic alloys, Journal of Crystal Growth 353(1) (2012) 17-24.

[24] A. Karma, A. Sarkissian, Morphological instabilities of lamellar eutectics, Metallurgical and Materials Transactions A 27(3) (1996) 635-656.

[25] J.D. Hunt, D.T.J. Hurle, The structures of faceted/nonfaceted eutectics, Transactions of the Metallurgical Society of AIME 242 (1968) 1043.

[26] J. Liu, R. Elliott, Irregular eutectic solidification, Materials Science and Engineering: A 173(1–2) (1993) 129-132.

[27] P. Magnin, J.T. Mason, R. Trivedi, Growth of irregular eutectics and the Al-Si system, Acta Metallurgica Materialia 39(4) (1991) 469-480.

[28] R.E. Napolitano, H. Meco, C. Jung, Faceted solidification morphologies in low-growth-rate Al-Si eutectics, Journal of The Minerals, Metals & Materials Society 56(4) (2004) 16-21.

[29] H. Jones, W. Kurz, Relation of interphase spacing and growth temperature to growth velocity in Fe-C And Fe-Fe_3C eutectic alloys, Zeitschrift Fur Metallkunde 72(11) (1981) 792-797.

[30] H. Jones, W. Kurz, Growth temperatures and the limits of coupled growth in unidirectional solidification of Fe-C eutectic alloys, Metallurgical Transactions A-Physical Metallurgy And Materials Science 11(8) (1980) 1265-1273.

[31] D.J. Chakrabarti, D.E. Laughlin, The B−Cu (Boron−Copper) system, Bulletin of Alloy Phase Diagrams 3(1) (1982) 45-48.

[32] A.J. Perry, A.R. Nicoll, K. Phillips, P.R. Sahm, The copper-boron eutectic-unidirectionally solidified, Journal of Materials Science 8(9) (1973) 1340-1348.

[33] D.J. Fisher, W. Kurz, A Theory of branching limited gorwth of irregular eutectics, Acta Metallurgica 28 (1980) 777-794.

[34] V.T. Witusiewicz, L. Sturz, U. Hecht, S. Rex, Thermodynamic description and unidirectional solidification of eutectic organic alloys: IV. Binary systems neopentylglycol–succinonitrile and amino-methyl-propanediol–succinonitrile, Acta Materialia 53(1) (2005) 173-183.

[35] M.-J. Suk, K. Leonartz, Halo growth during unidirectional solidification of camphor-naphthalene eutectic system, Journal of Crystal Growth (2000) 141-149.

[36] M.-J. Suk, K. Leonartz, Discontinuous growth of primary naphthalene plate in camphor-naphthalene eutectic system, Journal of Crystal Growth (2006) 809-812.

[37] S. Akamatsu, S. Bottin-Rousseau, G. Faivre, Stability of lamellar eutectic growth in thick samples, Philosophical Magazine 86(24) (2006) 3703-3715.

[38] S. Liu, J.H. Lee, R. Trivedi, Dynamic effects in the lamellar–rod eutectic transition, Acta Materialia 59(8) (2011) 3102-3115.

[39] K.A. Jackson, J.D. Hunt, Lamellar and rod eutectic growth, Transactions of the Metallurgical Society of AIME. 236(8) (1966) 1129-1142.

[40] H.E. Cline, Formation Of Faults In Eutectic Alloys, Transactions Of The Metallurgical Society Of AIME. 245(10) (1969) 2205.

[41] J.S. Langer, Eutectic solidification and marginal stability, Physical Review Letters 44(15) (1980) 1023.

[42] M. Asta, C. Beckermann, A. Karma, W. Kurz, R. Napolitano, M. Plapp, G. Purdy, M. Rappaz, R. Trivedi, Solidification microstructures and solid-state parallels: Recent developments, future directions, Acta Materialia 57(4) (2009) 941-971.

[43] M. Zimmermann, A. Karma, M. Carrard, Oscillatory lamellar microstructure in off-eutectic Al-Cu alloys, Physical Review B 42(1) (1990) 833.

[44] M. Ginibre, S. Akamatsu, G. Faivre, Experimental determination of the stability diagram of a lamellar eutectic growth front, Physical Review 56(1) (1997) 780.

[45] S. Akamatsu, S. Moulinet, G. Faivre, The formation of lamellar-eutectic grains in thin samples, Metallurgical and Materials Transactions A 32A (2001) 2039-2048.

[46] S. Akamatsu, M. Plapp, G. Faivre, A. Karma, Overstability of lamellar eutectic growth below the minimum-undercooling spacing, Metallurgical and Materials Transactions 35A (2004) 1815-1828.

[47] G. Faivre, Morphological instabilities of lamellar eutectic growth fronts: a survey of recent experimental and numerical results, Journal of Crystal Growth 166(1) (1996) 29-39.

[48] A. Karma, M. Plapp, New insights into the morphological stability of eutectic and peritectic coupled growth, The Journal of The Minerals, Metals & Materials Society 56(4) (2004) 28-32.

[49] S. Akamatsu, M. Plapp, G. Faivre, A. Karma, Pattern stability and trijunction motion in eutectic solidification, Physical Review E 66 (2002) 030501.

[50] A.N. Choudhury, Quantitative phase-field model for phase transformations in multi-component alloys, KIT Scientific Publishing (2012).

[51] A.A. Wheeler, G.B. McFadden, W.J. Boettinger, Phase-field model for solidification of a eutectic alloy, The Royal Society's physical sciences research journal 452(1946) (1996) 495-525.

[52] A. Karma, Phase-field model of eutectic growth, Physical Review E 49(3) (1994) 2245-2250.

[53] H. Xing, X. Dong, H. Wu, G. Hao, J. Wang, C. Chen, K. Jin, Degenerate seaweed to tilted dendrite transition and their growth dynamics in directional solidification of non-axially oriented crystals: a phase-field study, Scientific Reports 6 (2016) 26625.

[54] M. Serefoglu, R.E. Napolitano, M. Plapp, Phase-field investigation of rod eutectic morphologies under geometrical confinement, Physical Review E 84(1) (2011) 011614.

[55] M. Serefoglu, Pattern selection dynamics in rod eutectics, Materials Science and Engineering, Iowa State University, Ames, Iowa, 2009.

[56] A. Choudhury, Pattern formation during self-organization in three-phase eutectic solidification, Transactions of the Indian Institute of Metals 68(6) (2015) 1137-1143.

[57] A. Choudhury, M. Plapp, B. Nestler, Theoretical and numerical study of lamellar eutectic three-phase growth in ternary alloys, Physical Review E 83(5) (2011) 051608.

[58] T. Pusztai, L. Rátkai, A. Szállás, L. Gránásy, Spiraling eutectic dendrites, Physical Review E 87(3) (2013) 032401.

[59] S. Akamatsu, M. Perrut, S. Bottin-Rousseau, G. Faivre, Spiral two-phase dendrites, Physical Review Letter 104(5) (2010) 056101.

[60] P. Ball, Pattern Formation in Nature: Physical Constraints and Self-Organising Characteristics, Architectural Design 82(2) (2012) 22-27.

[61] J.P. Gollub, J.S. Langer, Pattern formation in nonequilibrium physics, Reviews of Modern Physics 71(2) (1999) S396-S403.

[62] U. Hecht, L. Granasy, T. Pusztai, B. Bottger, M. Apel, V. Witusiewicz, L. Ratke, J. De Wilde, L. Froyen, D. Camel, B. Drevet, G. Faivre, S.G. Fries, B. Legendre, S. Rex, Multiphase solidification in multicomponent alloys, Materials Science and Engineering: R: Reports 46(1-2) (2004) 1-49.

[63] D.G. Mccartney, J.D. Hunt, R.M. Jordan, The structures expected in a simple ternary eutectic system .1. theory, Metallurgical Transactions a-Physical Metallurgy and Materials Science 11(8) (1980) 1243-1249.

[64] S. Akamatsu, M. Plapp, Eutectic and peritectic solidification patterns, Current Opinion in Solid State and Materials Science (2015) 46-54.

[65] W.J. Boettinger, Surface relief cinemicrography of the unsteady solidification of the Lead-Tin-Cadmium ternary eutectic, Material Science, The Johns Hopkins University, 1972.

[66] J.D. Holder, B.F. Oliver, The directional solidification of Pb-Sn-Cd alloys, Metallurgical Transactions 5(11) (1974) 2423-2437.

[67] V.T. Witusiewicz, L. Sturz, U. Hecht, S. Rex, Phase equilibria and eutectic growth in quaternary organic alloys amino-methyl-propanediol-(D)camphor-neopentylglycol-succinonitrile (AMPD-DC-NPG-SCN), Journal of Crystal Growth 297(1) (2006) 117-132.

[68] M.A. Ruggiero, J.W. Rutter, Origin of microstructure in the 332 K eutectic of the Bi-In-Sn system, Materials Science and Technology 13(1) (1997) 5-11.

[69] V.T. Witusiewicz, U. Hecht, S. Rex, M. Apel, In situ observation of microstructure evolution in low-melting Bi-In-Sn alloys by light microscopy, Acta Materialia 53(13) (2005) 3663-3669.

[70] S. Bottin-Rousseau, M. Şerefoğlu, S. Yücetürk, G. Faivre, S. Akamatsu, Stability of three-phase ternary-eutectic growth patterns in thin sample, Acta Materialia 109 (2016) 259-266.

[71] E.E.M. Noor, N.M. Sharif, C.K. Yew, T. Ariga, A.B. Ismail, Z. Hussain, Wettability and strength of In–Bi–Sn lead-free solder alloy on copper substrate, Journal of Alloys and Compounds 507(1) (2010) 290-296.

[72] P.W. Bridgman, The compressibility of thirty metals as a function of pressure and temperature, Proceedings of the American Academy of Arts and Sciences 58 (1923) 165.

[73] W.N. Klaus-Werner Benz, Introduction to crystal growth and characterization, Wiley-VCH2014.

[74] S. Yücetürk, Solidification dynamics of three-phased eutectic patterns in 2D, Mechanical Engineering, Koc University, 2015.

[75] S. Akamatsu, S. Bottin-Rousseau, M. Serefoglu, G. Faivre, A theory of thin lamellar eutectic growth with anisotropic interphase boundaries, Acta Materialia 60(6-7) (2012) 3199-3205.

[76] S. Bottin-Rousseau, M. Serefoglu, S. Akamatsu, G. Faivre, Iop, The surface tension force of anisotropic interphase boundaries is perpendicular to the solidification front during eutectic growth, IOP Conference Series: Materials Science and Engineering (2012).

[77] S. Akamatsu, S. Bottin-Rousseau, M. Şerefoğlu, G. Faivre, Lamellar eutectic growth with anisotropic interphase boundaries: Experimental study using the rotating directional solidification method, Acta Materialia 60(6–7) (2012) 3206-3214.

[78] R.E. Napolitano, M. Serefoglu, Control and Interpretation of Finite-Size Effects and Initial Morphology in Directional Solidification of a Rod-Type Eutectic Transparent Metal-Analog, The Journal of The Minerals, Metals & Materials Society 64(1) (2012) 68-75.

[79] M. Serefoglu, R.E. Napolitano, On the role of initial conditions in the selection of eutectic onset mechanisms in directional growth, Acta Materialia 59(3) (2011) 1048-1057.

[80] D.P. Woodruff, How does your crystal grow? A commentary on Burton, Cabrera and Frank (1951) 'The growth of crystals and the equilibrium structure of their surfaces', Philosophical transactions. Series A, Mathematical, physical, and engineering sciences 373(2039) (2015) 20140230.

[81] D. Turnbull, J.C. Fisher, Rate of Nucleation in Condensed Systems, The Journal of Chemical Physics 17(1) (1949) 71-73.

[82] M. Gunduz, J.D. Hunt, The Measurement of Solid-Liquid Surface Energies in the Al-Cu, Al-Si and Pb-Sn Systems, Acta Metallurgica 33(9) (1985) 1651-1672.

[83] R.J. Schaefer, M.E. Glicksman, J.D. Ayers, High-confidence measurement of solid/liquid surface energy in a pure material, The Philosophical Magazine: A Journal of Theoretical Experimental and Applied Physics 32(4) (1975) 725-743.

[84] M. Muschol, D. Liu, H.Z. Cummins, Surface-tension-anisotropy measurements of succinonitrile and pivalic acid: Comparison with microscopic solvability theory, Physical Review A 46(2) (1992) 1038-1050.

[85] S. Liu, R.E. Napolitano, R. Trivedi, Measurement of anisotropy of crystal-melt interfacial energy for a binary Al-Cu alloy, Acta Materialia 49(20) (2001) 4271-4276.

[86] J.J. Eggleston, G.B. McFadden, P.W. Voorhees, A phase-field model for highly anisotropic interfacial energy, Physica D: Nonlinear Phenomena 150(1–2) (2001) 91-103.

[87] B. Caroli, C. Caroli, G. Faivre, J. Mergy, Lamellar eutectic rowth of CBr4-C2Cl6: effect of crystal anisotropy on lamellar orientations and wavelength dispersion, Journal of Crystal Growth 118 (1992) 135-150.

[88] S. Akamatsu, H. Nguyen-Thi, In situ observation of solidification patterns in diffusive conditions, Acta Materialia 108 (2016) 325-346.

[89] S. Ghosh, A. Choudhury, M. Plapp, S. Bottin-Rousseau, G. Faivre, S. Akamatsu, Interphase anisotropy effects on lamellar eutectics: a numerical study, Physical Review E 91(2) (2015) 022407.

[90] S. Ghosh, Effect of solid-solid boundary anisotropy on directional solidification microstrutures, Department of Physics, Universite Paris Saclay, 2015, p. 127.

[91] S. Akamatsu, M. Plapp, G. Faivre, A. Karma, Overstability of lamellar eutectic growth below the minimum-undercooling spacing, Metallurgical and Materials Transactions A35A (2004) 1815-1828.

[92] T. Einstein, Equilibrium shape of crystals, in: T. Nishinaga (Ed.), Handbook of crystal growth, Fundamentals: thermodynamics and kinetics, Elsevier, UK, 2015.

[93] C. Herring, Some theorems on the free energies of crystal surfaces, Physical Review 82(1) (1951) 87-93.

[94] D. Hoffman, J.W. Cahn, A Vector thermodynamics for anisotropic surfaces I. fundamentals and applications to plane surface junctions, Surface Science 31 (1972) 368-388.

[95] M.E.Glicksman, Principle of solidification, Springer science +business media (2011).

[96] S. Akamatsu, G. Faivre, T. Ihle, Symmetry-broken double fingers and seaweed patterns in thin-film directional solidification of a nonfaceted cubic-crystal, Physical Review E 51(5) (1995) 4751-4773.

[97] R.E. Napolitano, S. Liu, Three-dimensional crystal melt Wulff-shape and interfacial stiffness in the Al-Sn binary system, Physical Review B 70 (2004) 214103-1-214103-11.

[98] B. Utter, E. Bodenschatz, Dynamics of low anisotropy morphologies in directional solidification, Physical Review E 66(5) (2002) 051604.

[99] D. Chatain, Anisotropy of wetting, Annual Review of Materials Research 38(1) (2008) 45-70.

[100] J. Wilde De, L. Froyen, S. Rex, Coupled two-phase [a(Al)+h(Al2Cu)] planar growth and destabilisation along the univariant eutectic reaction in Al–Cu–Ag alloys, Scripta Materialia 51 (2004) 533-538.

[101] U. Hecht, V.T. Witusiewicz, A. Drevermann, S. Rex, O rientation relationship in univariant Al-Cu-Ag eutectics, Transactions of the Indian Institute of Metals, 2005, p. 545.

[102] A.L. Genau, L. Ratke, Crystal orientation and morphology in Al-Ag-Cu ternary eutectic, IOP Conference Series: Materials Science and Engineering 27 (2012).

[103] A. Dennstedt, L. Ratke, Microstructures of Directionally Solidified Al–Ag–Cu Ternary Eutectics, Transactions of the Indian Institute of Metals 65(6) (2012) 777-782.

[104] A. Choudhury, Y.C. Yabansu, S.R. Kalidindi, A. Dennstedt, Quantification and classification of microstructures in ternary eutectic alloys using 2-point spatial correlations and principal component analyses, Acta Materialia 110(Supplement C) (2016) 131-141.

Appendix

Appendix I

Glass Cleaning Procedure

The glasses were put inside the rack, Figure 1, and then all together was inserted inside the beaker containing acetone and it was put inside ultrasonic machine. The duration of ultrasonic cleaning process inside acetone should be at least 20 min. The rack was removed from acetone and rinsed with distilled water. In the next step, the beaker was filled with distilled water (1000 ml) + cleaning detergent (30 gr dishwasher detergent) and the rack was put inside it. The duration of the cleaning in ultrasonic in this step should be at least 15 min and the temperature of the ultrasonic machine was set 50°C. Subsequently, the rack and the glasses inside should be completely rinsed with distilled water. After washing the beaker, it was filled with distilled water and the rack was put inside the beaker. The duration of cleaning process in ultrasonic cleaning in this step should be at least 30 min. Later, the rack containing glasses was cleaned with methanol for 10 min in ultrasonic machine. Then, it was removed from the beaker and dried in an oven at 90°C for couple hours. The rack containing glasses should be stored in desiccator.

Appendix

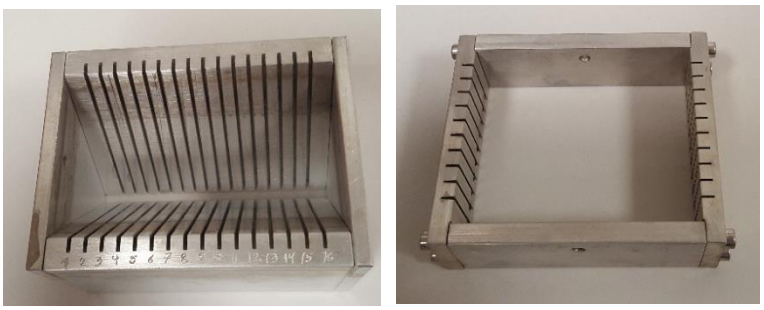

Figure 1. The racks used for washing circular and rectangular glasses.

Appendix II

Alloy Preparation

Alloy at eutectic composition was prepared from elemental Indium, Bismuth and Tin, (Alfa Aesar with 99.999 purity level), shown in Figure 2. The used composition is given in Table 1.

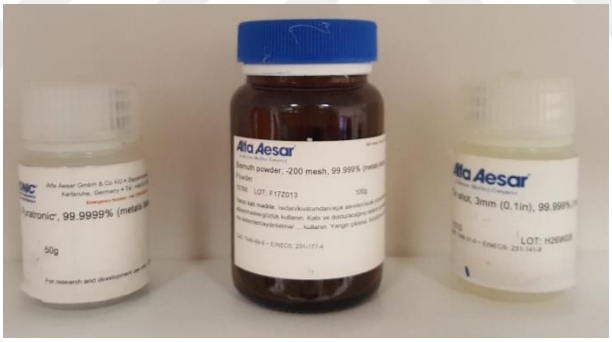

Figure 2. Elemental Indium, Bismuth and Tin

Table 1. The composition used for alloy preparation in this study.

Parameter	In	Bi	Sn	Total
composition (wt %)	51.1836	31.9898	16.8266	100.00

The elements were weighted in an accurate balance in KUTEM. The mixture was put inside the glass crucible and placed inside the container, shown in Figure 4. The container is connected to the vacuum/Argon line. The melting process must be done either under vacuum or Argon atmosphere. The highest melting temperature belongs to Bi with 271°C. Therefore, the temperature of heater was set about 300°C to make sure Bi powder got melted. Depending on the amount of the alloy preparation, the time needed to make a homogenous alloy may change. Higher amount will need longer time. For the used alloy, about 3 hours was considered to get a homogenized alloy. It should be mentioned that the stirring during alloy preparation is critical and the stirrer should be on when elements melt. The appearance of the alloy may indicate if it is homogenized or not. Bi element, which is a black powder, can be seen in the alloy if the alloy is not properly homogenized.

Appendix III

Sample Filling Procedure

The sample consists of two glasses, which were properly cleaned as explained in appendix I, separated by Mylar spacer with the desired thickness. After putting Mylar spacer, which was cut in the required shape, between two glasses, three edges of the sample were closed using UV-cured adhesive, shown in Figure 3. One edge was kept open in order to fill the liquid metal inside the cavity.

Figure 3. Optical adhesive used for gluing the samples. The glue is curried by UV-machine.

The sample was fastened to the clamp attached to the cap of the container. The alloy crucible was put inside the container and the cap was fastened by a clamp. The setup was evacuated and purged by vacuum pump and Argon pressure three times in order to make sure there is

not dirt in the system. The vacuum level is at least 0.03 mbar and the pressure of Argon was kept at 1 Bar. The temperature of the heater is about 120-180°C. When the alloy is completely melted under vacuum, the stirring was started at 100-200 rpm for at least 30 min to ensure whole alloy is melted and homogenized. Then stirring was stopped and sample was gently inserted inside the melt. It is suggested while entering the sample inside the melt, first the possible slag on the surface of the melt was swept by the edge of the glasses and then whole sample was inserted inside melt. Sometimes it might need that the container was slightly heated up using a gun. When the vacuum level stayed stable around the 0.03 mbar, Argon was purged into the system. The pressure provided by Argon leaded to filling the molten alloy inside the cavity of the sample. If the sample was successfully filled, the heater was turn off and the sample was cooled down using air pressure. When the temperature of the container wall reached to about 50°C, the sample could be slowly removed from molten metal. The time of removing sample from the molten metal is critical because if the alloy is so hot, the sample will get empty of the alloy while removing from the molten metal. On the other hand, if the temperature drops too much, the molten metal will start to solidify and stick to the glasses. The procedure is needed to be repeated couple times for the samples that are not filled in the first trail. After successful filling, the sample was removed from the filling setup and the open edge of the sample was closed by the glue.

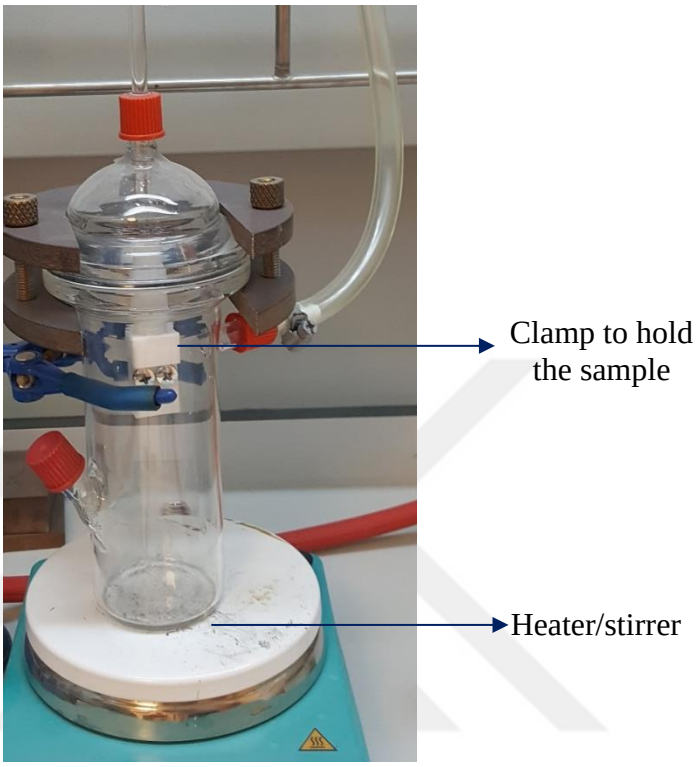

Figure 4. The container and heater/stirrer machine.

Figure 5. The sample filling setup, vacuum pump, and Argon line.

Appendix IV

Double-Sided Microscope

The used microscope system is a combination of an inverted and an upright microscopes (Leica), Figure 7, the lenses of those can be aligned such that they see the same region of interest. The alignment can be done with two screws of top microscope, shown in Figure 6.

Figure 6. Two screws of the top microscope used for alignment of the image with the bottom microscope.

The double-sided microscope has a motorized stage, Figure 8, which enables the motion of the stage in two directions. This function enables getting the images of whole sample to reconstruct panorama images.

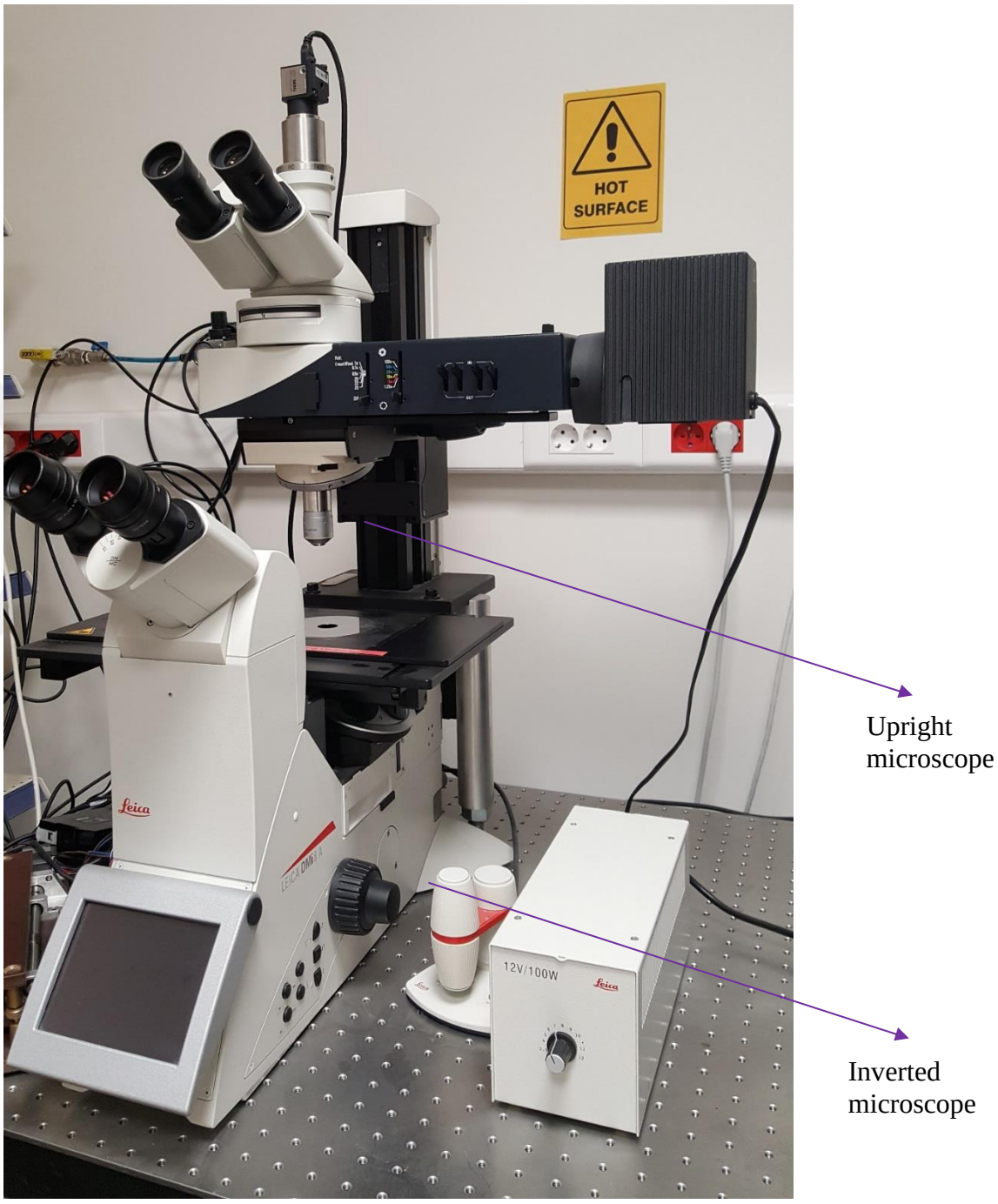

Figure 7. The double-sided microscope.

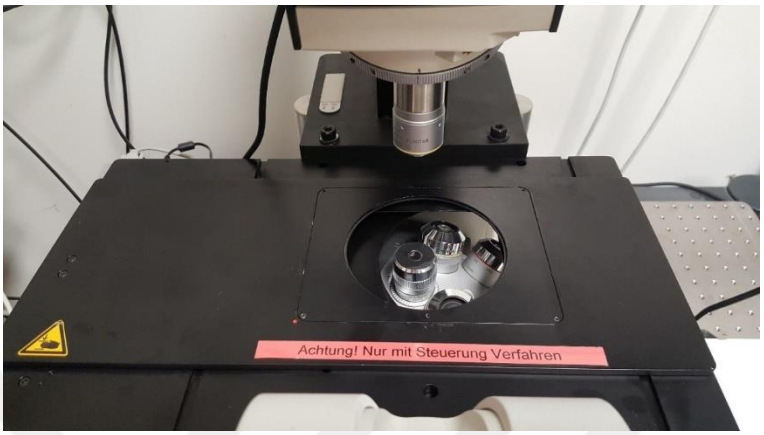

Figure 8. The motorized stage of the double-sided microscope.

Appendix V

Directional Solidification Setup (DS)

The sample was fixed inside the sample holder, shown in Figure 9. The sample holder was fixed inside the DS setup, shown in Figure 10. Through the metallic connector, the sample holder is attached to the motor of DS setup.

Figure 9. The sample holder of the DS experiment setup.

DS setup consists of a hot zone, heated by the thin resistance heaters (OMEGALUX), and a cold zone, cooled by water circulation.

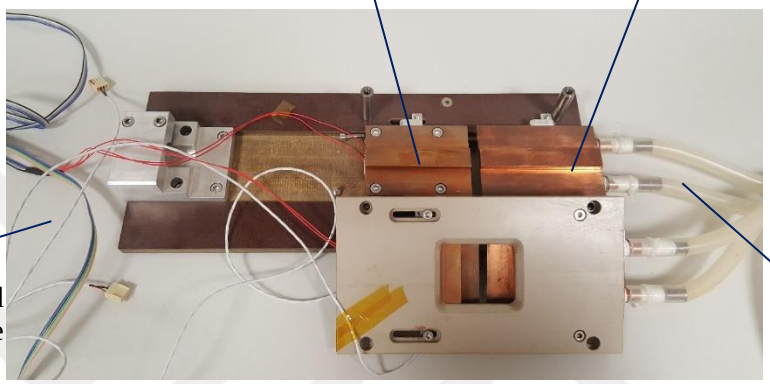

Figure 10. DS setup.

Appendix VII

Rotating Directional Solidification Setup (RDS)

The sample was fixed inside the sample holder, shown in Figure 11. Circular samples can seat in the gap of the holder. Rectangular sample can be stuck to the holder by tape.

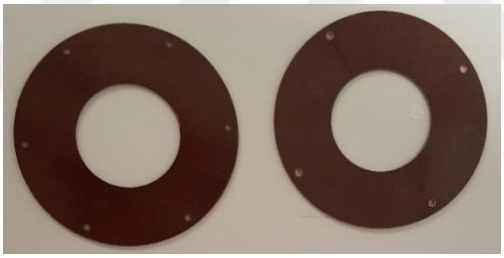

Figure 11. The sample holder of the RDS experiment setup.

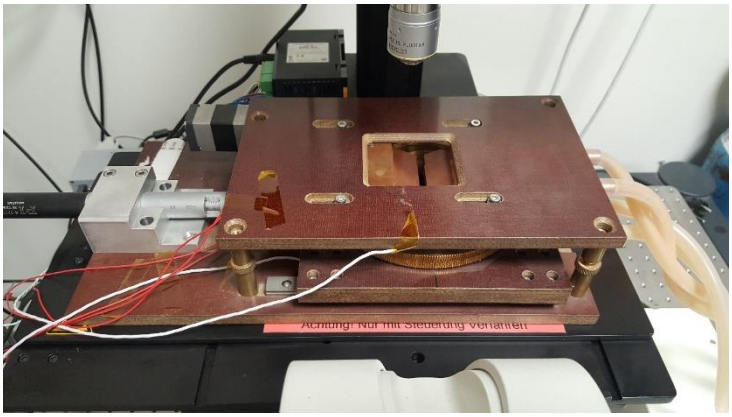

Figure 12. RDS setup mounted on double-sided microscope.

Similar to DS setup, RDS setup consists of a hot zone, heated by the thin resistance heaters, and a cold zone, cooled by water circulation. In addition to DS motor, it has another motor to enable rotational motion. RDS motor rotates a gear via a connecting rod. The sample holder is seated and fixed inside the gear.

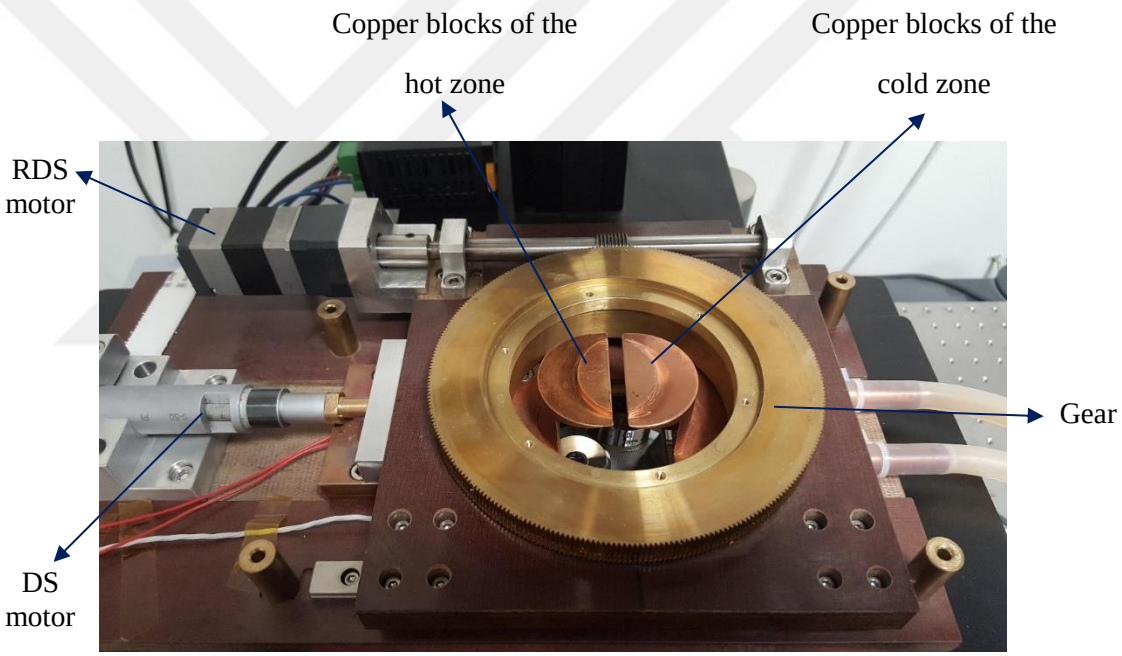

Figure 13. RDS setup configuration.

Appendix VIII

Thermal gradient measurements

Thermal gradient measurements of DS setup

Two K-type thermocouples were fixed in the sample and the molten metal with the same alloy composition was poured inside the cavity provided, Figure 14. The sample is fixed inside DS setup and the thermocouple is connected to temperature reader. The temperature of hot block was to 98°C and the temperature of cold block was 28°C (the temperatures were used through DS experiments). The gap between zone is 5 mm. The thermal gradient measurement was performed for three velocities: 0.1, 0.25 and 0.4 μm/s. The start position of the motor was read from the software and the values of the temperature was recorded by datalogger. Typical temperature versus position curve is shown in Figure 15.

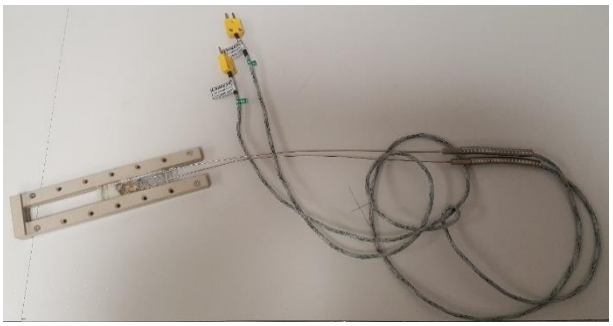

Figure 14. The sample used for thermal gradient measurements in DS setup.

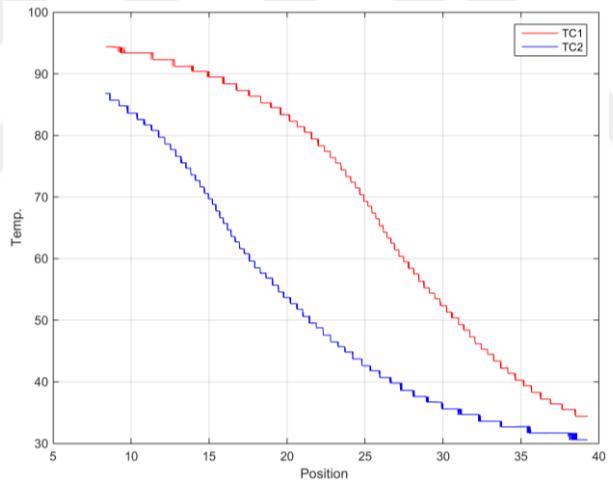

Figure 15. Thermal field at 5 mm Gap at V = 0.1 µm/s

One can do linear fitting at the range close to the eutectic temperature of the alloy, 59.2°C and get the average of the thermal gradients at different velocities.

Thermal gradient measurement of RDS setup

One K-type thermocouples was fixed in the sample and the molten metal with the same alloy composition was poured inside the cavity provided, shown in Figure 16. The sample is fixed inside RDS setup and the thermocouple is connected to temperature reader. The temperature of hot block was to 90°C and the temperature of cold block is set to 28°C. The gap between zone is 5 mm. The thermal gradient measurements were performed for three velocities: 0.1, 0.5 and 1 μm/s. The start position of the motor was read from the software and the values of the temperature was recorded by datalogger. Typical temperature versus position curve is shown in Figure 17.

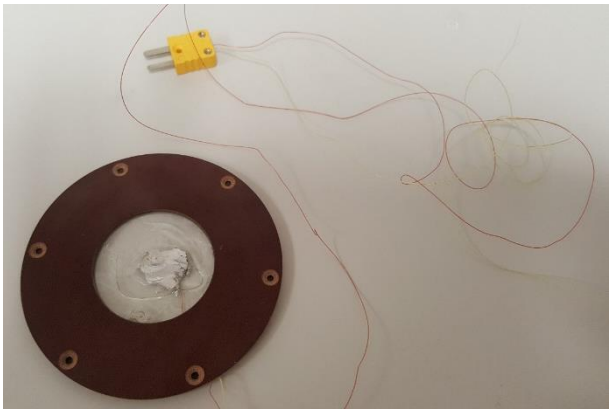

Figure 16. The sample used for thermal gradient measurements in RDS setup.

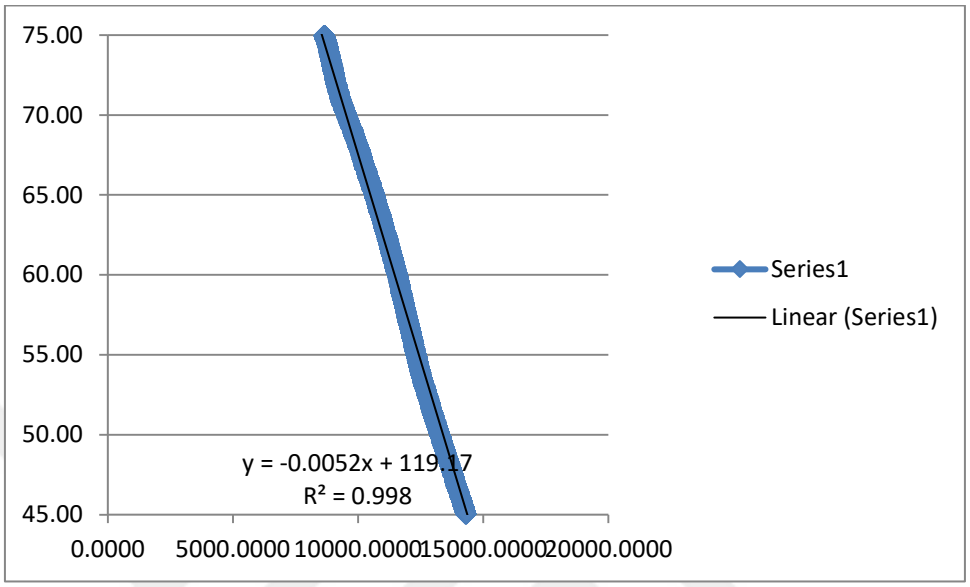

Figure 17. Thermal field at 5 mm Gap.

Linear fitting is performed in the range of 45-75°C. The average of thermal gradient is reported as the main G.

Appendix IX

Bulk samples experiment in high temperature directional setup

The alloy used in the bulk sample experiments was a ready In-Bi-Sn alloy. The alloy information is shown in Figure 18. The alloy was melted in a normal resistance furnace in KUTEM. Then, it was cast into the mold shown in Figure 19. The samples detached from runner system after solidifying. The sample are in rod shape with 5 mm diameter and 200 mm height. The sample was put inside the alumina crucible and inserted in high temperature directional setup, shown schematically in Figure 20 and Figure 21.

Figure 18. The ready alloy used for bulk sample experiments.

Figure 19. Mold and cast samples.

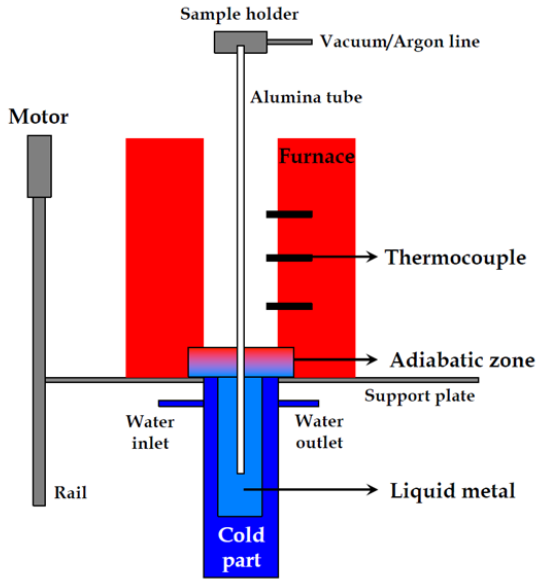

Figure 20. Schematic representation of high temperature directional solidification setup.

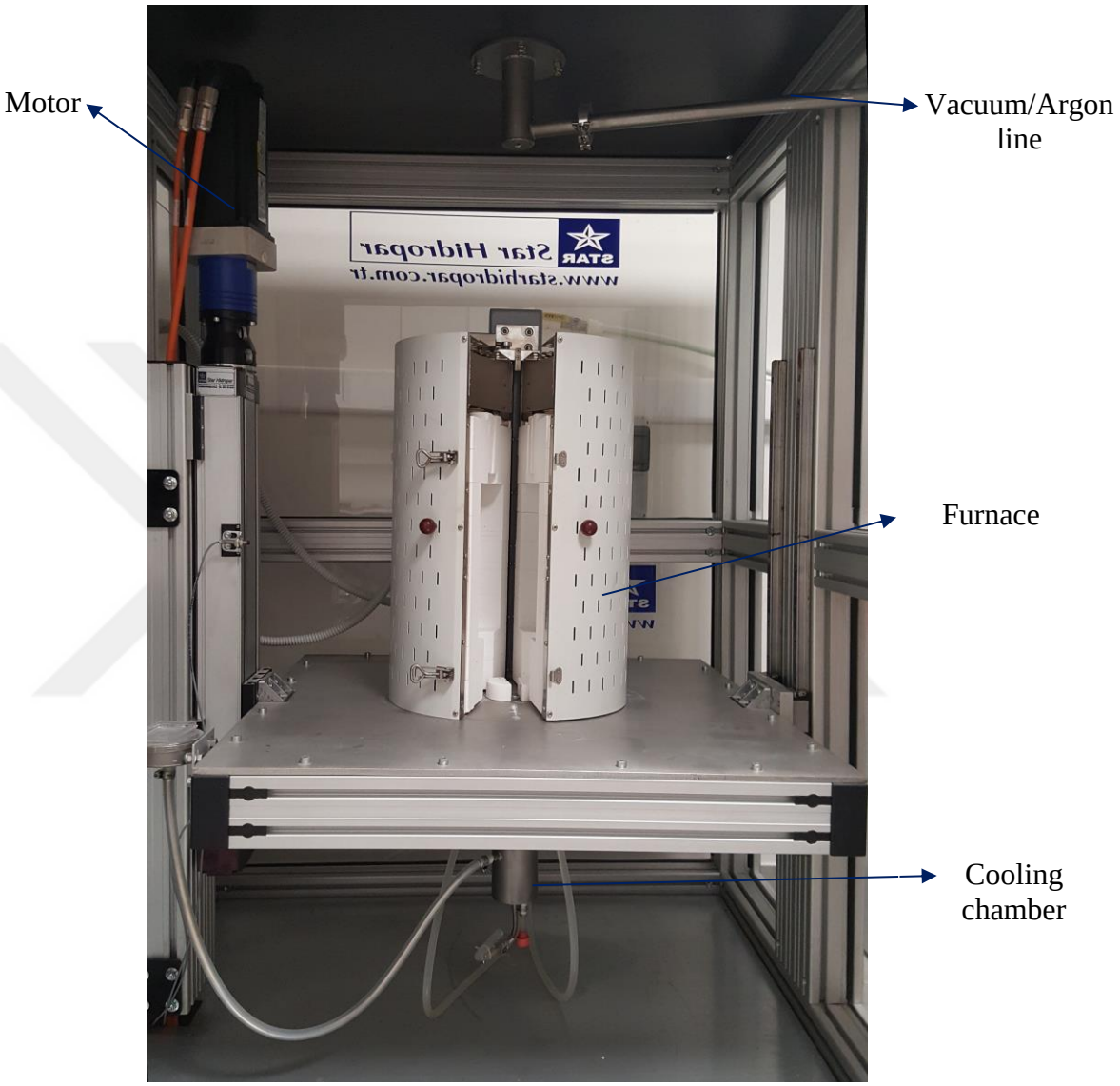

Figure 21. High temperature directional solidification setup.

Hot zone temperature was set 350°C and cold zone temperature was 20°C. Three growth velocities were examined: 1.3, 0.6, and 0.1 μm/s.

To have minimum temperature fluctuation of the furnace, the furnace control PID parameter were P = 1, I = 3 and D = 24, and power is 17.

Figure 22 shows the microstructures obtained in and 5 and 8 mm growth lengths at velocity 0.1 μm/s. In all examined samples, BC interface does not exist, irrespective of the microstructure. In some grains, the lamellar structure of ABAC pattern was observed.

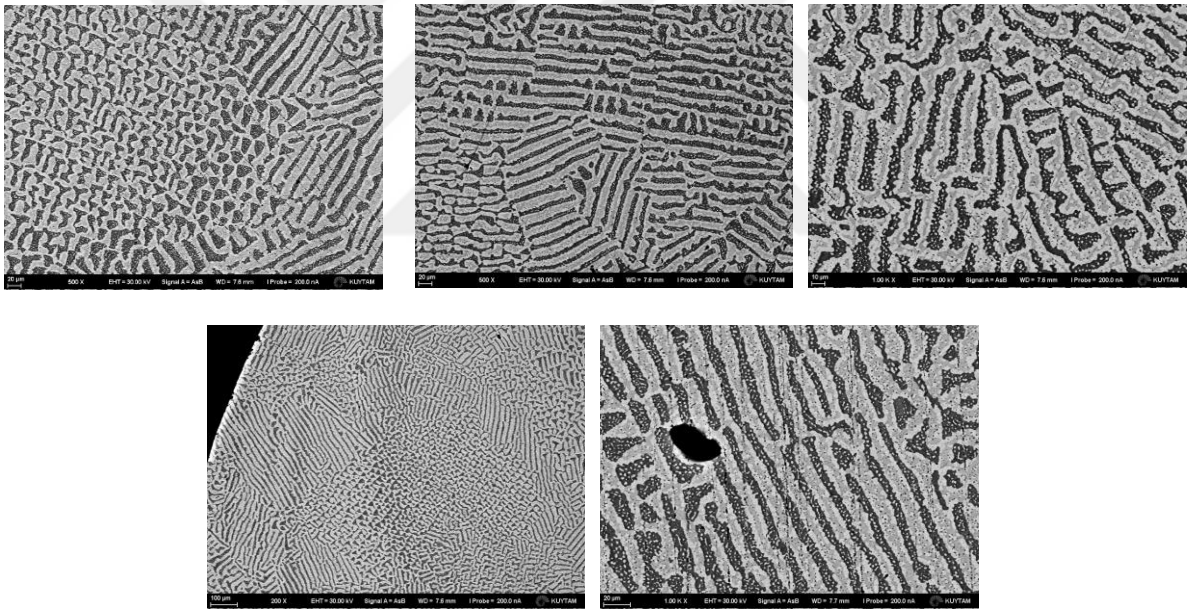

Figure 22. The microstructures observed in Bulk samples.